Quantitative Multi-Parameter Mapping in Magnetic Resonance Imaging

Dissertation

for the award of the degree
“Doctor rerum naturalium” (Dr.rer.nat)
of the Georg-August-Universität Göttingen

within the doctoral program
”Physics of Biological and Complex Systems”
of the Georg-August University School of Science (GAUSS)

submitted by

Nick Scholand

from Neheim-Hüsten

Göttingen, 2023

Thesis Committee:

Prof. Dr. Martin Uecker
Institute of Biomedical Imaging
Graz University of Technology, Graz

Prof. Dr. Hans-Christian Hofsäss
II. Institute of Physics
Georg-August-University, Göttingen

Prof. Dr. Susann Boretius
Functional Imaging
German Primate Center, Göttingen

Prof. Dr. Stefan Luther
Biomedical Physics
Max Planck Institute for Dynamics and Self-Organization, Göttingen

Members of the Examination Board:

First Reviewer:
Prof. Dr. Martin Uecker

Second Reviewer:
Prof. Dr. Hans-Christian Hofsäss

Further Members of the Examination Board:

Prof. Dr. Susann Boretius

Prof. Dr. Stefan Luther

Prof. Dr. Andreas Tilgner
Geophysics Institute
Georg-August-University, Göttingen

Prof. Dr. D. Russell Luke
Institute for Numerical and Applied Mathematics
Georg-August-University, Göttingen

Date of the oral examination: 27th June 2023

Contents

Glossary

ASY . . . . . asymmetric operator splitting

BART . . . . . Berkeley Advanced Reconstruction Toolbox

bSSFP . . . . . balanced steady-state free precession

BWTP . . . . . bandwidth time product

CG . . . . . conjugate gradient method

CLI . . . . . command line interface

CSF . . . . . cerebrospinal fluid

CT . . . . . computed tomography

DFT . . . . . discrete Fourier transform

DOPRI . . . . . Dormand-Prince

DQ . . . . . difference quotient

FFT . . . . . fast (discrete) Fourier transform

FID . . . . . free induction decay

FISTA . . . . . fast iterative shrinkage/thresholding algorithm

FLASH . . . . . fast low-angle shot

FoV . . . . . field of view

GIRF . . . . . gradient system impulse response function

GRE . . . . . gradient recalled echo

GRE-DA . . . . gradient recalled echo double-angle

HS1 . . . . . hyperbolic secant

IR . . . . . inversion-recovery

IR-bSSFP . . . . inversion-recovery balanced steady-state free precession

IR-FLASH . . . inversion-recovery fast low angle shot

IRGNM . . . . . iteratively regularized Gauss-Newton method

MR-STAT . . . . magnetic resonance spin tomography in time-domain

MRF . . . . . magnetic resonance fingerprinting

MRI . . . . . magnetic resonance imaging

MT . . . . . magnetization transfer

NIST . . . . . National Institute of Standards and Technology

NLINV . . . . . regularized nonlinear inverse reconstruction

NMR . . . . . nuclear magnetic resonance

nuFFT . . . . . non-uniform fast Fourier transform

ODE . . . . . ordinary differential equation

PCA . . . . . principal component analysis

PET . . . . . positron emission tomography

PI . . . . . parallel imaging

PSD . . . . . phase-sensitive detection

PWE . . . . . point-wise error

QMRI . . . . . quantitative magnetic resonance imaging

RF . . . . . radio frequency

RING . . . . . radial spoke intersections for gradient delay estimation

RK . . . . . Runge-Kutta

ROI . . . . . region of interest

ROT . . . . . rotation matrix

RT-NLINV . . . real-time regularized nonlinear inverse reconstruction

SAB . . . . . sensitivity analysis of the Bloch equations

SAR . . . . . specific absorption rate

SNR . . . . . signal-to-noise ratio

SS-Pre . . . . . slice-selective preconditioning

SSFP . . . . . steady-state free precession

STM . . . . . state-transition matrix

SVD . . . . . singular value decomposition

SY . . . . . symmetric operator splitting

TE . . . . . echo time

TI . . . . . inversion delay time

TR . . . . . repetition time

1. Introduction

Magnetic resonance imaging (MRI) is a versatile imaging technology with a broad variety of biomedical and clinical applications. It provides an excellent soft tissue contrast without the need for ionizing radiation or radioactive materials as required in modalities like computed tomography (CT) and positron emission tomography (PET). In general, the image contrast in MRI depends on tissue properties and hardware characteristics as well as the measurement technique. Thus, conventional MRI provides only a qualitative image contrast where images are interpreted based on relative intensity differences. In contrast, in quantitative magnetic resonance imaging (QMRI) physical properties such as relaxation constants, flow velocities, temperatures, or diffusion coefficients are determined in physical units. From a clinical perspective, QMRI is relevant for classification, detection, and monitoring of abnormal tissue [1]. It can be used to detect subtle changes that are not observable using conventional MRI and has the potential to replace measurements which require the use of contrast agents, benefiting otherwise excluded patients. From a methodological perspective, measuring physical quantities adds robustness of the acquired data against variations in the scanner hardware, the operating personnel or the software. It improves the longitudinal and inter-site comparability of results and thereby increases the reproducibility of studies.

Most existing techniques in QMRI rely on special sequences designed for high sensitivity to specific physical quantities, while being robust against other influences. They utilize analytical signal representations that are used in an additional fitting step to extract quantitative maps from conventionally reconstructed images [2–4]. The focus on robust sequences makes conventional QMRI methods very accurate in measuring specific physical quantities such as the T_1 and T_2 relaxation constants. Yet, this comes with a severe downside: The requirement to first obtain a number of high quality intermediate images for pixel-wise fitting leads to long measurement protocols which are then not feasible in a clinical setting.

By exploiting the data in a more efficient way, e.g., by incorporating prior knowledge, it is possible to reduce the amount of data required for reconstruction, and, consequently, shorten the measuring time. This can be achieved with model-based reconstructions that

bypass the reconstruction of intermediate images completely by formulating the image estimation as an inverse problem and by incorporating the physical signal model directly into the image reconstruction [5–8]. Thus, the acquisition of redundant information is avoided, which reduces the measurement time substantially.

Model-based reconstruction methods rely on sequences with analytical signal models [9, 10], which are convenient to use with numerical optimization algorithms applied in image reconstructions. These signal models are often derived using assumptions that limit their accuracy by excluding certain physical effects of the magnetization during the acquisition. Furthermore, the requirement of analytical models restricts the application of model-based reconstructions to specific MRI measurements. Several efficient sequences that are simultaneously sensitive to multiple parameters have complicated, often non-analytical signal expressions which prevent their use in established model-based reconstruction schemes [11, 12]. The acquisition of multiple parameter maps then requires multiple scans, which —even with shorter measurements— still presents a challenge in a clinical setting.

The aim of this thesis is to develop a generic model-based reconstruction method for quantitative mapping of multiple parameters with arbitrary MRI sequences. Building on a previous proof-of-principle study [13], a complete framework for QMRI that uses model-based reconstruction with the Bloch equations is developed and validated. The Bloch equations describe the behavior of nuclear spins under the influence of external magnetic fields and can be used to describe most MRI experiments. To integrate this into a practical reconstruction framework, a generic technique for the solution of the Bloch equations is described that efficiently exploits repeated patterns of the MRI measurement by pre-computation of state-transition matrices. This is combined with a direct sensitivity analysis for the computation of the partial derivatives that are required for numerical optimization. These techniques were then integrated into a calibration-less model-based reconstruction framework, which establishes a versatile and generic tool for QMRI. The technique was validated using simulations, phantom scans, and in vivo experiments.

The thesis starts in Chapter 2 with a theoretical overview of various fundamental concepts for MRI. The theory behind radio frequency (RF) excitation, signal acquisition, spatial encoding and reconstruction is discussed. The general concept of QMRI is introduced and various methods for the estimation of physical quantities are explained. In the end of the theoretical overview, techniques for the simulation of temporal evolutions of the magnetization in MRI experiments are introduced, followed by an overview about methods for the estimation of partial derivatives.

In Chapter 3 information about the software and hardware used in this thesis is provided.

It starts by introducing the MRI system, physical reference objects, and computational resources. Furthermore, software components for the simulation and reconstruction developed during this project are discussed. The chapter ends with a brief description on how the work of this thesis can be reproduced, listing the resources which provide the source code and raw data. The main part of this thesis consists of Chapters 4 and 5.

Chapter 4 is based on a journal article and presents the basic principles behind the nonlinear inversion of the Bloch equations and the details about the algorithm for the Bloch model-based reconstruction. The theoretical section shows how a direct sensitivity analysis for ordinary differential equations (ODEs) can be applied to the Bloch equations to compute their partial derivatives with respect to the physical parameters. It also presents how the state-transition matrix (STM) technique can be exploited for computationally efficient simulations of the temporal behavior of the magnetization in MRI experiments. Then, the integration of both concepts into a calibration-less model-based reconstruction framework is described. The technique is validated by reproducing a special case, for which an analytical signal model is available. This is done in a simulation and a physical phantom study as well as on an in vivo dataset acquired with an inversion-recovery fast low angle shot (IR-FLASH) sequence. Also in Chapter 4, the flexibility of the generalized forward model is demonstrated by simultaneous estimation of T_1 and T_2 relaxation parameters from inversion-recovery balanced steady-state free precession (IR-bSSFP) datasets. The simulation accuracy, the effect of regularization and a remaining physical bias due to magnetization transfer (MT) effects are discussed.

In Chapter 5, additional analyses are described that were performed to better understand the remaining bias observed for the in vivo IR-bSSFP scans. The influence of initialization and parameters on the Bloch model-based reconstruction as well as additional error sources such as B_0 field inhomogeneities and gradient imperfections are studied. The technique is also compared to results determined by pixel-wise fitting of images that were obtained by observing the magnetization dynamics in real-time exploiting real-time regularized nonlinear inverse reconstruction (RT-NLINV) [14].

Finally, the work is summarized and discussed in Chapter 6. Applications and future research directions are outlined.

2. Theoretical Overview

This section provides an overview of nuclear magnetic resonance (NMR) and magnetic resonance imaging (MRI) principles including signal generation, signal types, spatial encoding, sequences and image reconstruction. It also introduces quantitative MRI methods, such as basic T_1, T_2, B_1, and B_0 estimation, advanced physical modelling, and partial derivative calculation of complex signals for quantitative MRI.

2.1. Fundamentals of MRI

MRI generates signals with local magnetic field changes interacting with time-varying radio frequency (RF) fields. In the beginning of this section, the focus lies on how a magnetic field can be exploited to generate a signal response. Afterwards, the excitation and spatial encoding of signals is discussed and jointly explained in the concept of sequences. In the end, techniques to generate images from the acquired data are introduced. Thus, all concepts from magnetic field and signal generation to acquisition and reconstruction are covered.

2.1.1. Classical Description of Magnetization

The fundamental basis of MRI is the signal generation with magnetic fields. Because conventional MRI is based on H^1 spins (with quantum spin number $I = 1/2$) and their interactions with a temporary changing magnetic field, the underlying physical effects are generally of quantum mechanical nature. The magnitude μ of the spins' magnetic moment depends on the Planck constant $\hbar$ and the gyromagnetic ratio γ: [15, p.60]

$$\mu = \gamma\hbar\sqrt{I(I+1)}\ . \tag{2.1}$$

Individual spins cannot be resolved, and therefore, many of them are collectively observed within one volume element called voxel. In MRI, such a voxel has a volume of typically $1\ \mathrm{mm}^3$. Describing the individual magnetic moments $\boldsymbol{\mu}$ within one voxel

jointly defines a classical description of the spins' interactions with the macroscopic magnetization $\boldsymbol{M}$ [15, p.64]:

$$\boldsymbol{M} = \frac{1}{V} \sum_{n=1}^{N_s} \boldsymbol{\mu}_n \,, \tag{2.2}$$

and the number of spins N_s as well as the moment $\boldsymbol{\mu}_n$ of the n-th spin in the volume V. For a vanishing external magnetic field $\boldsymbol{B}_0 = 0$, the polarization of the individual spins within the collective is randomly distributed. This lack of preference in orientation leads to an overall disappearing $\boldsymbol{M}$.
For $\boldsymbol{B}_0 > 0$, the magnetic field adds a orientation preference which is parallel or anti-parallel to the external field. It is described by the Zeeman effect leading to a split of the quantum mechanical up and down states and resulting in discrete states of the z-component of the magentic moments μ_z [15, p.60],

$$\mu_z = \gamma m_I \hbar \,, \tag{2.3}$$

defined by the magnetic quantum number $m_I = -I, -I+1, \ldots, I$. The H^1 particles for MRI split into two states: the ground state $N_\uparrow$ with $m_I = 1/2$ and the excited state $N_\downarrow$ with $m_I = -1/2$. In Figure 2.1, both are visualized and different population levels are indicated.

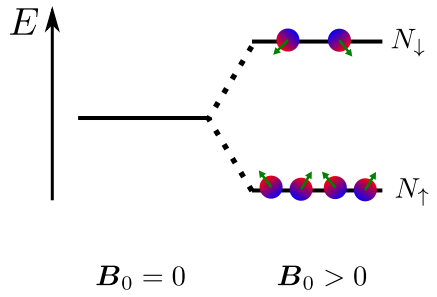

Figure 2.1: Visualization of a not-vanishing magnetization adding an orientation preference to a spin system of spin 1/2 particles. The Zeeman effect describes the splitting in the anti-parallel excited $N_\downarrow$ and the parallel ground state $N_\uparrow$. Figure taken from [13].

To understand the differently populated states, the energy of the ground and the excited state is required. Both follow with the magnetic quantum number [15, p.64]

$$E = -\boldsymbol{\mu} \cdot \boldsymbol{B}_0 = -\gamma \hbar m_I B_0 \,. \tag{2.4}$$

The energy difference between both states is defined by

$$\Delta E = E_{\downarrow} - E_{\uparrow} = \gamma \hbar B_0, \tag{2.5}$$

with the energy of the ground state $E_{\uparrow}$ and of the excited state $E_{\downarrow}$, respectively.

In the equilibrium state without any external RF pulses, the H^1 spins are Boltzmann-distributed over $N_{\downarrow}$ and $N_{\uparrow}$ [15, p.65]:

$$\frac{N_{\uparrow}}{N_{\downarrow}} = \exp\left(-\frac{\Delta E}{k_B T}\right), \tag{2.6}$$

with temperature T and the Boltzmann constant k_B. Because more spins are located in the ground state, this distribution is asymmetric leading to an overall non-zero macroscopic magnetization $M > 0$ with $\boldsymbol{M}$ being parallel to $\boldsymbol{B}_0$.

2.1.2. Rotating Coordinate Systems

In the previous section, the basic concepts behind the classical macroscopic magnetization are introduced. Here, the focus is on two coordinate systems commonly used for various explanations in MRI. First, the focus is on the individual spins $\boldsymbol{\mu}$. They are tilted against the external magnetic field $\boldsymbol{B}_0$ as illustrated in Figure 2.1. The tilting angle follows [15, p.63]

$$\theta = \arccos\left(\frac{\mu_z}{\mu}\right). \tag{2.7}$$

A tilted $\boldsymbol{\mu}$ in an external magnetic field exhibits a precession around $\boldsymbol{B}_0$ where the angular frequency is given by the Larmor frequency [15, p.63]:

$$\omega_0 = \gamma B_0. \tag{2.8}$$

This rotation of $\boldsymbol{M}$ can be either described from a stationary perspective, the laboratory frame, or incorporated into the coordinate system from a rotating perspective, the rotating frame. While the first describes the perspective of an outside observer, it is challenging to visualize temporary effects of $\boldsymbol{M}$ when it is rotating with a frequency of 127.74 MHz. In the rotating frame $\boldsymbol{M}$ is stationary which simplifies a visual understanding and explanation of evolutions of the magnetization. Both perspectives are discussed in detail in the following.

Laboratory Perspective In the laboratory frame, the observer is located in a stationary Cartesian coordinate system described by the coordinates x', y' and z. A tilted magnetization $\boldsymbol{M}$, as presented in Figure 2.2, is seen to rotate around $\hat{\boldsymbol{e}}_z$ with the frequency ω_0. In the laboratory frame, the magnetization is defined as

$$\boldsymbol{M}'(t) = M_{x'}(t)\hat{\boldsymbol{e}}_{x'} + M_{y'}(t)\hat{\boldsymbol{e}}_{y'} + M_z(t)\hat{\boldsymbol{e}}_z \,, \tag{2.9}$$

with the time independent basis vectors $\hat{\boldsymbol{e}}_{x',y',z}$.

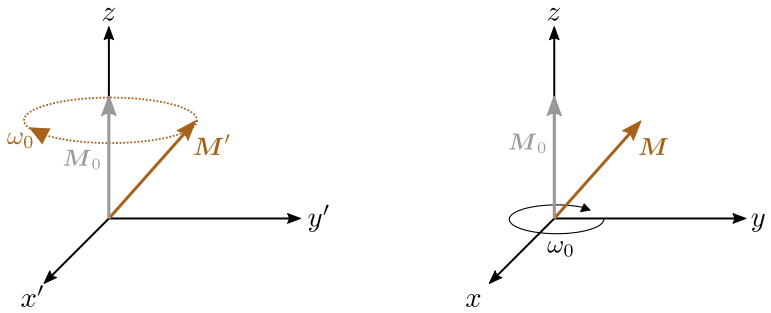

Figure 2.2: Visualization of the laboratory (left) and rotating (right) coordinate systems. On the left, the magnetization $\boldsymbol{M}'$ rotates with the frequency ω_0 around the z-axis. On the right, the magnetization $\boldsymbol{M}$ is static, while the coordinate system rotates with ω_0 around z. Figure modified from [13].

Rotating Perspective In the rotating frame, the observer is no longer stationary but its x-, y-, and z-coordinate system rotates with the Larmor frequency ω_0. A tilted magnetization as shown in Figure 2.2 appears to be stationary from this perspective. In general, the magnetization is described by

$$\boldsymbol{M}(t) = M_x(t)\hat{\boldsymbol{e}}_x(t) + M_y(t)\hat{\boldsymbol{e}}_y(t) + M_z\hat{\boldsymbol{e}}_z \,, \tag{2.10}$$

with the time-varying basis vectors $\hat{\boldsymbol{e}}_{x,y}(t)$. As these basis vectors rotate with constant ω_0, the notation of Equation (2.10) is typically simplified to

$$\boldsymbol{M}(t) = M_x(t)\hat{\boldsymbol{e}}_x + M_y(t)\hat{\boldsymbol{e}}_y + M_z\hat{\boldsymbol{e}}_z \,. \tag{2.11}$$

Both coordinate systems share the same z-axis. The transformation connecting the two coordinate systems is given by

$$\mathcal{R} : \boldsymbol{M}' \mapsto \boldsymbol{M} \,, \tag{2.12}$$

with [16, p.23]

$$\boldsymbol{M} = \mathcal{R}(t)\boldsymbol{M'} = \begin{pmatrix} \cos(\omega_0 t) & -\sin(\omega_0 t) & 0 \\ \sin(\omega_0 t) & \cos(\omega_0 t) & 0 \\ 0 & 0 & 1 \end{pmatrix} \boldsymbol{M'} \,. \tag{2.13}$$

For the temporal change, this becomes [17]

$$\frac{\mathrm{d}\boldsymbol{M}}{\mathrm{d}t} = \frac{\mathrm{d}\boldsymbol{M'}}{\mathrm{d}t} - \Omega \times \boldsymbol{M} \,, \tag{2.14}$$

with

$$\Omega = -\omega_0 \hat{\boldsymbol{e}}_z \,. \tag{2.15}$$

2.1.3. Excitation

With the introduced rotating perspective on the macroscopic magnetization $\boldsymbol{M}$, all tools are derived for introducing the classical concept of RF excitation through nuclear induction proposed by [18]. It is based on the application of a time-varying external magnetic field $\boldsymbol{B}_1(t)$ oriented within the transversal plane. While $\boldsymbol{B}_1(t)$ is static from the rotating perspective, it precesses around $\hat{\boldsymbol{e}}_z$ with an angular frequency ω_{RF} from the laboratory view [16, p.26]:

$$\boldsymbol{B}_1'(t) = B_1(t)\cos(\omega_{\mathrm{RF}} t)\ \hat{\boldsymbol{e}}_{x'} - B_1(t)\sin(\omega_{\mathrm{RF}} t)\ \hat{\boldsymbol{e}}_{y'} \,. \tag{2.16}$$

Adding $\boldsymbol{B}_1'(t)$ to the main magnetic field $\boldsymbol{B}_0$ gives a total magnetization at time t of

$$\boldsymbol{B'}(t) = \boldsymbol{B}_0 + \boldsymbol{B}_1'(t) \,. \tag{2.17}$$

The magnetization $\boldsymbol{M}$ precesses around $\boldsymbol{B'}(t)$ and its temporal evolution therefore follows [16, p.26]

$$\begin{aligned} \frac{\mathrm{d}\boldsymbol{M'}}{\mathrm{d}t} &= \gamma \boldsymbol{M} \times \boldsymbol{B'}(t) \\ &= \gamma \boldsymbol{M} \times \left[B_1(t)\cos(\omega_{\mathrm{RF}} t)\ \hat{\boldsymbol{e}}_{x'} - B_1(t)\sin(\omega_{\mathrm{RF}} t)\ \hat{\boldsymbol{e}}_{y'} + B_0 \hat{\boldsymbol{e}}_z \right] \,. \end{aligned} \tag{2.18}$$

For a better understanding, the temporal dynamics of the magnetization are mapped to the rotating frame from the laboratory perspective in Equation (2.18). First, the field $\boldsymbol{B}_1'(t)$ in Equation (2.16) is transformed to $\boldsymbol{B}_1(t)$ with $\mathcal{R}$ following Equation (2.13).

The result is inserted in Equation (2.18). In the last step, Equation (2.15) is used to transform the temporal change of the magnetization $\frac{\mathrm{d}\boldsymbol{M'}}{\mathrm{d}t}$. Finally, the precession from a

rotating perspective reads [16, p.27]

$$\frac{\mathrm{d}\boldsymbol{M}}{\mathrm{d}t} = \gamma \boldsymbol{M} \times \underbrace{\left(B_1(t)\cos([\omega_{\mathrm{RF}} - \omega_0]t)\ \hat{\boldsymbol{e}}_x - B_1(t)\sin([\omega_{\mathrm{RF}} - \omega_0]t)\ \hat{\boldsymbol{e}}_y + \hat{\boldsymbol{e}}_z \left(B_0 - \frac{\omega_0}{\gamma} \right) \right)}_{B_{\mathrm{eff}}(t)}, \tag{2.19}$$

which defines the effective field $B_{\mathrm{eff}}(t)$.
With a definition of the effective field in the rotating view, the resonance condition MRI is named after can be understood geometrically. Classically, precession is a rotation of the magnetization around $\boldsymbol{B}_0$. This effect is static in the rotating frame. When a $\boldsymbol{B}_1$ field is added in the transversal plane that fulfills the resonance condition

$$\omega_{\mathrm{RF}} = \omega_0\ , \tag{2.20}$$

it as well appears stationary in the rotating frame. This effect is illustrated in Figure 2.3.

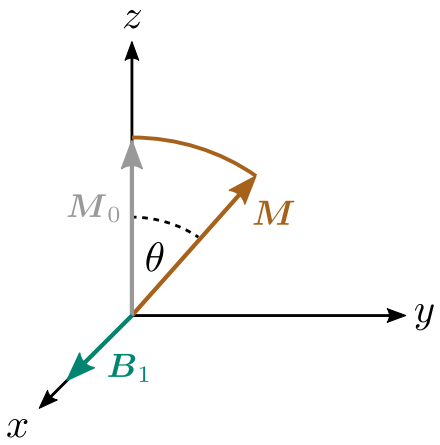

Figure 2.3: Visualization of the effect of an external magnetic field $\boldsymbol{B}_1$ acting on a magnetization $\boldsymbol{M}_0$ in the rotating frame of reference. $\boldsymbol{M}_0$ precesses around $\boldsymbol{B}_1$ until it reaches a position $\boldsymbol{M}$ flipped by the angle θ. Figure modified from [13].

Because B_{eff} is a superposition of $\boldsymbol{B}_0$ and $\boldsymbol{B}_1$, its orientation is no longer parallel to $\hat{\boldsymbol{e}}_z$. The precession axis changes leading to a rotation of the magnetization $\boldsymbol{M}$ around $\boldsymbol{B}_1$. This effect describes the on-resonant excitation with RF pulses from a classical perspective.

For an on-resonant $\boldsymbol{B}_1(t)$ Equation (2.19) simplifies to

$$\frac{\mathrm{d}\boldsymbol{M}}{\mathrm{d}t} = \gamma \boldsymbol{M} \times \left[\underbrace{B_1(t)\ \hat{\boldsymbol{e}}_x}_{\text{RF field}} + \underbrace{\hat{\boldsymbol{e}}_z \left(B_0 - \frac{\omega_{\mathrm{RF}}}{\gamma} \right)}_{\text{freq. offset}} \right] . \tag{2.21}$$

The tipping angle of this rotation, generally referred to as flip angle, follows with [16, p.69]

$$\theta(t) = \gamma \int_{t'=0}^{t} B_1(t')\mathrm{d}t' . \tag{2.22}$$

After the introduction of time-varying magnetic fields and the resonance condition, the following is focused on the actual design of two RF pulses. Both are chosen for their later application in the experiments of this work.

Sinc Pulses

The main frequency of the RF pulse is the carrier frequency ω_{RF}. When it fulfills the resonance condition in Equation (2.20) $\boldsymbol{B}_1$ is stationary in the rotating frame (compare Figure 2.3). Nevertheless, the amplitude $\boldsymbol{B}_1$ is changed by adding an envelope of the carrier frequency which defines the RF pulse's shape in MRI experiments. The first discussed design is a sinc pulse which follows

$$B_1(t) = A\ \mathrm{sinc}\left(\frac{\pi t}{t_0} \right) , \tag{2.23}$$

with the width of the main lope t_0 and the maximum amplitude A. The frequency representation of the sinc in Equation (2.23) is a rectangular function $\Pi(\omega)$. It is ideal for applications in slice-selection as further discussed in Section 2.1.7. In practice, a sinc cannot be used in MRI because it requires an infinite long application time. Thus, it needs to be cut at specific points in time giving a truncated sinc pulse

$$B_1(t) = \begin{cases} A\ \mathrm{sinc}\left(\frac{\pi t}{t_0}\right), & -N_L t_0 \leq t \leq N_R t_0 \\ 0, & \text{elsewhere} \end{cases} , \tag{2.24}$$

with $N_{L,R}$ as the number of zero-crossing to the left (L) and right (R). The pulse shape defined by Equation (2.24) is illustrated in Figure 2.4. The truncation of the infinite long sinc results in discontinuities of the derivative at both cutting points. For an intuitive understanding, the temporal limitation can be understood as the multiplication of the

infinite sinc with a rectangular function in time. Following the convolution property of the Fourier transform [15, p.31]

$$FT(\mathrm{sinc}(t) \cdot \Pi(t)) = FT(\mathrm{sinc}(t)) * FT(\Pi(t)) \tag{2.25}$$

$$= \Pi(\omega) * \mathrm{sinc}(\omega)\,, \tag{2.26}$$

this relates to a convolution of the frequency response of the ideal sinc with the Fourier transform of a rectangular function. Following $FT(\Pi(t)) = \mathrm{sinc}(\omega)$, oscillations around the sharp edges of the original rectangular frequency response occur as shown in Figure 2.4.

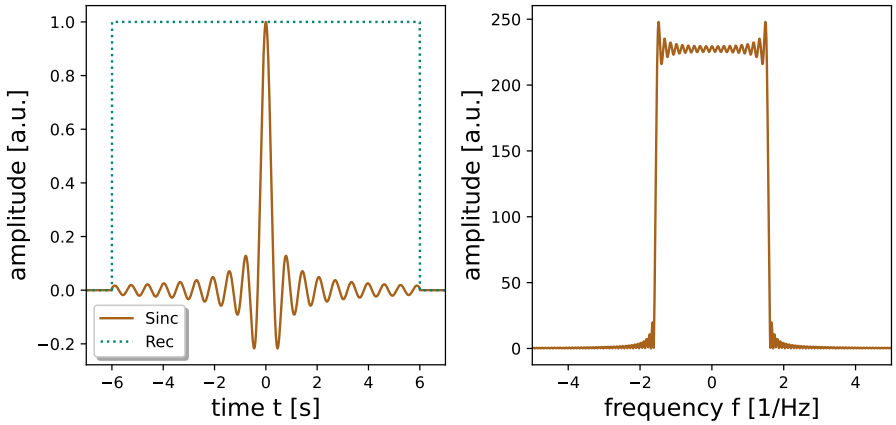

Figure 2.4: Visualization of a truncated sinc function defined by Equation (2.24) (left) and its frequency representation (right). The shape is defined by N_L=N_R=6, A=1 and t_0=1. The rectangular function representing the truncation limits is added in time domain. Figure modified from [13].

To reduce oscillations, the cut sinc pulse in Equation (2.24) can be apodized by applying a windowing function like a Hamming ($\alpha = 0.46$) or a Hanning window ($\alpha = 0.5$). No windowing function corresponds to $\alpha = 0$. The analytical representation of the windowed and temporal limited sinc pulse is [16, p.39]

$$B_1(t) = \begin{cases} A\left[(1-\alpha) + \alpha\cos\left(\frac{\pi t}{N t_0}\right)\right]\ \mathrm{sinc}\left(\frac{\pi t}{t_0}\right), & -N_L t_0 \leq t \leq N_R t_0 \\ 0, & \text{elsewhere.} \end{cases} \tag{2.27}$$

An analytical representation of its integral in time is derived in Section A1. The windowing decreases the amplitude of the pulse to zero at the cutting points. This can be understood as a multiplication of the $\boldsymbol{B}_1$ field not with a rectangular function $\Pi(t)$, but with a constant function C following

$$FT(C) = C \cdot \delta(t) \ . \tag{2.28}$$

With the Dirac delta function $\delta(t)$ the convolution does not interpolate neighboring frequencies and oscillations are avoided. The different windowing functions and their effect on the frequency representation of the RF pulse are visualized in Figure 2.5.

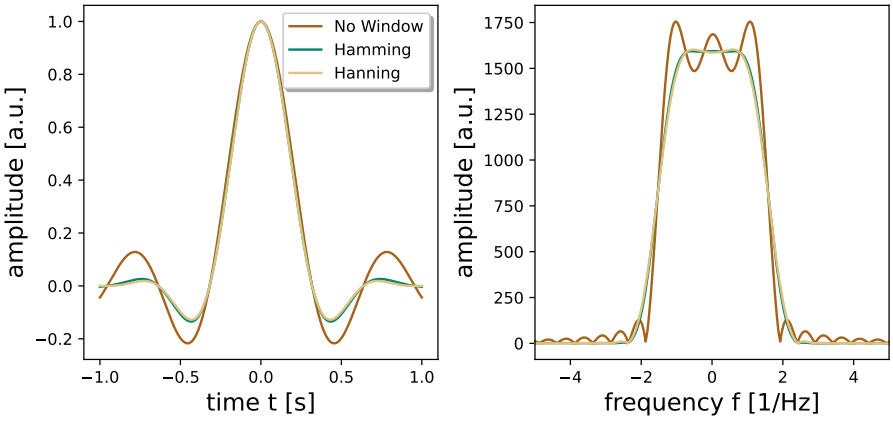

Figure 2.5: Visualization of a truncated sinc function on the left defined by Equation (2.27). The effect of multiple windowing functions defined by α are presented: no-windowing, a Hanning- and a Hamming-window. Their frequency responses are shown on the right. The shape of the sinc pulses is defined by: N_L=N_R=1, A=1 and t_0=1. Figure modified from [13].

Adiabatic Inversion Pulses

In MRI, sinc pulses are commonly chosen for their simplicity and their almost rectangular frequency response. They are designed with temporal variations solely in the amplitude, as shown in Figure 2.5. In contrast adiabatic RF pulses are designed for robustness against $\boldsymbol{B}_0$ inhomogeneities and accurate inversion of the magnetization. This second class of RF pulses vary in amplitude and frequency and consequently has a greater complexity.
In the following, the concept of adiabatic pulses is introduced. Their effects on the magnetization are discussed and the origins behind their robustness are explained. While the class of adiabatic pulses is large, this work is focused on hyperbolic secant (HS1) inversion pulses initially published by Silver *et al.* [19] as they are used in the inversion-recovery sequences of this work.
The temporal evolution of the amplitude $\omega_1(t)$ of a HS1 pulse follows

$$\omega_1(t) = \omega_1^{\max} \left(\operatorname{sech}(\beta t)\right)^{1+i\gamma} \ , \tag{2.29}$$

depending on the maximum amplitude $\omega_1^{\max}$, the modulation of the angular frequency β, and an additional dimensionless factor μ. Equation (2.29) can be expressed in a coordinate system rotating with a constant angular frequency ω_c [20],

$$\omega_1(t) = \omega_1^{\max}\mathrm{sech}(\beta t)e^{i\phi(t)} , \tag{2.30}$$

leading to a time-varying phase [20]

$$\phi(t) = \mu \ln(\mathrm{sech}(\beta t)) . \tag{2.31}$$

For a better understanding, the explanation follows [20] with Equations (2.30) and (2.31) being transformed to a frequency-modulated rotating coordinate system. Its angular frequency $\omega_{\mathrm{RF}}(t)$ follows the frequency of the RF pulse $\omega_{\mathrm{RF}}(t)$. Compared to the rotating frame introduced in Section 2.1.2, its time-dependency varies. Within this system, the amplitude of the HS1 pulse is described by

$$\omega_1(t) = \omega_1^{\max}\mathrm{sech}(\beta t) , \tag{2.32}$$

while the frequency is given by the derivative of Equation (2.31) with respect to t and reads

$$\frac{\mathrm{d}\phi}{\mathrm{d}t} = \omega_{\mathrm{RF}}(t) - \omega_c = -\mu\beta\tanh(\beta t) . \tag{2.33}$$

In the frequency-modulated frame, the effect of the HS1 pulse can be described geometrically because it appears stationary. The effective RF field ω_{eff} consists of the two components $\boldsymbol{\omega}_1(t)$ and $\boldsymbol{\Delta\omega}(t)$:

$$\boldsymbol{\omega}_1(t) = \omega_1(t)\hat{\boldsymbol{e}}_{x_{\mathrm{RF}}} \tag{2.34}$$

$$\boldsymbol{\Delta\omega}(t) = (\omega_0 - \omega_{\mathrm{RF}}(t))\hat{\boldsymbol{e}}_z , \tag{2.35}$$

with the Larmor frequency ω_0. Since $\omega_1(t)$ and $\omega_{\mathrm{RF}}(t)$ vary with time, $\omega_{\mathrm{eff}}(t)$ rotates with the angular velocity of

$$\frac{\mathrm{d}\alpha}{\mathrm{d}t} = \mathrm{d}\left(\arctan\left[\frac{\omega_1(t)}{\Delta\omega(t)}\right]\right)/\mathrm{d}t . \tag{2.36}$$

The temporal dynamics during the HS1 inversion pulse are illustrated in Figure 2.6.

For $\omega_{\mathrm{RF}} \ll \omega_0$, the effective field $\omega_{\mathrm{eff}} \approx \Delta\omega$ is parallel to $\hat{\boldsymbol{e}}_z$. During the frequency sweep ($\omega_{\mathrm{RF}} \rightarrow -\omega_{\mathrm{RF}}$) , the effective field ω_{eff} moves towards the transversal plane where the on-resonance condition is fulfilled: $\omega_{\mathrm{RF}} \approx \omega_0$ and $\omega_{\mathrm{eff}} = \omega_1$. Afterwards, the ω_{eff} continues

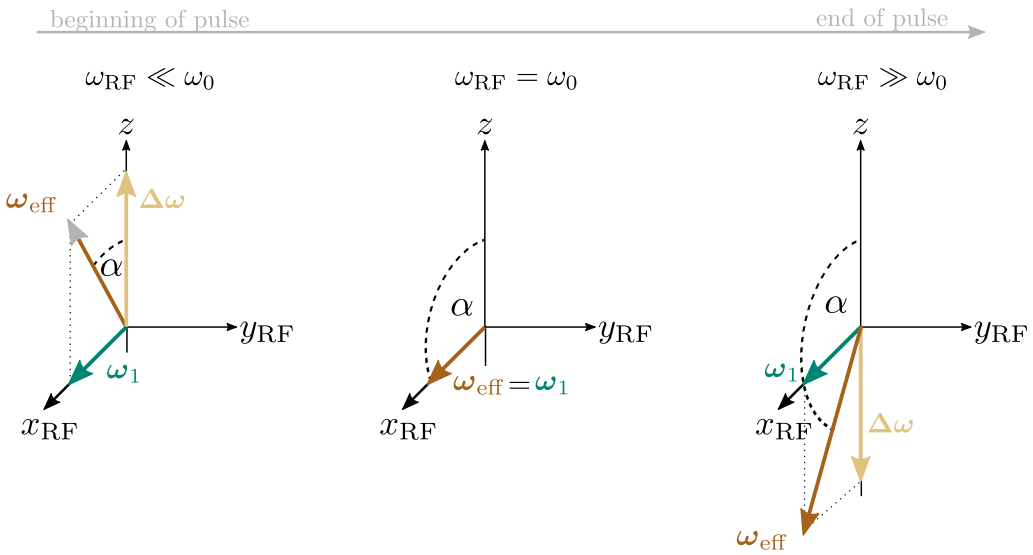

Figure 2.6: Visualization of the effective magnetic field ω_{eff} which is experienced by isochromates during an adiabatic HS1 inversion pulse in a frequency modulated coordinate system. The left presents its projections on the z- and x_{RF}-axis for ω_{RF} far away from the Larmor frequency ω_0. The center shows both for the on-resonant case leading to a vanishing z-axis projection $\boldsymbol{\Delta\omega}$ and a tipping angle α of 90°. On the right, both components are presented for $\omega_{RF} \gg \omega_0$ leading to an inverted $\boldsymbol{\Delta\omega}$. Figure inspired by [20].

the rotation until $\omega_{RF} \gg \omega_0$ and until the effective field will be oriented anti-parallel to $\hat{\boldsymbol{e}}_z$. The isochromates can follow ω_{eff} during this passage when the adiabatic condition

$$|\omega_{eff}(t)| \gg \left|\frac{d\alpha}{dt}\right| \tag{2.37}$$

is fulfilled. This holds for HS1 inversion pulses if [16, p.195]

$$\omega_1^{max} \gg \frac{\sqrt{\mu}\beta}{\gamma}\,. \tag{2.38}$$

The fundamental robustness of adiabatic pulses against B_0 inhomogeneities results from their designed sweep through a broad range of frequencies. Inhomogeneities lead to isochromates with different resonance frequencies, which are not possible to excite with a simple sinc pulse designed for a single carrier frequency ω_{RF}. During the application of an adiabatic pulse, spins within a broad range of frequencies experience the whole sweep, but at different time points. This ensures a high inversion efficiency even in the presence of inhomogeneities of the main magnetic field.

2.1.4. Signal Acquisition

The previously introduced excitation rotates the macroscopic magnetization $\boldsymbol{M}$ around an applied time-varying RF field. In this section, the example of a $\pi/2$-pulse is used to explain the concept of signal acquisition in MRI. The $\pi/2$-pulse flips $\boldsymbol{M}$ into the transversal plane: $\boldsymbol{M} = \boldsymbol{M}_{xy}$. From the laboratory perspective, the transversal component $\boldsymbol{M}_{xy}$ precesses around the z-axis with the Larmor frequency ω_0. This induces a voltage $V(t)$ in neighboring loops [15, p.95],

$$V(t) = -\frac{\partial \Phi(t)}{\partial t} = -\frac{\partial}{\partial t} \int\limits_{\text{object}} \boldsymbol{B}(\boldsymbol{r}) \boldsymbol{M}(\boldsymbol{r},t) \mathrm{d}\boldsymbol{r} \,, \tag{2.39}$$

following Faraday's law of induction. These receivers need to resonate at the Larmor frequency to be able to detect the signal from the precessing magnetization. The resulting signal has a high frequency due to the typically high magnetic field strengths in MRI.
To improve its post-processing, the signal is demodulated by ω_0. The technique is called phase-sensitive detection (PSD). $V(t)$ is multiplied with a reference sinusoidal signal $2\cos(\omega_0 t)$ and the double frequency component is removed by low-pass filtering [15, p.97]. The resulting low frequency signal $S_1(t)$ corresponds to a rotating perspective. With a single demodulation, the direction of the rotation of the transversal magnetization cannot be detected. Therefore, a second demodulation is performed with a reference signal that is phase-shifted by $\pi/2$: $2\sin(\omega_0 t)$ [15, p.99]. It results in a second signal $S_2(t)$ orthogonal to $S_1(t)$. This quadrature detection is often expressed in a complex notation:

$$S(t) = S_1(t) + iS_2(t) \,. \tag{2.40}$$

The signal $S(t)$ is proportional to the transversal component of the magnetization:

$$S(t) \propto M_{xy}(t) = M_x(t) + iM_y(t) \,, \tag{2.41}$$

with $M_{x,y}(t) = |\boldsymbol{M}(t)\hat{\boldsymbol{e}}_{x,y}|$. The proportionality constant includes the effect of different distances between the object and the receiver coils. In later sections this effect of varying coil sensitivities is discussed. For simplicity, this work describes the signal with M_{xy} and ignores further effects influencing $S(t)$.
A detailed discussion about the principles of signal detection was carried out by [15, p.94ff].

2.1.5. Relaxation

Up to now, no interactions between individual spins have been taken into account. They can lead to a reduced inversion efficiency when isochromates are moved through the transversal plane. Therefore, different types of interactions between spins and their surroundings based on [18, 21, 22] are introduced and modelled in this section. A more detailed description was given by [22].

T_1 Relaxation The T_1 relaxation results from a model that incorporates interactions between the spins and their surrounding lattice. Energy between spins and lattice is exchanged which connects both thermally. Heat is understood as Brownian motion which represents the temperature of the spin system. The focus here is on fast molecular motion which allows for the approximation of dipol-dipol interactions by random field fluctuations. A generalized model describing slow molecular motions was developed by [23].

The model from Section 2.1.1 is continued where spins in the excited state $N_\downarrow$ have the energy $E_\downarrow$ and the ones in the ground state $N_\uparrow$ have $E_\uparrow$. The difference of spins between both levels $n = N_\uparrow - N_\downarrow$ has been shown to contribute to the macroscopic magnetization. Let $n(t = 0) = n_0$ describe the difference in equilibrium. An applied RF pulse changes n by lifting spins from $E_\uparrow$ up to $E_\downarrow$ through absorption. After the RF pulse is switched off, the system relaxes back to its equilibrium state. This transitions in the spin system originate from stimulated emissions induced by their interactions with random field changes that are created from the surrounding lattice. The process can be described classically with the ordinary differential equation (ODE) [18, 22],

$$\frac{\mathrm{d}n}{\mathrm{d}t} = \frac{n_0 - n}{T_1}\,, \tag{2.42}$$

and the relaxation constant T_1. Taking into account that n corresponds to M_z of a voxel and n_0 replacing M_0 in the equilibrium state, the solution of the ODE (2.42) is

$$M_z = M_0 \left(1 - e^{-\frac{t}{T_1}}\right)\,. \tag{2.43}$$

This T_1 relaxation can be understood as an increase of the M_z component until the equilibrium state M_0 is reached. The effect is visualized in Figure 2.7.

T_2 Relaxation The T_2 relaxation describes interactions between individual spins. The overall energy of the spin system does not change and only the polarization of the

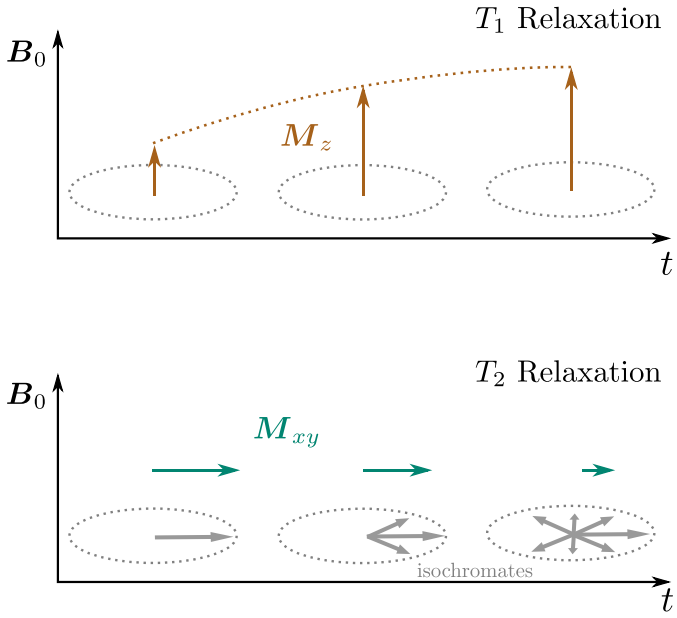

Figure 2.7: Visualization of the effect of relaxation on the longitudinal (top) and transversal magnetization (bottom). While the T_1 relaxation describes the increase of M_z over time, T_2 models the decreasing M_{xy} component due to dephasing of the isochromates that are summed up to the macroscopic magnetization. Figure modified from [13].

macroscopic magnetization of a voxel is affected. Spin 1/2-particles like H^1 have no quadrupole moment which makes dipol-dipol interactions the dominating effect for the T_2 relaxation in conventional MRI. By approximating dipol-dipol interactions with random field fluctuations [22], the classical interpretation of T_2 is a dephasing effect of the spins which is visualized in Figure 2.7. Here, the transversal magnetization $M_{xy} = \boldsymbol{M} \cdot \hat{\boldsymbol{e}}_{\boldsymbol{x}} + i\boldsymbol{M} \cdot \hat{\boldsymbol{e}}_{\boldsymbol{y}}$ is the sum over all dephased spins and T_2 reduces M_{xy} by changing the phase of the individual spins and by keeping the overall polarization of $\boldsymbol{M}$ constant. The dynamic of M_{xy} can be described with the ODE [18],

$$\frac{\mathrm{d}M_{xy}}{\mathrm{d}t} = -\frac{1}{T_2} M_{xy} \,, \tag{2.44}$$

and its solution is

$$M_{xy} = M_0 e^{-\frac{t}{T_2}} \,. \tag{2.45}$$

The T_2 relaxation results from a model that incorporates interactions within the spin assemble for the ideal chase of a homogeneous magnetic field. Only the dipol-dipol

interactions result in random field fluctuations and dephasing. Field fluctuations due to B_0 inhomogeneities increase the dephasing of the spins and increases the transversal relaxation rate which is described by the effective relaxation time $T_2^* < T_2$.

2.1.6. Combined Temporal Evolution Models

In the previous sections, the excitation and relaxation effects in MRI have been classically described. After introducing them individually, they will be combined to a single system of ODEs in this section. The derived equations describe the temporal evolution of the classical magnetization within the limits of the random field fluctuation model. They include the Bloch equations and extensions to diffusion and multiple substance compartments.

Bloch Equations The Bloch equations introduced by Bloch in 1946 [18] describe the temporal dynamics of a two-level spin system in the presence of both time-varying RF fields and different types of interactions between the spins and their surroundings. It does not describe individual spins but focuses on the classical macroscopic magnetization that results from Zeemann splitting. Spin interactions are described with two relaxation constants. The Bloch equations read

$$\frac{\mathrm{d}\boldsymbol{M}}{\mathrm{d}t} = \gamma \boldsymbol{M} \times \boldsymbol{B} - \frac{\hat{\boldsymbol{e}}_x \boldsymbol{M} + \hat{\boldsymbol{e}}_y \boldsymbol{M}}{T_2} - \frac{\hat{\boldsymbol{e}}_z \boldsymbol{M} - M_0}{T_1}\,, \tag{2.46}$$

with

$$\boldsymbol{M} = \begin{pmatrix} M_x \\ M_y \\ M_z \end{pmatrix} \quad \text{and} \quad \boldsymbol{B} = \begin{pmatrix} B_x \\ B_y \\ B_z \end{pmatrix}. \tag{2.47}$$

It takes major assumptions, like a spatially stationary macroscopic magnetization and a single type of observed particles. Incorporating further extension of the Bloch equations, which avoid these assumptions, are not part of this work. Nevertheless, the possible extensions are briefly discussed for a better understanding of possible future work.

Bloch-Torrey Equations The originally proposed model by Bloch in Equation (2.46) takes the assumptions of stationary spins, which does not hold in general. An extension incorporating this effect was proposed by Torrey in 1956 [24] who included an additive diffusion term with the diffusion coefficients $\boldsymbol{D}$ and small drift terms in all directions $\boldsymbol{M}_0$:

$$\frac{\partial \boldsymbol{M}}{\partial t} = \gamma \boldsymbol{M} \times \boldsymbol{B} - \frac{\hat{\boldsymbol{e}}_x \boldsymbol{M} + \hat{\boldsymbol{e}}_y \boldsymbol{M}}{T_2} - \frac{\hat{\boldsymbol{e}}_z \boldsymbol{M} - M_0}{T_1} - \nabla \cdot \boldsymbol{D} \nabla (\boldsymbol{M} - \boldsymbol{M}_0). \tag{2.48}$$

This model requires spins to have only small drift velocities, but can be further extended to incorporate flow terms [25].

Bloch-McConnell Equations The Bloch equations in Equation (2.46) assume a single type of observed particles. In reality, multiple interacting substances frequently contribute to the measured signal. This is modelled by the Bloch-McConnell extension [26] which added a second semi-solid pool $\boldsymbol{M}_s$ and exchange rates to the free water pool $\boldsymbol{M}_w$ with first order transversal life times $\tau_{2,s\to w}$ and $\tau_{2,w\to s}$ as well as the longitudinal life time $\tau_{1,s\to w}$ and $\tau_{1,w\to s}$:

$$\begin{aligned}\frac{\mathrm{d}\boldsymbol{M}_w}{\mathrm{d}t} &= \gamma \boldsymbol{M}_w \times \boldsymbol{B} - \frac{\hat{\boldsymbol{e}}_x \boldsymbol{M}_w + \hat{\boldsymbol{e}}_y \boldsymbol{M}_w}{T_{2,w}} - \frac{\hat{\boldsymbol{e}}_z \boldsymbol{M}_w - M_{0,w}}{T_{1,w}} \\ &\quad - \frac{\hat{\boldsymbol{e}}_x \boldsymbol{M}_w + \hat{\boldsymbol{e}}_y \boldsymbol{M}_w}{\tau_{2,w\to s}} - \frac{\hat{\boldsymbol{e}}_z \boldsymbol{M}_w}{\tau_{1,w\to s}} + \frac{\hat{\boldsymbol{e}}_x \boldsymbol{M}_s + \hat{\boldsymbol{e}}_y \boldsymbol{M}_s}{\tau_{2,s\to w}} + \frac{\hat{\boldsymbol{e}}_z \boldsymbol{M}_s}{\tau_{1,s\to w}} \\ \frac{\mathrm{d}\boldsymbol{M}_s}{\mathrm{d}t} &= \gamma \boldsymbol{M}_s \times \boldsymbol{B} - \frac{\hat{\boldsymbol{e}}_x \boldsymbol{M}_s + \hat{\boldsymbol{e}}_y \boldsymbol{M}_s}{T_{2,s}} - \frac{\hat{\boldsymbol{e}}_z \boldsymbol{M}_s - M_{0,s}}{T_{1,s}} \\ &\quad + \frac{\hat{\boldsymbol{e}}_x \boldsymbol{M}_w + \hat{\boldsymbol{e}}_y \boldsymbol{M}_w}{\tau_{2,w\to s}} + \frac{\hat{\boldsymbol{e}}_z \boldsymbol{M}_w}{\tau_{1,w\to s}} - \frac{\hat{\boldsymbol{e}}_x \boldsymbol{M}_s + \hat{\boldsymbol{e}}_y \boldsymbol{M}_s}{\tau_{2,s\to w}} - \frac{\hat{\boldsymbol{e}}_z \boldsymbol{M}_s}{\tau_{1,s\to w}}.\end{aligned} \tag{2.49}$$

By assuming the same exchange rate in transversal ($1/\tau_{1,s\to w} = 1/\tau_{2,s\to w} = k_{s\to w}$) and longitudinal ($1/\tau_{1,w\to s} = 1/\tau_{2,w\to s} = k_{w\to s}$) direction, this reduces to [27]

$$\begin{aligned}\frac{\mathrm{d}\boldsymbol{M}_w}{\mathrm{d}t} &= \gamma \boldsymbol{M}_w \times \boldsymbol{B} - \frac{\hat{\boldsymbol{e}}_x \boldsymbol{M}_w + \hat{\boldsymbol{e}}_y \boldsymbol{M}_w}{T_{2,w}} - \frac{\hat{\boldsymbol{e}}_z \boldsymbol{M}_w - M_{0,w}}{T_{1,w}} \\ &\quad - k_{w\to s} \boldsymbol{M}_w + k_{s\to w} \boldsymbol{M}_s \\ \frac{\mathrm{d}\boldsymbol{M}_s}{\mathrm{d}t} &= \gamma \boldsymbol{M}_s \times \boldsymbol{B} - \frac{\hat{\boldsymbol{e}}_x \boldsymbol{M}_s + \hat{\boldsymbol{e}}_y \boldsymbol{M}_s}{T_{2,s}} - \frac{\hat{\boldsymbol{e}}_z \boldsymbol{M}_s - M_{0,s}}{T_{1,s}} \\ &\quad + k_{w\to s} \boldsymbol{M}_w - k_{s\to w} \boldsymbol{M}_s,\end{aligned} \tag{2.50}$$

with the overall exchange rates $k_{s\to w}$ and $k_{w\to s}$.

2.1.7. Spatial Encoding

Previous sections described the temporal evolution of a single magnetization $\boldsymbol{M}$, but full objects consist of many voxels at different locations $\boldsymbol{r}$. While the Bloch equations take the assumption of a single component in a voxel contributing to its signal, the overall received signal is still a superposition of all voxels.

In this section, spatial encoding is introduced and combined in the concept of sampling trajectories. It explains how the signal from different locations $\boldsymbol{r}$ is separated by relying on the basic principle of gradients and frequency controlled RF pulses. For simplicity, the following explanations assume linear gradient systems. Further developments extend spatial encoding to nonlinear gradients with curved planes [28, 29] and multi-slice excitations [30–32]. In the end of this section, a brief introduction to parallel imaging (PI) is added.

Slice-Selection

The first spatial dimension in MRI is encoded using a slice-selection gradient. Without loss of generality, the gradient is assumed to be located in z-direction: $\boldsymbol{G}_z = G_z\hat{\boldsymbol{e}}_z$.
The gradient induces a magnetic field $\boldsymbol{B}_z(\boldsymbol{r})$ which depends on the location $\boldsymbol{r}$,

$$\boldsymbol{B}_z(\boldsymbol{r}) = \boldsymbol{G}_z\, \boldsymbol{r}\, \hat{\boldsymbol{e}}_z\,, \tag{2.51}$$

and modifies the total magnetic field:

$$\boldsymbol{B}(\boldsymbol{r}) = \boldsymbol{B_0} + \boldsymbol{B}_z(\boldsymbol{r}) = (B_0 + \boldsymbol{G}_z\boldsymbol{r})\hat{\boldsymbol{e}}_z\,. \tag{2.52}$$

It assumes a strong main magnetic field $\boldsymbol{B}_0$ that leads to the vanishing of concomitant fields [16, p.292f].
Introducing a spatially dependent $\boldsymbol{B}(\boldsymbol{r})$ changes the resonance frequency [15, p.145]:

$$\omega_{\boldsymbol{r}} = \omega_0 + \gamma\boldsymbol{G}_z\boldsymbol{r}\,. \tag{2.53}$$

This encodes the spatial position $\boldsymbol{r}$ along z with a frequency ω_{z_c} which can be matched with the carrier frequency ω_{RF} of the RF pulse:

$$\omega_{\mathrm{RF}} \stackrel{!}{=} \omega_{z_c} = \gamma(B_0 + G_z z_c)\,. \tag{2.54}$$

The frequency response of the applied RF pulse defines the shape of the excited slice centered at z_c. Figure 2.8 illustrates this effect for a pulse with perfect rectangular frequency response, as provided by an infinite sinc pulse.

After the excitation of a single slice of an object, the received signal is still a superposition of all voxels within this slice. To explain the theory behind the encoding of the signal in the two other spatial dimensions the next section introduces the frequency and phase encoding concepts.

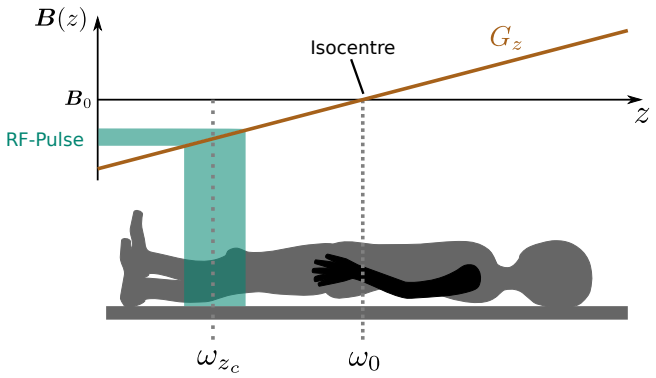

Figure 2.8: Visualization of the physical effects during slice-selection. A slice-selection gradient G_z introduces a spatially dependent resonance frequency. By adjusting the carrier frequency of an exciting RF pulse to match ω_{z_c}, its frequency response is exploited to excite a single slice centered around z_c. Figure modified from [13].

Frequency Encoding

Frequency encoding allows for encoding a two-dimensional slice along individual isolines, as illustrated in Figure 2.9.

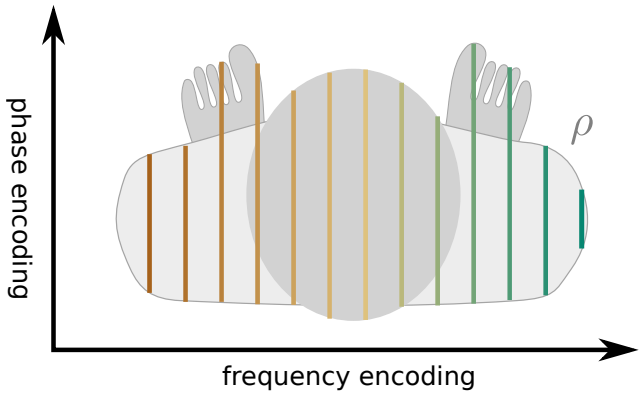

Figure 2.9: Visualization of different isolines within an object ρ spatially encoded with a frequency encoding gradient. Figure modified from [13].

From the physical perspective, the signal from individual isolines is separated with a frequency encoding gradient $\boldsymbol{G}_{\text{fe}}$. Its application results in a spatially dependent local magnetic field and a precession frequency [15, p.153]

$$\omega(\boldsymbol{r}) = \omega_0 + \gamma \boldsymbol{G}_{\text{fe}} \boldsymbol{r} \,. \tag{2.55}$$

The signal $S(t)$ at time t received from the excited slice $\rho(\boldsymbol{r})$ of the object ρ becomes [15, p.153]

$$S(t) = \int_{\text{object}} \mathrm{d}S(\boldsymbol{r},t) = \int_{-\infty}^{\infty} \rho(\boldsymbol{r}) \mathrm{e}^{-i\gamma(B_0+G_{\text{fe}}\boldsymbol{r})t} \mathrm{d}\boldsymbol{r}\,, \tag{2.56}$$

and can be demodulated by the Larmor frequency in Equation (2.8):

$$\tilde{S}(t) = \int_{\text{object}} \rho(\boldsymbol{r}) \mathrm{e}^{-i\gamma G_{\text{fe}}\boldsymbol{r}t} \mathrm{d}\boldsymbol{r}\,. \tag{2.57}$$

The frequency encoding is visualized in Figure 2.10 showing the different frequencies for the isolines in Figure 2.9.

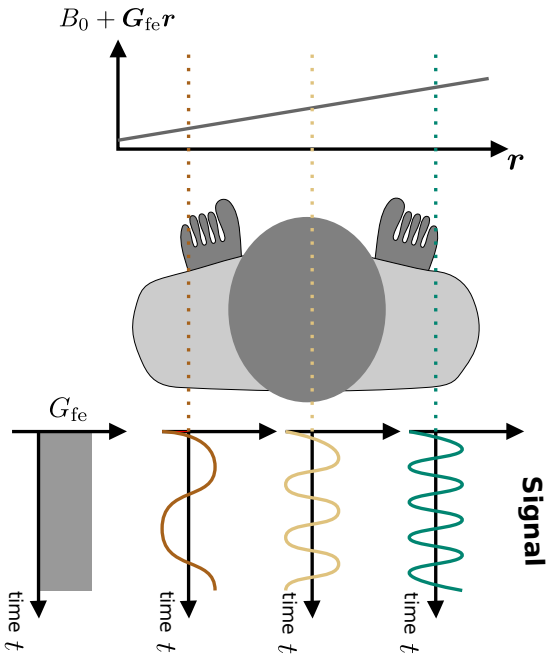

Figure 2.10: Visualization of the physical concepts behind frequency encoding. A gradient $\boldsymbol{G}_{\text{fe}}$ modifies the magnetic field B_0 locally and leads to a spatially dependent frequency of the signal. Figure modified from [13].

From the signal perspective, MRI data is measured in frequency space, also called k-space. High frequencies are located at the borders and low frequencies in the center. Taking a two-dimensional acquisition as an example, a frequency is encoded with the coordinates k_x and k_y (compare Figure 2.11). The frequency encoding gradient $\boldsymbol{G}_{\text{fe}}$ maps the time t to the frequencies $\boldsymbol{k}$ [15, p.158]:

$$\boldsymbol{k} = \begin{cases} \frac{\gamma}{2\pi}\, \boldsymbol{G}_{\mathrm{fe}} t & \text{FID signals} \\ \frac{\gamma}{2\pi}\, \boldsymbol{G}_{\mathrm{fe}} (t - \mathrm{TE}) & \text{echo signals .} \end{cases} \tag{2.58}$$

Here, $\boldsymbol{G}_{\mathrm{fe}}$ maps the time t to two different trajectories. The free induction decay (FID) appears directly after the RF excitation, while the echo signal describes the trajectory at the time point shifted by echo time (TE) following a refocusing event. By inserting Equation (2.58) in Equation (2.57), the description for the measured signal is expressed as a function of $\boldsymbol{k}$ [15, p.158],

$$S(\boldsymbol{k}) = \int_{\mathrm{object}} \rho(\boldsymbol{r}) \mathrm{e}^{-2\pi i \boldsymbol{k}\boldsymbol{r}} \mathrm{d}\boldsymbol{r} \,, \tag{2.59}$$

showing the Fourier relation between the excited object ρ and the acquired k-space data $S(\boldsymbol{k})$. The temporal order in which the signal $S(\boldsymbol{k})$ is sampled is referred to as sampling trajectory. To understand the effect of the frequency encoding on this trajectory, a two-dimensional echo signal is considered [15, p.158]:

$$k_x = \frac{\gamma}{2\pi}\, G_x (t - \mathrm{TE}) \tag{2.60}$$

$$k_y = \frac{\gamma}{2\pi}\, G_y (t - \mathrm{TE}) \,. \tag{2.61}$$

These coordinates can be transformed from Cartesian to polar coordinates with the magnitude

$$k = \frac{\gamma}{2\pi}\, (t - \mathrm{TE}) \sqrt{G_x^2 + G_y^2} \,, \tag{2.62}$$

and the rotation angle

$$\phi = \tan^{-1} \left(\frac{G_y}{G_x} \right) \,, \tag{2.63}$$

defined by the ratio between the gradient amplitudes G_x and G_y. The transformation leads to

$$k_x = k \cos \phi \tag{2.64}$$

$$k_y = k \sin \phi \,. \tag{2.65}$$

Therefore, the effect of the frequency encoding on the sampling trajectory can be understood with a radial line in k-space. It is rotated by an angle ϕ, as shown in Figure 2.11.

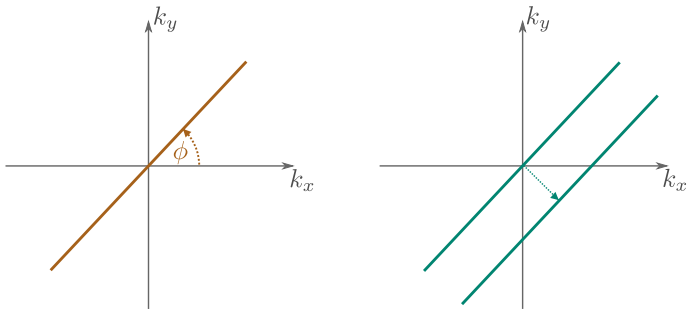

Figure 2.11: Visualization of the signal perspective on spatial encoding. Frequency encoding has a time dependent effect and samples radial lines tilted by an angle ϕ (left). Phase encoding shows a sampling time independent effect offsetting the sampled trajectory relative to the center of k-space (right). Figure modified from [13].

Phase Encoding

Following the introduction to the concept behind frequency encoding, phase encoding is explained in this section. It aims to encode the received signal along the isolines illustrated in Figure 2.9.

The phase encoding is based on an additional gradient $\boldsymbol{G_p}$ switched on for a defined time T_p. It adds a spatially dependent linear phase $\phi(\boldsymbol{r})$ [15, p.156]

$$\phi(\boldsymbol{r}) = -\gamma \boldsymbol{G_p} \boldsymbol{r} T_p \,, \tag{2.66}$$

to the received signal from the volume element $\mathrm{d}S(\boldsymbol{r},t)$ [15, p.156]:

$$\mathrm{d}S(\boldsymbol{r},t) = \begin{cases} \rho(\boldsymbol{r})\ \mathrm{e}^{-i\gamma(B_0+\boldsymbol{G_p}\boldsymbol{r})t}, & 0 \le t \le T_p \\ \rho(\boldsymbol{r})\ \mathrm{e}^{-i\gamma \boldsymbol{G_p}\boldsymbol{r}T_p}\ \mathrm{e}^{-i\gamma B_0 t}, & T_p \le t\,. \end{cases} \tag{2.67}$$

The additional phase is illustrated in Figure 2.12. Integrating the signal over the whole object and demodulating it by the Larmor frequency leads to [15, p.156]

$$\tilde{S}(t) = \int_{\text{object}} \rho(\boldsymbol{r}) \mathrm{e}^{-i\gamma \boldsymbol{G_p}\boldsymbol{r}T_p} \mathrm{d}\boldsymbol{r} \,, \tag{2.68}$$

similar to the frequency encoding in Section 2.1.7.

The phase encoding gradient $\boldsymbol{G_p}$ modifies the measured spatial frequencies for a fixed time T_p. This changes the trajectory following [15, p.163]

$$\boldsymbol{k} = \frac{\gamma}{2\pi} \int_0^{T_p} \boldsymbol{G_p}(\tau)\mathrm{d}\tau \tag{2.69}$$

$$\Rightarrow \boldsymbol{k} = \frac{\gamma}{2\pi} \boldsymbol{G_p} T_p, \quad \text{for} \quad \boldsymbol{G_p}(\tau) = \text{const}\,. \tag{2.70}$$

Inserting Equation (2.70) into (2.68) shows the same Fourier relation like Equation (2.59). Compared to the idea of frequency encoding, Equation (2.69) shows that the effect of phase encoding on the sampling trajectory is independent of the sampling time t. It only depends on the fixed time T_p during which the gradient is turned on and affects the sampling trajectory with a constant offset. This process is visualized in Figure 2.12.

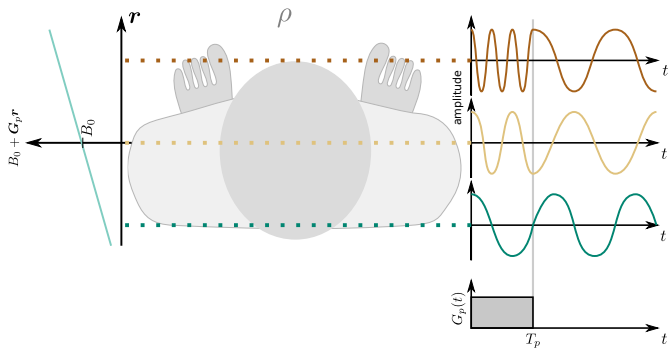

Figure 2.12: Visualization of the physical effect during phase encoding. A gradient $\boldsymbol{G}_p$ locally modifies the main magnetic field $\boldsymbol{B}_0$ for a fixed time T_p. This induces a spatially dependent phase change in the signal. Figure modified from [13].

Sampling Trajectories

With the combined effect of the phase and frequency encoding gradients, various sampling schemes of the k-space can be achieved. An exemplary overview on a fast low-angle shot (FLASH) sequence is given in Figure 2.13 showing how different gradients can be combined to create a sampling trajectory. Here, the slice-selection gradient has no influence on the spatial encoding. Instead, it focuses all spins moving the start of the encoding to the low frequencies in the k-space center. Afterwards, according to Equation (2.63), the simultaneous effects of the phase and frequency encoding gradients lead to a radially outward sampling in frequency space. The corresponding angle of the radial spoke is defined with the ratio of both gradient moments following Equation (2.63). During the echo acquisition, the frequency encoding gradient is active, moving through the k-space

in a horizontal line while measuring the signals. By modifying the ratio between the gradients, all other horizontal k-space lines can be acquired in further repetitions.

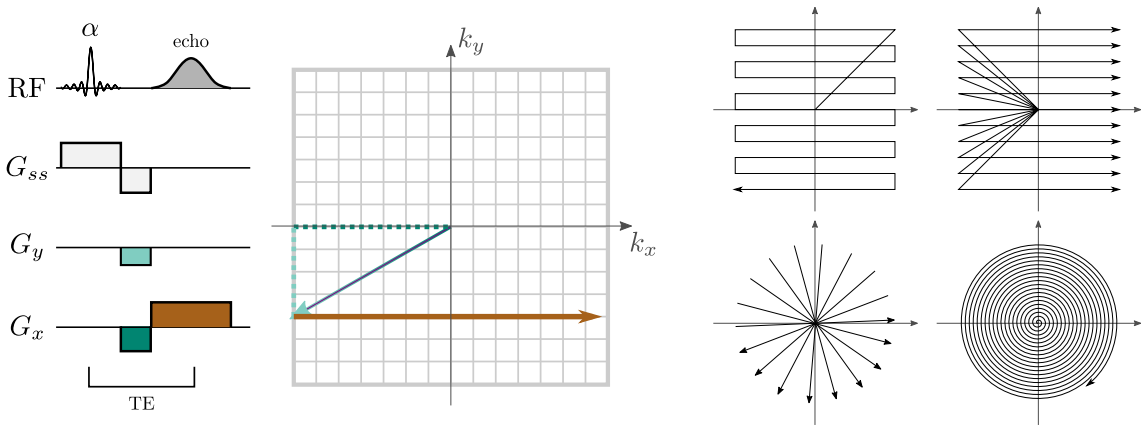

Figure 2.13: Visualization of a sequence diagram of a FLASH sequence (left) with its sampling trajectory (center) and other classes of sampling trajectories (right). Figure partially adapted from [13].

Depending on the order in which the frequencies are sampled, the different trajectories are prone to various inaccuracies, like motion (Cartesian) and gradient delays (radial, spiral). A more detailed discussion was elaborated by [33, 34].

Parallel Imaging

Up to now, only gradients have been exploited for spatial encoding, even though multiple receive coils can add additional spatial information. An illustration of this effect for an individual signal is shown in Figure 2.14. By placing an array of receivers around the measured object, the signal of a point source becomes stronger in receivers close to it and it becomes weaker in those further away. With the knowledge about the sensitivity of the individual channels, the strength of these individual signals in the various coils encode spatial information.
This simplistic example fails if more than a single signal source is acquired. The resulting superposition of the signals cannot be separated if only the coil sensitivities are known. While it does not replace frequency and phase encoding, this simple example demonstrates that spatial information is provided by the knowledge about the individual receiver sensitivities. The technique exploiting this additional knowledge is called PI and can be efficiently used to compensate missing data from not measured k-space frequencies. This reduces the length of sequences and speeds up MRI examinations. Reconstruction methods that exploit PI make use of the spatial correlations in multi-receive coil data

while still keeping the quality of images similar to those of full k-space acquisitions. Many of these techniques have been developed in the past [35]. Here, the focus is on regularized nonlinear inverse reconstruction (NLINV) [36] which is introduced in Section 2.1.9.

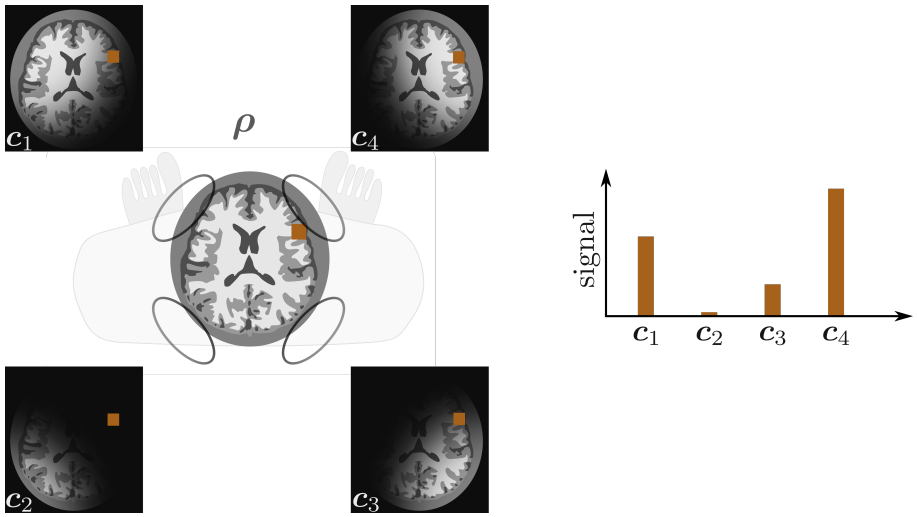

Figure 2.14: Visualization of parallel imaging (PI) for spatial encoding. The signal of the observed object ρ is detected by multiple receive channels $c_{1,2,3,4}$ with each acquiring other areas depending on their location. This leads to varying signals of the colored point source in ρ in the channels. With the knowledge about the receivers' spatial sensitivity, the location of the brown signal can roughly be found from the measured signal plot on the right alone. This simple example demonstrates the spatial information but does not work for multiple signal sources. Parallel imaging is no replacement for phase and frequency encoding, but can only add additional knowledge.

2.1.8. Pulse Sequences

In the previous section, the influence of different gradients on the acquisition in k-space and their relation to sampling trajectories have been discussed. In this section, the focus is on how gradients and RF excitation events are combined to actual measurements in MRI, called sequences. Besides tissue and hardware related properties, sequences have a major influence on the contrast of the resulting reconstructions. Many sequences have been designed to produce specific relative contrasts to encode a wide variety of physical effects. After using a simple FLASH sequence diagram in an example in Figure 2.13, three often used sequences of this work are introduced. While many of them provide a mixed contrast depending on multiple physical effects, some can encode individual parameters.

These sequences are used for quantitative parameter mapping in quantitative magnetic resonance imaging (QMRI) and are discussed in Section 2.2.

Spin-Echo

The first sequence discussed in this work is the spin-echo sequence. It is one of the first developed sequences in MRI and was introduced by Hahn in 1950 [37]. Its main event blocks are visualized in Figure 2.15.

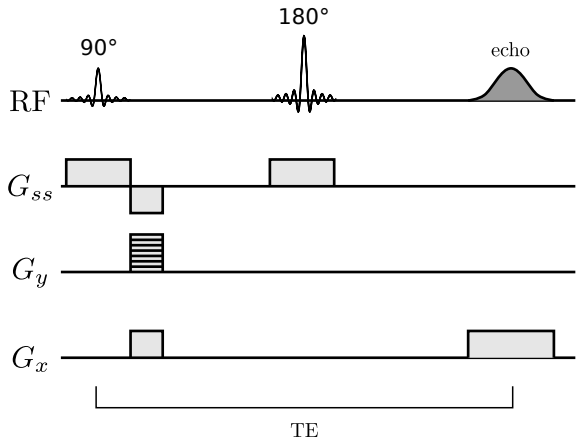

Figure 2.15: Visualization of a sequence diagram for a spin-echo sequence. the refocusing 180° pulse is centered between the 90° excitation pulse and the echo. The pulses are simultaneously turned on together with slice-selection gradients. An additional slice-rephaser and frequency as well as phase encoding gradients are shown.

It starts with a 90° pulse with a simultaneously active slice-selection gradient. Those are followed by a slice-rephaser with the negative half of the integral of the slice-selection gradient. It is simultaneously turned on with phase and frequency encoding gradients. During a slice-selective 180° pulse halfway through the TE, an additional slice selection gradient is added. Symmetrical around the 180° refocusing pulse, a readout gradient samples the generated echo signal.
The spin-echo sequence typically requires long repetition time (TR), because the excitation with the 90° pulse needs to be applied to the initial magnetization M_0 to avoid further influences on the contrast of the data. TR needs to be long enough so that the excited magnetization can relax back with T_1 to M_0.
The spin-echo sequence is often used for its robustness especially in gold-standard QMRI sequences, as further discussed in Section 2.2.

(IR) FLASH

The second sequence discussed in this work is the FLASH which belongs to the family of steady-state free precession (SSFP) sequences. It relies on a steady-state M_{ss} developed under application of repetitive RF pulses in combination with short TR. It results from an equilibrium state between external B_1 field effects and T_1 relaxation. The FLASH sequence is a spoiled SSFP [38]. After each TR, the transversal magnetization is entirely dephased. This can be achieved either by application of additional gradients and constant phase [39, 40] or by using random phase RF spoiling [41].
By exploiting much shorter TR compared to spin-echo sequences, FLASH allows significantly reduced acquisition times. Combined with an advanced reconstruction a single slice can be acquired in 20 ms [14].
Through its repetitive spoiling in each TR and short TE, FLASH sequences are robust against field inhomogeneities. The steady-state between B_1 and T_1 makes it sensitive to changes in the longitudinal relaxation and B_1 inhomogeneities. This sensitivity leads to a T_1 dependent contrast in the data, also referred to as T_1 weighted contrast.

To increase the capability of the sequence to encode T_1 for QMRI applications, FLASH can be extended by an initial inversion pulse followed by a transversal spoiling gradient and an inversion delay time (TI). This modification is illustrated in Figure 2.16. Without any RF excitation, the inverted magnetization relaxes back to M_0 which is described by the T_1 relaxation. During this transition phase, also called transient state, the inversion-recovery fast low angle shot (IR-FLASH) sequence includes a FLASH readout that influences the relaxation with repetitive RF excitations. This modified transient state is characterized by the effective relaxation T_1^* and the equilibrium steady-state M_{ss}. The analytical model derived from the Bloch equations that describes the IR-FLASH signal evolution is called the Look-Locker model [42]. It depends on the variables for the steady-state M_{ss}, M_0 and $R_1^* = 1/T_1^*$ that encode mixed physical effects of the relative flip angle α_{eff} and T_1. The model can be reformulated to depend on the underlying physical parameters following [43] as briefly presented in Section 4.7.3.

The IR-FLASH sequence is used in QMRI for T_1 mapping. When being combined with a model-based reconstruction framework these maps can be determined efficiently from small amounts of data [9]. The technique is introduced in Section 2.2.2.

(IR) bSSFP

The last basic MRI sequence discussed in this work is similar to FLASH. The balanced steady-state free precession (bSSFP) is also part of the family of SSFP sequences and

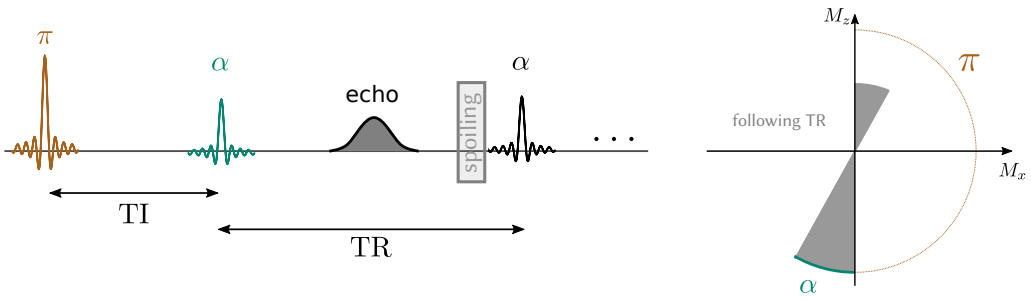

Figure 2.16: Visualization of an IR-FLASH sequence (left) and the evolution of the magnetization for RF pulses parallel to the y-axis (right). It shows the initial inversion pulse with TI as well as the FLASH readout that consists of excitation pulses with flip angle α, an echo and a spoiling event.

was introduced by [44]. It exploits a similar short TE and TR, but uses a higher flip angle leading to magnetization transfer (MT) influences [45–47] and finite RF pulse effects for longer pulse durations [48]. Instead of spoiling events, it provides a balanced gradient moment in each repetition and a 180° phase change between consecutive RF pulses to reach a steady-state [49]. This makes the sequence less robust against field inhomogeneities leading to the characteristic banding artifacts shown in Figure 5.4.

The signal of a bSSFP follows [50]

$$M_{ss} = M_0 \frac{\sin\alpha(1-E_1)}{1-(E_1-E_2)\cos\alpha - E_1E_2} \cdot e^{-\frac{\mathrm{TE}}{T_2^*}}, \tag{2.71}$$

with $E_{1,2} = \exp\left(-\frac{\mathrm{TR}}{T_{1,2}}\right)$ and therefore depends not only on the physical parameters T_1, M_0 and B_1, as FLASH does, but is also sensitive to T_2^*. By taking the assumption that off-resonances are smaller than π within a TR and setting,

$$\mathrm{TE} = \tfrac{1}{2} \cdot \mathrm{TR},$$

the transverse magnetization is refocused similar to a spin-echo sequence, and thus reduces the T_2^* dependency to T_2 [51]. This case is the default in this work. It ensures the contrast of the bSSFP to be proportional to $\sqrt{T_2/T_1}$ leading to high signal-to-noise ratio, especially for liquids like cerebrospinal fluid (CSF) and fat tissue [49].

Similar to the IR-FLASH, the bSSFP can also be extended with an initial inversion module. It increases the T_1 sensitivity of the sequence for QMRI applications. This addition makes the sequence even more sensitive to off-resonances requiring an accurate magnetization preparation either with an $\alpha/2$-TR/2 preparation [49], as shown in Figure 2.17, or with ramps of varying flip angles [52, 53]. The benefit of the increased sensitivity to more physical effects is that the inversion-recovery balanced steady-state free precession

(IR-bSSFP) allows for simultaneous mapping of T_1 and T_2 if the actual flip angle is known. It decouples both parameters from B_1, as further discussed in Section 4.7.5.

The IR-bSSFP is used in this work because of its increased sensitivity and simultaneous mapping possibilities for T_1 and T_2 parameters.

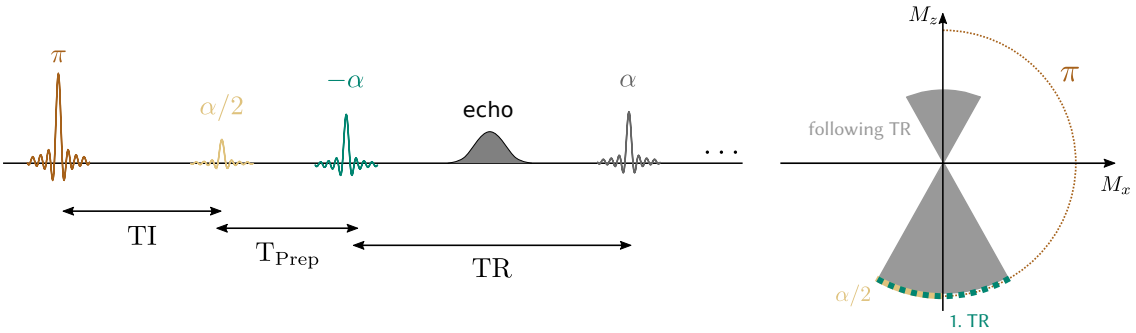

Figure 2.17: Visualization of an IR-bSSFP sequence (left) and the evolution of the magnetization for RF pulses parallel to the y-axis (right). It shows the initial inversion pulse with TI, the preparation pulse with preparation time T_{Prep} and the bSSFP readout. The latter consists of excitation pulses with flip angle α and an alternating phase as well as echoes in the center of the TR.

2.1.9. Image Reconstruction

In the previous sections, the basic concepts of excitation, spatial encoding and sequences have been introduced in order to provide an understanding of the data acquisition with different signal encodings and various sampling patterns. In this section, the focus lies on the image reconstruction of measured data. The aim is to introduce the theory behind the reconstruction of the slice of the object $\rho(\boldsymbol{r})$ at location $\boldsymbol{r}$ from the measured frequency signals $S(\boldsymbol{k})$.

Fourier Reconstruction

The definition in Equation (2.59) shows that the measured object and the signal are related via a Fourier transformation. The object can be reconstructed from the acquired k-space with an inverse Fourier transform:

$$\rho(\boldsymbol{r}) = \int_{-\infty}^{\infty} S(\boldsymbol{k}) \mathrm{e}^{2\pi i \boldsymbol{k}\boldsymbol{r}} \mathrm{d}\boldsymbol{k}. \tag{2.72}$$

This involves approximations like the acquisition of all data at a single point in time and a continuous as well as infinite sampling of the object. While the temporal assumption influences the use of MRI as measurement device in QMRI, it can be assumed to hold for conventional applications. The continuous and infinite sampling on the other hand influence all MRI reconstructions and is further discussed in the following for a simplified one-dimensional case.

Discretization Receiver hardware does not allow for continuous acquisition of signals. The occurring echo can only be sampled with a defined sampling size Δk. This gives a one-dimensional sampling basis of

$$D = \{n\Delta k,\ -\infty < n < \infty\}\,, \tag{2.73}$$

and the continuous reconstruction in Equation (2.72) becomes [15, p.191]

$$\rho(x) \approx \sum_{n=-\infty}^{\infty} S(n\Delta k)\mathrm{e}^{2\pi i n\Delta k x}\,. \tag{2.74}$$

With the Poisson formula [15, p.191]

$$\sum_{n=-\infty}^{\infty} \mathrm{e}^{2\pi i n\Delta k x} = \frac{1}{\Delta k}\sum_{n=-\infty}^{\infty} \delta\left(x - \frac{n}{\Delta k}\right)\,, \tag{2.75}$$

Equation (2.74) simplifies to an inverse discrete Fourier representation:

$$\rho(x) \approx \frac{1}{\Delta k}\sum_{n=-\infty}^{\infty} \rho\left(x - \frac{n}{\Delta k}\right)\,. \tag{2.76}$$

The infinite but discrete sampling results in periodic replicas of the object at frequencies that are shifted by a factor of $\frac{1}{\Delta k}$ are illustrated in Figure 2.18.

If the sampling Δk is not chosen small enough, the replicas overlap with the original ρ creating infolding artifacts in the reconstruction.
To find an accurate sampling, the fact of support limited objects can be exploited [15, p.193]. Every measured object ρ will not extend a limit L so that

$$\rho(x) = 0,\ |x| > \frac{L}{2}\,. \tag{2.77}$$

The limit L will be referred to as field of view (FoV). The sampling size can then be chosen following the Nyquist sampling criterion

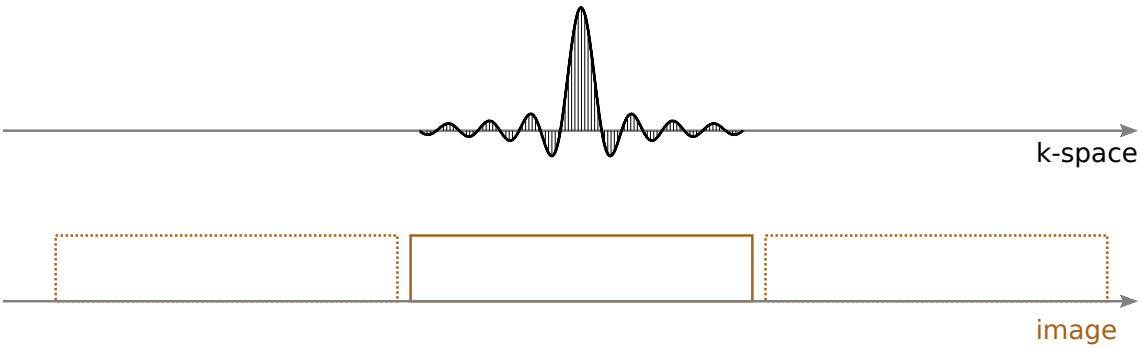

Figure 2.18: Visualization of the effects of discretization of a one-dimensional signal. The sinc-shaped signal is presented in frequency space (top) with its image representation resulting from an inverse Fourier transform (bottom). The discretized signal is indicated by stripes. The discretization leads to repeating replicas, which are marked with dotted lines. Depending on the sampling rate of the signal in k-space, these replicas can overlap with the original image leading to infolding artifacts. Figure modified from [13].

$$\mathrm{FoV} < \frac{1}{\Delta k} \tag{2.78}$$

to avoid infolding artifacts. The Fourier pixel-size representing the largest voxel dimension while still avoid infolding artifacts and follows with

$$\Delta x = \frac{1}{N\Delta k}. \tag{2.79}$$

Finite Sampling Following the discussion of the influence of discrete sampling on the reconstruction Equation (2.72) still assumes an infinite acquisition. This is practically impossible because the frequency spectrum can only be measured to a limited bandwidth $N\Delta k$. The sampling from Equation (2.73) therefore becomes

$$k \in D = \left\{ n\Delta k,\ -\frac{N}{2} \leq n < \frac{N}{2} \right\}, \tag{2.80}$$

leading to two main effects on the reconstruction: First, measured $S(n\Delta k) = S[n]$ and not measured Fourier coefficients $c[n] = c(\Delta k)$ change Equation (2.74) to [15, p.193]

$$\rho(x) = \Delta k \sum_{n=-\frac{N}{2}}^{\frac{N}{2}-1} S[n] \mathrm{e}^{2\pi i n \Delta k x} + \sum_{n<-\frac{N}{2};\ n\geq\frac{N}{2}} c[n] \mathrm{e}^{2\pi i n \Delta k x}. \tag{2.81}$$

The reconstruction becomes non-unique providing multiple possible solutions. Taking the minimum-norm as a constraint for finding a reconstruction, the frequencies $c[n]$

vanish [15, p.194], resulting in the Fourier reconstruction formula:

$$\rho(x) = \Delta k \sum_{n=-\frac{N}{2}}^{\frac{N}{2}-1} S[n] \mathrm{e}^{2\pi i n \Delta k x}, \ |x| < \frac{1}{\Delta k}\,, \tag{2.82}$$

which represents a discrete Fourier transform (DFT),

$$\rho(m) = \sum_{n=-\frac{N}{2}}^{\frac{N}{2}-1} S[n] \mathrm{e}^{\frac{2\pi i n m}{N}}, \ -\frac{N}{2} \leq m < \frac{N}{2}\,, \tag{2.83}$$

for a normalization factor of $\Delta k = 1$.

The second effect of finite sampling is similar to cutting off frequencies of a sinc pulse, like discussed in Section 2.1.3. Because the frequency representation of ρ extends the sampling limit N, the finite sampling results in discontinuities of the underlying derivatives at the k-space edges.

With the convolution property of the Fourier transform [15, p.31], the finite sampling can be understood as the multiplication of the infinite signal $S(k)$ with a rectangular function $\Pi(k)$ in frequency space:

$$\begin{aligned} FT(S(k) \cdot \Pi(k)) &= FT(S(k)) * FT(\Pi(k)) \\ &= FT(S(k)) * \mathrm{sinc}(x)\,. \end{aligned} \tag{2.84}$$

This corresponds to a convolution of the reconstructed object with a sinc-kernel and introduces ringing artifacts that are referred to as Gibbs ringing. This effect is demonstrated on a numerical phantom geometry in Figure 3.4.

MRI as Inverse Problem

Although fast (discrete) Fourier transform (FFT)-based reconstruction is computationally efficient, it requires fully-sampled data which can be time-consuming to acquire. An alternative approach is to formulate image reconstruction as an inverse problem. This strategy is more generic and enables MR image reconstruction from undersampled data with the potential to incorporate PI models. This leads to a dramatic improvement in MRI speed.

To give an intuitive understanding of these concepts, this section first introduces a reconstruction as an inverse problem. It gives rise to a large variety of advanced reconstruction techniques that incorporate complex signal models specially designed for QMRI application.

PI was introduced in Section 2.1.7 and is based on multiple receive channels. Therefore, Equation (2.59) is extended to M receivers with their sensitivity $c_j(\boldsymbol{r})$ for $j \in [0, M]$. This leads to the signal

$$y_j(\boldsymbol{k}) = \int_{\text{object}} \rho(\boldsymbol{r}) c_j(\boldsymbol{r}) \mathrm{e}^{-2\pi i \boldsymbol{k}\boldsymbol{r}} \mathrm{d}\boldsymbol{r} \ . \tag{2.85}$$

It describes a forward problem with a known object $\boldsymbol{\rho}$ and an unknown received signal $\boldsymbol{y}_j$ for the j-th coil. Equation (2.85) can be reformulated to

$$\boldsymbol{y} = \mathcal{P}\mathcal{F}\mathcal{C}(\boldsymbol{c},\boldsymbol{\rho}) \ , \tag{2.86}$$

with the coil sensitivities $\boldsymbol{c}$. The pattern operator $\mathcal{P}$ includes the information about the sampling trajectory $\boldsymbol{k}$. The Fourier operator $\mathcal{F}$ performs a Fourier transformation and the coil-profile operator C incorporates the information about the coil-sensitivities $\boldsymbol{c}$. All operators are illustrated in Figure 4.1. Under the assumption of known $\boldsymbol{c}$, the operators $\mathcal{P}\mathcal{F}\mathcal{C}$ can be combined:

$$\mathcal{A} = \mathcal{P}\mathcal{F}\mathcal{C} \ . \tag{2.87}$$

This simplifies an inverse formulation of the problem where the object $\boldsymbol{\rho}$ is unknown and should be estimated from the measured signal $\boldsymbol{y}$ while knowing $\mathcal{A}$:

$$\boldsymbol{\rho} = \mathcal{A}^{-1}\boldsymbol{y} \ . \tag{2.88}$$

These problems are typically ill-posed because noise and undersampling makes their solution non-unique. Instead of solving it with a traditional inverse, the solution needs to be found with respect to a metric. By choosing an Euclidean norm, the inverse of $\mathcal{A}$ is approximated by the Moore-Penrose inverse $\mathcal{A}^+$,

$$\mathcal{A}^{-1} \approx \mathcal{A}^+ = (\mathcal{A}^H\mathcal{A})^{-1}\mathcal{A}^H \ , \tag{2.89}$$

with the adjoint $(\cdot)^H$. The solution $\boldsymbol{\rho} = \mathcal{A}^+\boldsymbol{y}$ corresponds to the solution found with an iterative least-squares optimization with the cost functional

$$\hat{\boldsymbol{\rho}} := \underset{\boldsymbol{\rho}}{\operatorname{argmin}} \|\mathcal{A}(\boldsymbol{c},\boldsymbol{\rho}) - \boldsymbol{y}\|_2^2 \ . \tag{2.90}$$

In general, noise in MRI signal results either from the resistance of the receiver coils, the preamplifier of the system or inductive and dielectric losses in the measured object [54]. Together with complex sampling schemes, they make the inverse problem ill-conditioned.

This requires additional prior knowledge to be added as regularization to stabilize the convergence of the optimization. An example is additional l_2 regularization which improves the robustness to Gaussian distributed noise in conventional MRI:

$$\hat{\boldsymbol{\rho}} := \underset{\boldsymbol{\rho}}{\operatorname{argmin}} \|\mathcal{A}\boldsymbol{\rho} - \boldsymbol{y}\|_2^2 + \underbrace{\|\rho\|_2^2}_{\text{regularization}} . \tag{2.91}$$

Reconstruction by Nonlinear Inversion

In the previous section, the concept of reconstruction is introduced from the perspective of an inverse problem. In Section 2.1.9, the model described by Equation (2.86) is linear because all operators in $\mathcal{A}$ are linear due to the assumption of known coil-sensitivities. In practice, this assumption requires prior knowledge about the coil sensitivities. They are either estimated in a separate calibration scan or from a calibration region within the acquired data $\boldsymbol{y}$. The latter is based on popular techniques like ESPIRiT [55]. They do not exploit all the acquired information and skip data outside of the calibration area. This potentially reduces the quality of the sensitivity maps [36]. A solution is to exploit the coil-sensitivity signal model in Equation (2.86) and not just determine the image $\boldsymbol{\rho}$, but the coils $\boldsymbol{c}$ simultaneously. This renders Equation (2.86) to be nonlinear and ill-conditioned. It requires regularization and iterative solution strategies. While techniques like JSENSE [56] integrate the coil-sensitivities as polynomials in the cost function, the focus of this work lies on regularized nonlinear inverse reconstruction (NLINV) [36] with $\boldsymbol{c}$ in image space and Sobolev norm based smoothness penalty $\boldsymbol{Q}$

$$(\hat{\boldsymbol{\rho}},\hat{\boldsymbol{c}}) = \underset{(\boldsymbol{\rho},\boldsymbol{c})}{\operatorname{argmin}} \|\mathcal{P}\mathcal{F}\mathcal{C}(\boldsymbol{c},\boldsymbol{\rho}) - \boldsymbol{y}\|_2^2 + \alpha\|\boldsymbol{\rho}\|_2^2 + \alpha\boldsymbol{Q}(\boldsymbol{c}) , \tag{2.92}$$

scaled by regularization factor α. The nonlinear operator has the form

$$\mathcal{A}\boldsymbol{x} = \mathcal{P}\mathcal{F}\mathcal{C}\boldsymbol{x} = \boldsymbol{y}, \quad \text{with } \boldsymbol{x} = \begin{pmatrix} \boldsymbol{\rho} \\ \boldsymbol{c}_1 \\ \vdots \\ \boldsymbol{c}_N \end{pmatrix} , \tag{2.93}$$

and maps

$$\mathcal{A} : \boldsymbol{x} \mapsto \begin{pmatrix} \mathcal{P}\mathcal{F}\boldsymbol{c}_1\boldsymbol{\rho} \\ \mathcal{P}\mathcal{F}\boldsymbol{c}_2\boldsymbol{\rho} \\ \vdots \\ \mathcal{P}\mathcal{F}\boldsymbol{c}_N\boldsymbol{\rho} \end{pmatrix} . \tag{2.94}$$

In NLINV, the cost function in Equation (2.92) is solved with an iteratively regularized Gauss-Newton method (IRGNM) [57, 58]. This algorithm linearizes the nonlinear problem in each Gauss-Newton step around the current solution x_n for step n:

$$\mathcal{A}(\boldsymbol{x} + \mathrm{d}\boldsymbol{x}) \approx D\mathcal{A}(\boldsymbol{x}_n)\mathrm{d}\boldsymbol{x} + \mathcal{A}(\boldsymbol{x}_n) , \tag{2.95}$$

with the Jacobian $D\mathcal{A}$ at $\boldsymbol{x}_n$ and the update $\mathrm{d}\boldsymbol{x}$. The linearized optimization problem in each step n,

$$\hat{\boldsymbol{x}}_{n+1} = \underset{\boldsymbol{x}}{\operatorname{argmin}} \|D\mathcal{A}(\boldsymbol{x}_n)(\boldsymbol{x} - \boldsymbol{x}_n) + \mathcal{A}(\boldsymbol{x}_n) - \boldsymbol{y}\|_2^2 + \alpha_n\|\boldsymbol{x} - \boldsymbol{x}_n\|_2^2 + \alpha_n\boldsymbol{Q}(\boldsymbol{c}) , \tag{2.96}$$

is solved using iterative algorithms like the conjugate gradient method (CG) or a fast iterative shrinkage/thresholding algorithm (FISTA).
While the solution $\boldsymbol{x}_n$ will have a low accuracy for small n, a strong regularization enforces a strong prior knowledge about $\boldsymbol{c}$ and $\boldsymbol{\rho}$ which stabilizes the convergence of the optimization. Keeping a constantly high regularization for larger n leads to biases introduced to the solution of the optimization. Therefore, the IRGNM iteratively reduces the regularization strength with increasing n following

$$\alpha_n = \alpha_0 q^n , \tag{2.97}$$

with the initial regularization scaling α_0 and factor $q \in (0,1)$.

2.2. Quantitative MRI

Depending on the sequence that is executed, MRI can provide images with various contrasts for the same measured object. The contrast depends on the physical properties of the measured tissue, hardware characteristics of the MRI system and the executed sequences. This complexity and high degree of freedom in choosing arbitrary sequences makes MRI one of the most versatile imaging techniques in the clinical application. However, this leads to complex protocols in the daily clinical routine and a difficult interpretation of the resulting images. QMRI aims to reduce the complexity of the interpretation of the images by measuring physical properties of the tissue or hardware. It requires sequences capable

of encoding the desired characteristics and reconstructions that incorporates physical knowledge to extract the information. This section introduces some common sequences in QMRI, which are sensitive to various physical effects. It also explains how they are designed to be robust against not desired characteristics.

2.2.1. Conventional Methods

Conventional QMRI typically exploits sequences that are sensitive to a single property of the tissue or hardware and which are robust against most other occurring physical effects. This conservative approach ensures to determine a single characteristic accurately while avoiding coupled physical effects biasing the results. After the acquisition of data with a specific sequence sensitive to a single parameter, the reconstruction in conventional QMRI involves two steps:

1. Reconstruction of intermediate images from the acquired data
2. Pixel-wise fitting of an analytical model to the intermediate images to extract the parameter.

A schematic drawing of this procedure is shown to Figure 2.19.

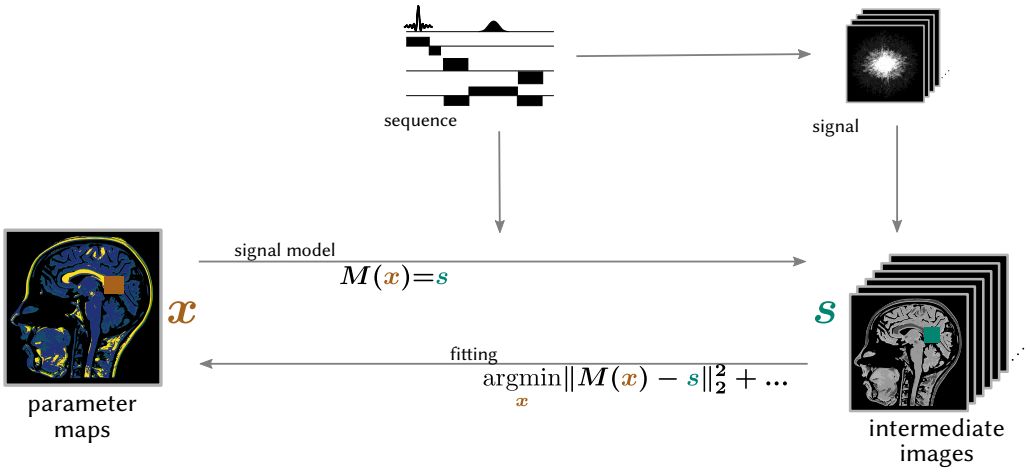

Figure 2.19: Visualization of a conventional QMRI workflow. A special sequence is designed to provide an analytical signal model $\boldsymbol{M}(\boldsymbol{x})$. Fully-sampled datasets for multiple points in time are measured and reconstructed using an inverse Fourier transform. Afterwards, the derived analytical signal model is fitted pixel-wisely to the reconstructed intermediate images, which results in the parameter maps $\boldsymbol{x}$.

The analytical signal model applied in the pixel-wise fitting is derived from the Bloch equations for the special sequence that were used during acquisition. Its derivation

typically involves assumptions that simplify the underlying physical processes. Common assumptions are:

1. **Hard-Pulses**: No relaxation takes place during the execution of RF pulses.
2. **Perfect Spoiling**: The transversal magnetization vanished completely during a spoiling event.
3. **Infinite Short Sampling**: All samples of an echo are acquired at the same time.

The pixel-wise fitting approach in conventional QMRI requires high quality intermediate images. They are typically reconstructed from the raw dataset with an inverse Fourier transform. Reconstruction with artifacts can alter the signal evolution of a single pixel and reduce the accuracy of the physical parameter maps. The reconstruction with the inverse Fourier transform requires fully-sampled k-spaces to avoid the artifacts. Measurements involving PI [35] can speed up the acquisition, but still require a lot of redundant information to be measured, especially for higher frequencies.
An example of conventional QMRI are sequences for gold-standard estimation of relaxation parameters.

Relaxation Parameter Mapping

Gold-Standard T_1 Mapping Gold-Standard T_1 mapping sequences are based on inversion-recovery (IR) single-echo spin-echo sequences. A visualization of their sequence diagram is shown in Figure 2.20. They consist of an initial adiabatic HS1 inversion pulse with varying TI. The inversion pulse leads to a high T_1 sensitivity. The single-echo acquisition with constant TE shows the same T_2 effect on every acquired sample in time, which makes the pixel-fitting robust against T_2 variations. Addtionally, spin-echo sequences are by design insensitive to T_2^* because the π-RF pulse refocuses the dephasing effects introduced through inhomogeneities of the main magnetic field. The T_1 and T_2 contrast is not affected by previous measurements because a full relaxation to M_0 is enforced by a long TR. Inhomogeneities in B_1 show differences between individual pixels, but are constant for each in time and therefore do not affect the pixel-wise fitting.

In summary, the signal of an IR single-echo spin-echo sequence with varying TI encodes only T_1 and is robust against T_2, B_0 and B_1 inhomogeneitities. The analytical model for

the temporal evolution of the signal M_{xy} derived from the Bloch equations for such a sequence follows

$$M_{xy}(t) \propto M_z(t) = M_0 \cdot \left(1 - e^{-t/T_1}\right) , \tag{2.98}$$

with t given with TI.

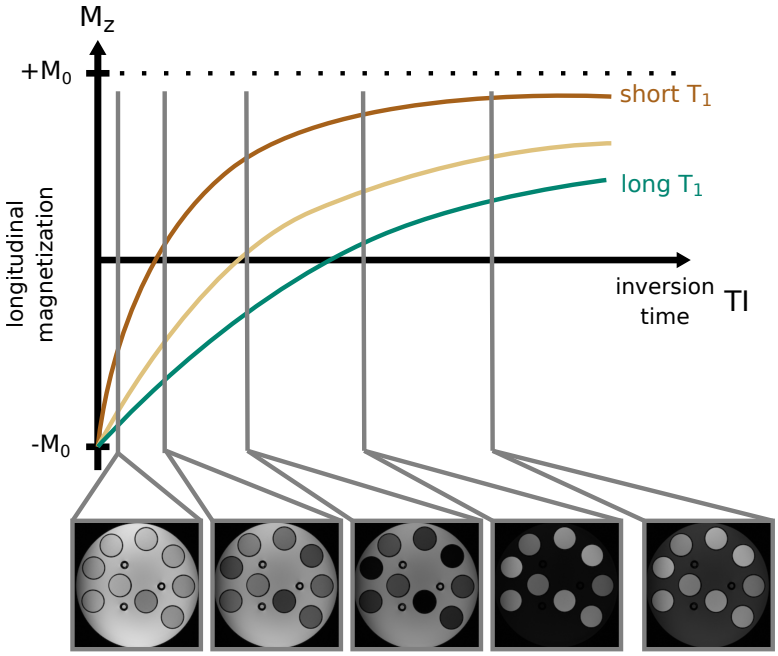

Figure 2.20: Visualization of the signal during a gold-standard T_1 mapping acquisition representing the regrowing longitudinal magnetization. Phantom acquisitions for different TI are added on the bottom showing varying signal intensities dependent on the R_1 relaxation rate of the individual pixels. Three exemplary regrowing curves are plotted on the top for short to long T_1 values. Figure modified from [13].

Gold-Standard T_2 Mapping The gold-standard T_2 mapping technique is based on a single-echo spin-echo sequence with varying TE. It shows a reduced image contrast in time encoding the T_2 relaxation, as presented in Figure 2.21. The spin-echo sequence is robust against T_1 variations due to the magnetization relaxing back to M_0 for long TR. The same initial $\pi/2$ pulse excites the magnetization for each acquisition. This pulse can be affected by B_1 inhomogeneities, which leads to spatial variations of the contrast. Nevertheless, the temporal evolution of each individual voxel is not affected making the pixel-wise fitting robust against B_1 inhomogeneities. The gold-standard T_2 sequence is

robust against the inhomogeneity effect in T_2^* because of their refocusing π-RF pulse.

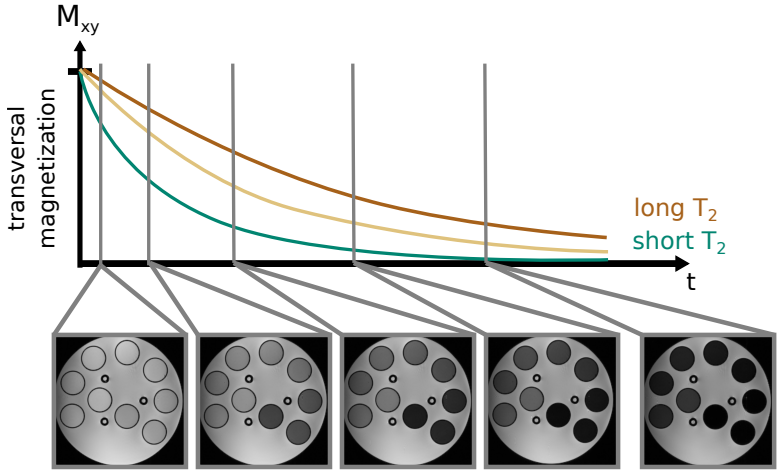

Figure 2.21: Visualization of the signal during a gold-standard T_2 mapping acquisition representing the decreasing of the transversal magnetization. Phantom acquisitions for different TE are added on the bottom showing varying signal intensities dependent on the R_2 relaxation rate of the individual pixels. Three exemplary signal curves are plotted on the top for short to long T_2 values. Figure modified from [13].

In summary, the signal change between acquisitions with varying TE encodes only T_2 information and the pixel-wise fitting is robust against T_1, B_0 and B_1. The analytical model for the temporal evolution of the signal M_{xy} derived from the Bloch equations for the variable TE single-echo spin-echo sequence follows

$$M_{xy}(t) = M_0 \cdot e^{-t/T_2} \,, \tag{2.99}$$

with t defined by TE.

B_1 Mapping

Field inhomogeneities of the RF transmitter field B_1 lead to spatially different excitations. This modifies the received signal for sequences sensitive to B_1 and becomes important for QMRI to model or compensate introduced biases. Many analytical models are based on knowledge about the effective flip angle. This does not only include B_1, but also the slice profile in the presence of slice-selective excitations. While the latter is known from the shape of the RF pulse and active gradients, B_1 often needs to be measured.

The concept of B_1 mapping is to exploit two sequences whose varying contrasts encode B_1. Many methods have been developed over the years that can be classified in magnitude-

and phase-based techniques [59]. This introduction focuses on a gold-standard gradient recalled echo double-angle (GRE-DA) and a fast preconditioned RF pulse mapping technique with FLASH readout.

Gradient Recalled Echo Double-Angle The GRE-DA technique exploits the differences of two gradient recalled echo (GRE) acquisitions acquired with two small flip angles: α and 2α. Both acquisitions need to be identical in all other parameters to avoid further influences on the image. The contrast of GRE-based sequences depends on the relaxation time T_1. This can be reduced by increasing TR to about five times the longest T_1 relaxation present in the measured object. It avoids the creation of a T_1 dependent steady-state and allows the magnetization to recover to its equilibrium M_0. GRE-DA is assumed to be robust against B_0 inhomogeneities because dephasing affects both acquired images equally. The measured image contrasts can be approximated with

$$\rho_1 = M_0 \sin(\alpha) \tag{2.100}$$

$$\rho_2 = M_0 \sin(2\alpha). \tag{2.101}$$

The ratio

$$r = \frac{\rho_1}{\rho_2} = \frac{1}{2\cos(\alpha)} \tag{2.102}$$

describes the relative change in B_1 and can be converted to absolute values with the definition of the flip angle α. As an example for a block pulse with flip angle $\alpha = \gamma B_1 t$, the absolute B_1 becomes [60]

$$B_1 = \frac{1}{\gamma t} \cos^{-1}\left(\frac{1}{2r}\right). \tag{2.103}$$

Preconditioned RF Pulse While GRE-DA provides accurate B_1 values, its long TR leads to long acquisition times. If its T_1 robustness is not compromised, they are too long for in vivo acquisitions. While techniques exist to reduce the TR based on compensation pulses [61], current vendor implementations are based on preconditioned RF pulses with spoiled FLASH readout [62]. A schematic drawing of the sequence can be found in Figure 2.22.

Similar to the GRE-DA technique, the preconditioned RF pulse sequence is based on two GRE acquisitions with the contrasts ρ_{PD} and $\rho_{\mathrm{SS\,Pre}}$. Both have the same flip angle but the acquisition of $\rho_{\mathrm{SS\,Pre}}$ starts with an initial slice-selective preconditioning (SS-

Pre) RF pulse and a spoiling block removes any transversal macroscopic magnetization. This SS-Pre pulse flips the magnetization with a high flip angle α^{nom} ($\approx 80°$) changing the image contrast from the GRE acquisition to start from M_z instead of M_0. Ignoring partial saturation, relaxation and off-resonance effects, the individual images become proportional to the initial z-component of the magnetization [62, 63]:

$$\rho_{\text{PD}} \propto M_0 \tag{2.104}$$

$$\rho_{\text{SS Pre}} \propto M_z. \tag{2.105}$$

Assuming the same proportionality constant, the ratio between both images follows [62]

$$\frac{\rho_{\text{SS Pre}}}{\rho_{\text{PD}}} = \cos(r \cdot \alpha^{\text{nom}}) \tag{2.106}$$

$$\Leftrightarrow r = \cos^{-1}\left(\frac{\rho_{\text{SS Pre}}}{\rho_{\text{PD}}}\right) / \alpha^{\text{nom}}, \tag{2.107}$$

with the relative B_1 change r and the nominal SS-Pre pulse flip angle α^{nom}. The absolute B_1 follows similar to Equation (2.103) with the knowledge of the applied RF pulse.

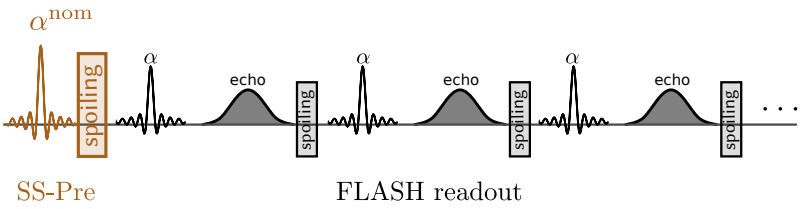

Figure 2.22: Visualization of a simplified sequence diagram for a B_1 Mapping sequence based on preconditioned RF pulses. The SS-Pre module is colored with the flip angle of α^{nom} and its spoiling event. The FLASH readout with different flip angle α follows directly afterwards similar to Figure 2.16.

While this sequence allows for fast B_1 mapping, especially the assumption of no longitudinal relaxation does not hold for short T_1 values in measured objects. Here, $\rho_{\text{SS Pre}} \propto M_z$ breaks because the whole acquisition of the image does not happen in a steady-state but rather in a transient state relaxing back to the initial M_0. B_0 inhomogeneities and T_2 effects are assumed to be weak because of the spoiling of transversal magnetization during the FLASH readout.

B_0 Mapping

In conventional B_0 field mapping, two images ρ_{TE_1} and ρ_{TE_2} are acquired with GRE sequences rather than spin-echoes, which are too robust against field inhomogeneities. The acquisitions of the complex images ρ_{TE_1} and ρ_{TE_2} differ in TE leading to a phase difference

$$\Delta\phi = -\gamma B_0(\mathrm{TE}_2 - \mathrm{TE}_1) \quad \text{with} \quad \mathrm{TE}_2 < \mathrm{TE}_1\,, \tag{2.108}$$

which encodes the B_0 information and is exploited to determine the relative field map ΔB_0 [64]:

$$\Delta B_0 = \frac{\arg(\rho_{\mathrm{TE}_2}\rho^*_{\mathrm{TE}_1})}{-(\mathrm{TE}_2 - \mathrm{TE}_1)}\,, \tag{2.109}$$

with the complex conjugate $(\cdot)^*$.
By focussing on the phase difference and exploiting short TE, this sequence is robust against variations in T_2, which influence the magnitude but not the phase. In addition, they are typically much longer than the used TE. T_1 and B_1 both only affect the magnitude image of GRE sequences. Therefore, both acquisitions are influenced in the same way. This requires the difference between both echo times to fulfill: $(\mathrm{TE}_2 - \mathrm{TE}_1) \ll T_1$.

2.2.2. Model-Based Reconstruction

Compared to conventional QMRI, which was introduced in Section 2.2.1, model-based reconstruction does not require a two-step parameter estimation, but integrate the physical model into the reconstruction directly. They formulate the parameter estimation and reconstruction as a single inverse problem allowing to determine quantitative parameters directly from the acquired raw data. This reduces the modelling of the temporal signal evolution to only a few parameters and makes efficient use of the acquired data avoiding the acquisition of redundant data. Model-based reconstructions bypass the intermediate image reconstruction step from conventional QMRI techniques shown in Figure 2.19. A visualization of a model-based acquisition/reconstruction pipeline is presented in Figure 2.23.

Many model-based reconstruction techniques exist. The complexity of their forward models differs and allows to classify them in two basic categories: The linear subspace [65–69] and nonlinear model-based methods [5–8, 70], which are further discussed in the following.

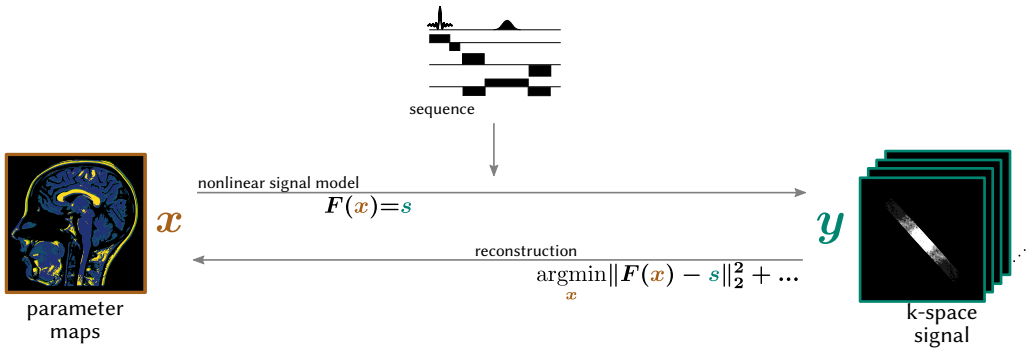

Figure 2.23: Visualization of a model-based reconstruction workflow. A special sequence is designed providing an analytical signal model. This is further combined with a signal acquisition model in the operator $\boldsymbol{F}$. After measurement of undersampled datasets for multiple time points, the parameter maps $\boldsymbol{x}$ are calculated directly from the measured data $\boldsymbol{y}$.

Linear Subspace Techniques

Linear subspace techniques are based on simulated dictionaries $\boldsymbol{X}$ incorporating nonlinear signal evolutions. Every possible combination of the desired physical quantities within the measured object needs to be covered by the simulated time series in $\boldsymbol{X}$. The aim of subspace techniques is to find an orthonormal basis $\boldsymbol{\Phi} = [\phi_1 \ \ldots \ \phi_T]$ in time [71],

$$\boldsymbol{X} = \boldsymbol{\Phi}\boldsymbol{\Phi}^H\boldsymbol{X} \, . \tag{2.110}$$

A K-dimensional subspace $\boldsymbol{\Phi}_K = \text{span}\{\phi_1 \ \ldots \ \phi_T\}$ is designed to approximate $\boldsymbol{\Phi}$ to an error limit ϵ [71]:

$$\|\boldsymbol{X} - \boldsymbol{\Phi}_K\boldsymbol{\Phi}_K^H\boldsymbol{X}\| < \epsilon \, . \tag{2.111}$$

$\boldsymbol{\Phi}_K$ is typically found with a principal component analysis (PCA) of $\boldsymbol{X}$.
During the reconstruction, the temporal basis coefficients $\boldsymbol{\alpha} = \boldsymbol{\Phi}_K^H\boldsymbol{x}$ are optimized for

$$\hat{\boldsymbol{\alpha}} = \underset{\boldsymbol{\alpha}}{\operatorname{argmin}}\|\boldsymbol{y} - \boldsymbol{F}\boldsymbol{\Phi}_K\boldsymbol{\alpha}\|_2^2 + \ldots \, , \tag{2.112}$$

Overall, the otherwise nonlinear forward model $\boldsymbol{F}$ [71] is linearized

$$\boldsymbol{y} = \boldsymbol{F}\boldsymbol{x} \approx \boldsymbol{F}\boldsymbol{\Phi}_K \underbrace{\boldsymbol{\Phi}_K^H\boldsymbol{x}}_{\boldsymbol{\alpha}} \, . \tag{2.113}$$

with the physical parameters $\boldsymbol{x}$.
The linear nature of the subspace models makes them computationally efficient for

a large variety of different signal models $\boldsymbol{F}$. Nevertheless, linearization represents an approximation of the nonlinear model. This may require more parameters in cases of complex signal dynamics making the approximation less efficient than the evaluation of the nonlinear model itself [8].

Nonlinear Model-based Reconstructions

In comparison to linear subspace models, nonlinear model-based reconstructions do not linearize the temporal evolution of the signals but include the underlying nonlinear physical model directly into the reconstruction. While some techniques exploit analytical signal models [9, 10, 72] that are derived from the Bloch equations for specific sequences (see Table 2.1) others rely on generic simulations [73, 74].

Table 2.1: Listing of various signal models encoding a wide variety of physical parameters. The models are derived from the Bloch equation for special sequences and are taken from [8].

R_1:	$a - (1+a) \cdot e^{\frac{-t_n R_1}{a}}$
R_2:	$e^{-R_2 t_n}$
R_2^*:	$e^{-R_2^* t_n}$
B_0:	$e^{i2\pi \cdot f_{B_0} t_n}$
Chemical Shift:	$\sum_p a_p e^{i2\pi f_p t_n}$
$\boldsymbol{v}$:	$e^{i\boldsymbol{v} \cdot \boldsymbol{V}_n}$
D:	$e^{-\boldsymbol{b}_n^T D \boldsymbol{b}_n}$

Most nonlinear model-based reconstructions differ in their complexity of the data sampling and in the integration of coil-profiles.

Reconstruction without Parallel Imaging Model Many model-based reconstructions treat the coil-sensitivies $\boldsymbol{x}_c$ as prior knowledge [5–7, 70, 72]. They are either estimated in a separate calibration scan or are calculated from a calibration region within the acquired dataset itself [55]. The reconstruction is performed as an iterative optimization following

$$\hat{\boldsymbol{x}} = \underset{\boldsymbol{x}_p}{\operatorname{argmin}} \| \boldsymbol{y} - \mathcal{P}\mathcal{F}\mathcal{C}(\boldsymbol{x}_c, \mathcal{M}(\boldsymbol{x}_p)) \|_2^2 + \dots \,, \tag{2.114}$$

with a pattern operator $\mathcal{P}$ that includes information about the sampling trajectory. The Fourier operator $\mathcal{F}$ performs a Fourier transform into frequency space. The coil-operator

C multiplies the signal with the known coil sensitivities. Finally, the nonlinear physics model $\mathcal{M}$ takes the parameters $\boldsymbol{x}_p$ as input and $\boldsymbol{y}$ represents the measured data. This method takes the assumption that the whole echo is acquired at a single point in time. It is based on the idea that dynamics within a readout do not have a propagating effect through the entire acquisition, which holds for most sequences. Additionally, the readout time is much shorter compared to the T_2 relaxation for the radial sampling schemes.

Reconstruction Including a Parallel Imaging Model Other techniques jointly reconstruct the coil-profiles $\boldsymbol{x}_c$ and the physical parameters $\boldsymbol{x}_p$ [9, 10] based on techniques like NLINV, which is introduced in Section 2.1.9. They incorporate additional prior knowledge about the smoothness of the sensitivities with a Sobolev norm regularization $\boldsymbol{Q}$ scaled by a scalar α. The cost function of the optimization follows

$$\hat{\boldsymbol{x}} = \underset{\boldsymbol{x}_p, \boldsymbol{x}_c}{\operatorname{argmin}} \|\boldsymbol{y} - \mathcal{P}\mathcal{F}C(\boldsymbol{x}_c, \mathcal{M}(\boldsymbol{x}_p))\|_2^2 + \alpha \boldsymbol{Q}(\boldsymbol{x}_c) + \dots . \tag{2.115}$$

Other Types Besides the two major classes defined by the treatment of coil-sensitivities, most of the model-based reconstruction techniques rely on analytically derived signal models. While some integrate full size simulations into the reconstruction process [73, 74], even these simulation-based methods differ in their complexity. The method developed by Ben-Eliezer in 2016 [73] takes the assumption of a single TE for a whole echo readout and coil-sensitivities as prior knowledge, magnetic resonance spin tomography in time-domain (MR-STAT) [74] assumes a single coil profile but simulates each sampling point along the trajectory of the acquisition. Further reconstruction techniques, like magnetic resonance fingerprinting (MRF) [11], incorporate simulations stored in large look-up tables but rely on a classical two-step QMRI reconstruction processes. They speed up the acquisition by exploiting the incoherence between the noise from undersampling artifacts and a signal acquired with a pseudo-random variable flip angle sequence. The reconstruction in MRF is performed as an inverse Fourier transform. Afterwards, the signal traces (fingerprints) are looked up pixel-wisely in a previously simulated dictionary.

2.3. Simulation of Spin Dynamics

Following the idea of model-based reconstructions and QMRI, the knowledge about the temporal evolution of the macroscopic magnetization can be exploited to measure quantitative parameters. Generalizing the techniques beyond analytical models requires

simulations of the underlying Bloch equation and extension, which is presented in Section 2.1.6.

This section is focused on different techniques for integrating the Bloch equations (2.46). More information about different methods that are simulating in the frequency domain was summarized in [75, 76].

For a simplified notation, the Bloch equations (2.46) are reformulated to a homogeneous ODE:

$$\frac{\mathrm{d}\boldsymbol{M}(\boldsymbol{c},t)}{\mathrm{d}t} = \boldsymbol{A}(\boldsymbol{c},t)\ \boldsymbol{M}(\boldsymbol{c},t)\ , \tag{2.116}$$

with the magnetization vector

$$\boldsymbol{M}(\boldsymbol{c},t) = \begin{pmatrix} M_x(\boldsymbol{c},t) \\ M_y(\boldsymbol{c},t) \\ M_z(\boldsymbol{c},t) \\ 1 \end{pmatrix}, \tag{2.117}$$

and its constant components $\boldsymbol{c} = (R_1\ R_2\ M_0)$ as well as the system matrix

$$\boldsymbol{A}(\boldsymbol{c},t) = \begin{pmatrix} -R_2 & \gamma B_z(t) & -\gamma B_y(t) & 0 \\ -\gamma B_z(t) & -R_2 & \gamma B_x(t) & 0 \\ \gamma B_y(t) & -\gamma B_x(t) & -R_1 & M_0 R_1 \\ 0 & 0 & 0 & 0 \end{pmatrix}, \tag{2.118}$$

with the relaxation rates $R_{1,2} = 1/T_{1,2}$ and the external magnetic field $\boldsymbol{B} = (B_x\ B_y\ B_z)^T$.

2.3.1. Rotation Matrix Approaches

The first type of Bloch simulations discussed in this work is based on rotation matrices [77]. They rely on the idea that the system matrix $\boldsymbol{A}$ in Equation (2.116) is approximately constant for short time intervals Δt:

$$\boldsymbol{A}(\boldsymbol{c}, t \rightarrow t + \Delta t) = \text{const.} \tag{2.119}$$

In this piece-wise constant Bloch step, the physical effects of relaxation, excitation and gradients can be modelled with basic rotations $\boldsymbol{R}_i$ along the individual axis of the rotating frame $i \in (x,y,z)$. This concept is visualized in Figure 2.24.

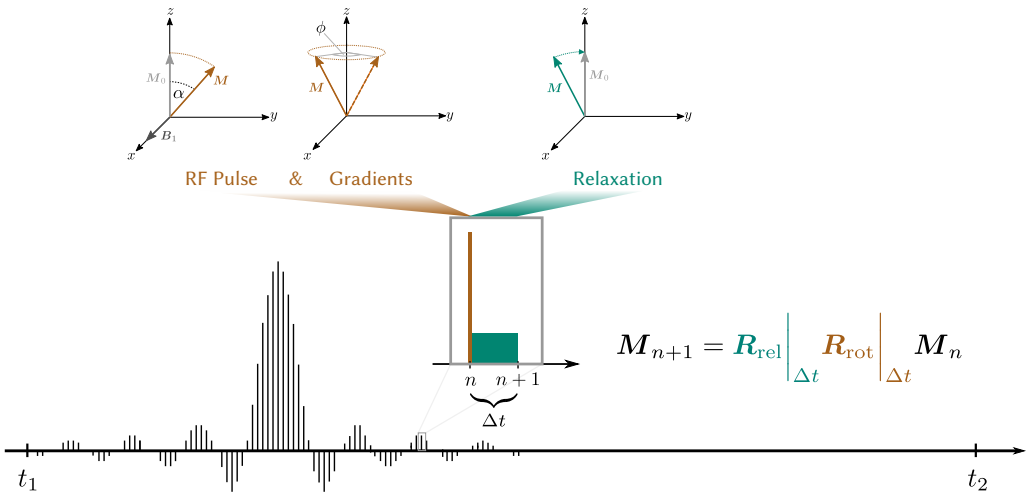

Figure 2.24: Visualization of the concept of asymmetric operator splitting (ASY). The dynamics of the Bloch equations are approximated in order to be piecewise constant during small time intervals Δt. The evolution of the magnetization is described by rotations for RF pulses and gradients as well as exponential terms for relaxation. Both effects are described by operators executed in an asymmetric order transforming the magnetization from step n to $n+1$.

RF-Pulse Effects The rotation effects through RF pulses can be split in their components around all three axis depending on its phase ϕ, off-resonance frequency $\Delta\omega = \gamma B_0 - \omega_{\mathrm{rf}}$ and flip angle $\Delta\alpha$. The effective RF field axis is tipped by

$$\theta = \arctan\left(\frac{\Delta\omega \cdot \Delta t}{\Delta\alpha}\right) \tag{2.120}$$

and the effective flip angle becomes

$$\Delta\alpha' = \sqrt{\Delta\omega^2 + \left(\frac{\Delta\alpha}{\Delta t}\right)^2}\,. \tag{2.121}$$

Using the notation $\boldsymbol{M}_n$ for the magnetization vector before the RF excitation and $\boldsymbol{M}_{n+1}$ after, the RF effect can be described by

$$\begin{aligned} \boldsymbol{M}_{n+1} &= \boldsymbol{R}_y(\theta)\boldsymbol{R}_z(\phi)\boldsymbol{R}_x(\Delta\alpha')\boldsymbol{R}_z(-\phi)\boldsymbol{R}_y(-\theta)\boldsymbol{M}_n && (2.122)\\ &= \boldsymbol{R}_{\mathrm{RF}}(\boldsymbol{M}_n, \Delta t, \ldots)\,. && (2.123) \end{aligned}$$

Free-Precession Effects Free-precession introduced through field inhomogeneities and gradient effects are also modelled with rotations. Instead of acting on multiple axis,

they rotate only around the z-axis. Gradients $\boldsymbol{G}$ introduce a rotation angle θ_g at location $\boldsymbol{r}$ following

$$\theta_g = \gamma \boldsymbol{r} \int_t^{t+\Delta t} \boldsymbol{G}(\boldsymbol{r},\tau)\mathrm{d}\tau. \tag{2.124}$$

Field inhomogeneities $\Delta\boldsymbol{B}$ introduce a rotation around z by the angle θ_i within Δt:

$$\theta_i = \gamma \Delta \boldsymbol{B}(\boldsymbol{r})\hat{\boldsymbol{e}}_z \Delta t \ . \tag{2.125}$$

Their combined effects modify the magnetization in the piece-wise constant Bloch step according to

$$\boldsymbol{M}_{n+1} = \boldsymbol{R}_z(\theta_g)\boldsymbol{R}_z(\theta_i)\boldsymbol{M}_n \tag{2.126}$$

$$= \boldsymbol{R}_{\mathrm{prec}}(\boldsymbol{M}_n m \Delta t,\ldots) \ . \tag{2.127}$$

For an efficient simulation, the two rotations described by Equations (2.123) and (2.127) can be combined to

$$\boldsymbol{R}_{\mathrm{rot}} = \boldsymbol{R}_{\mathrm{RF}}\boldsymbol{R}_{\mathrm{prec}} \ , \tag{2.128}$$

modelling all rotations within one Bloch step.

Relaxation Effects While RF and gradient effects can be modelled with rotations and can be combined in a single operator in Equation (2.128), the relaxation effects follow with separate exponential models, which are introduced in Section 2.1.5, and are described with a homogeneous component

$$\boldsymbol{R}_{\mathrm{rel,hom}}(\Delta t) = \begin{pmatrix} E_2 & 0 & 0 \\ 0 & E_2 & 0 \\ 0 & 0 & E_1 \end{pmatrix}, \tag{2.129}$$

with $E_{1,2} = e^{-\frac{\Delta t}{T_{1,2}}}$ and an inhomogeneous component

$$\boldsymbol{R}_{\mathrm{rel,non}}(\Delta t) = (M_0 - E_1)\begin{pmatrix} 0 \\ 0 \\ 1 \end{pmatrix} . \tag{2.130}$$

The relaxation dynamic therefore follows with the operator

$$\boldsymbol{M}_{n+1} = \boldsymbol{R}_{\text{rel,hom}}(\Delta t)\boldsymbol{M}_n + \boldsymbol{R}_{\text{rel,non}}(\Delta t) \tag{2.131}$$

$$= \boldsymbol{R}_{\text{rel}}(\boldsymbol{M}_n, \Delta t, \ldots) \; . \tag{2.132}$$

With the definition of operators for rotation $\boldsymbol{R}_{\text{rot}}$ and relaxation $\boldsymbol{R}_{\text{rel}}$ different rotation based simulations techniques can be designed. Methods with rotation and relaxation acting during the whole Bloch step Δt are called ASY [77]

$$\boldsymbol{M}_{n+1} = \boldsymbol{R}_{\text{rel}}\Big|_{\Delta t} \boldsymbol{R}_{\text{rot}}\Big|_{\Delta t} \boldsymbol{M}_n \; , \tag{2.133}$$

and provide a first order convergence in relation to their step size. Techniques with $\boldsymbol{R}_{\text{rot}}$ acting on $\Delta t/2$ in the beginning and end of the Bloch step are referred to as symmetric operator splitting (SY) [78]:

$$\boldsymbol{M}_{n+1} = \boldsymbol{R}_{\text{rot}}\Big|_{\Delta t/2} \boldsymbol{R}_{\text{rel}}\Big|_{\Delta t} \boldsymbol{R}_{\text{rot}}\Big|_{\Delta t/2} \boldsymbol{M}_n \; , \tag{2.134}$$

with a quadratic convergence in step size. A detailed discussion of the different operator splitting techniques, also including higher orders, was elaborated by [79].

2.3.2. Matrix Exponentials

The ODE in Equation (2.116) with the initial condition $\boldsymbol{M}(\boldsymbol{c},0) = \boldsymbol{M}_0 = M_0\hat{\boldsymbol{e}}_z$ can be formally solved by

$$\boldsymbol{M}(\boldsymbol{c},t) = \mathcal{T}\left\{e^{\int \boldsymbol{A}(\boldsymbol{c},t)\mathrm{d}t}\right\}\boldsymbol{M}_0 \; . \tag{2.135}$$

Here, $\mathcal{T}\left\{e^{\int \boldsymbol{A}(t)\mathrm{d}t}\right\}$ describes a time-ordered exponential but can be simplified to a matrix exponential for small time intervals Δt in which the system matrix $\boldsymbol{A}(\boldsymbol{c},t)$ is assumed to be constant:

$$e^{\int \boldsymbol{A}(t)\mathrm{d}t} \approx e^{\sum_n \boldsymbol{A}(\boldsymbol{c},t_n)\Delta t} \; . \tag{2.136}$$

The matrix exponential-based simulation requires the same small Bloch step assumption as the rotation approach. For each interval n, the matrix exponential $\boldsymbol{S}_{n\Delta t}$ can be calculated as follows:

$$\boldsymbol{S}_{n\Delta t} = e^{\boldsymbol{A}(\boldsymbol{c},n\Delta t)\Delta t} \; , \tag{2.137}$$

modelling the dynamics of the magnetization

$$\boldsymbol{M}(\boldsymbol{c},(n+1)\Delta t) = \boldsymbol{S}_{n\Delta t}\boldsymbol{M}(\boldsymbol{c},n\Delta t)\ . \tag{2.138}$$

A matrix exponential describes the combined effect of RF excitation, relaxation, inhomogeneities and gradients during the interval Δt. The individual physical effects do not need to be split, which allows to generalize the physical models [12, 80]. Nevertheless, the simulation of fast dynamics requires a high discretization rate and many matrix exponentials need to be calculated. This becomes computationally demanding even though multiple efficient techniques to determine matrix exponentials exist [81, 82]. The basic concept behind matrix exponential-based simulation is visualized in Figure 2.25.

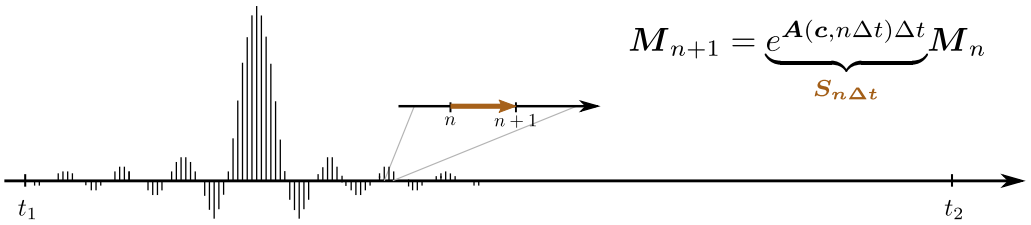

Figure 2.25: Visualization of the concept of simulations based on matrix exponentials. The dynamics of the Bloch equations are approximated to be piece-wise constant during small time intervals Δt ranging from step n to $n+1$. The system matrix $\boldsymbol{A}$ becomes constant and the originally time-ordered exponential becomes a matrix exponential. This can be solved to find a matrix $\boldsymbol{S}_{n\Delta t}$ that transforms the magnetization from $\boldsymbol{M}_n$ to $\boldsymbol{M}_{n+1}$.

2.3.3. ODE Solver

They previously introduced simulation methods require a constant sampling in time to hold the assumption of the piece-wise constant $\boldsymbol{A}$. Combined with the fact that these techniques provide up to second order convergence in step size, they are slow to simulate with high accuracies. To overcome these limitations, it is exploited that the Bloch equations (2.46) are ODEs and generic solvers are applied to integrate them. In this section, ODE solvers are introduced and extended to provide an adaptive step size control.
For a better understanding of how they work, the Bloch equations (2.116) are reduced to their gradient f_i form,

$$\frac{\mathrm{d}}{\mathrm{dt}}M_i(\boldsymbol{c},t) = f_i(\boldsymbol{M}(\boldsymbol{c},t),\boldsymbol{c},t)\ , \tag{2.139}$$

with the individual axis components $i \in (x,y,z)$.
ODE solvers estimate the unknown magnetization $\boldsymbol{M}_{n+1}(t_{n+1})$ at time $t_{n+1} = t_n + h$ with

step size h from the known previous time point $\boldsymbol{M}_n(t_n)$. The individual techniques differ in the number of intermediate gradients within h that are summed up and averaged.

Euler Method The Euler method [83, p.720] is the simplest ODE solver. It exploits only information from the beginning of the interval at t_n and interpolates a solution for t_{n+1}. The update follows with the product of step size h and gradient $f(t_n,\boldsymbol{M}_n)$ in t_n referred to as k_1:

$$k_1 = h \cdot f(t_n,\boldsymbol{M}_n) \tag{2.140}$$

$$\boldsymbol{M}_{n+1} = \boldsymbol{M}_n + k_1 + O(h^2)\ . \tag{2.141}$$

It shows an approximation error in the order of h^2, here in Big O notation.

Midpoint Method Taking not just gradient information of the initial time t_n but adding an intermediate step to the interpolation leads to the midpoint method [83, p.720]. The gradient at t_n is added as k_1, similar to the Euler method, but the additional approximated gradient at $t_n + \frac{h}{2}$ that depends on k_1 is calculated to improve the accuracy of the solution:

$$k_1 = h \cdot f(t_n,\boldsymbol{M}_n) \tag{2.142}$$

$$k_2 = h \cdot f(t_n + \frac{h}{2}, \boldsymbol{M}_n + \frac{k_1}{2}) \tag{2.143}$$

$$\boldsymbol{M}_{n+1} = \boldsymbol{M}_n + k_2 + O(h^3)\ . \tag{2.144}$$

This additional gradient information decreases the error order to $O(h^3)$ with $h > 1$.

Generic Runge-Kutta Method This concept of adding information from more intermediate points can be generalized to the generic Runge-Kutta (RK) method. Here, information of $s-1$ intermediate points is combined to approximate the magnetization at $\boldsymbol{M}_{n+1}$ from its origin $\boldsymbol{M}_n$:

$$k_i = h_n \cdot f\left(t_n + a_i h_n, \boldsymbol{M}_n + \sum_{j=1}^{s} b_{ij} k_j\right), \quad \text{with} \quad i = 2,\ldots,s \tag{2.145}$$

$$\boldsymbol{M}_{n+1} = \boldsymbol{M}_n + \sum_{i=1}^{s} c_i k_i\ . \tag{2.146}$$

The coefficients a_i, b_{ij} and c_i define the weighting of the integration coefficients and are commonly presented in a full butcher array

$$\begin{array}{c|c} \boldsymbol{a} & \boldsymbol{b} \\ \hline & \boldsymbol{c}^T \end{array} = \begin{array}{c|cccc} a_1 & b_{11} & b_{12} & \dots & b_{1s} \\ a_2 & b_{21} & b_{22} & \dots & b_{2s} \\ \vdots & \vdots & \vdots & \ddots & \vdots \\ a_s & b_{s1} & b_{s2} & \dots & b_{ss} \\ \hline & c_1 & c_2 & \dots & c_s \end{array} . \tag{2.147}$$

Variable Step Size Runge-Kutta Method Up to now, techniques that provide an increased order of convergence compared to the rotation simulation techniques are discussed. Next, the previously required constant sampling in time is addressed. Following the definition of a generalized formulation of RK methods, the extention to adaptive step size control is introduced. This extension avoids manual tuning of the step size and reduces the computational complexity when temporal dynamics like RF pulses and relaxation effect are simulated. Mainly two different approaches for adding adaptive step size control to an ODE solver have been developed: Techniques that are based on the Richardson extrapolation involve two calculations of $\boldsymbol{M}_{n+1}$ with different step sizes and adapt h with knowledge about the errors. This procedure, also known as step-doubling [83, p.716], is computationally demanding and two times less efficient than an embedded formula technique, which is discussed in the following.

A prominent example of embedded RK algorithms is the Dormand-Prince (DOPRI) method [84]. It is based on a classical RK 5 algorithm [83, p.716]:

$$\begin{aligned} k_1 &= h \cdot f(t_n, \boldsymbol{M}_n) \\ k_2 &= h \cdot f(t_n + a_2 h, \boldsymbol{M}_n + b_{21} k_1) \\ &\dots \\ k_6 &= h \cdot f(t_n + a_6 h, \boldsymbol{M}_n + b_{61} k_1 + \dots + b_{65} k_5) \\ \boldsymbol{M}_{n+1} &= \boldsymbol{M}_n + c_1 k_1 + c_2 k_2 + c_3 k_3 + c_4 k_4 + c_5 k_5 + c_6 k_6 + O(h^6), \end{aligned} \tag{2.148}$$

and includes an embedded RK 4:

$$\boldsymbol{M}^*_{n+1} = \boldsymbol{M}_n + \sum_{i=1}^{s=6} c^*_i k_i + O(h^5). \tag{2.149}$$

Note the different coefficients c^*_i for the RK 4. The coefficients are [84]:

$$
\begin{array}{c|c}
\boldsymbol{a} & \boldsymbol{b} \\
\hline
 & \boldsymbol{c}^T \\
 & (\boldsymbol{c}^*)^T
\end{array}
=
\begin{array}{c|ccccccc}
0 & & & & & & & \\
\frac{1}{5} & \frac{1}{5} & & & & & & \\
\frac{3}{10} & \frac{3}{40} & \frac{9}{40} & & & & & \\
\frac{4}{5} & \frac{44}{45} & -\frac{56}{15} & \frac{32}{9} & & & & \\
\frac{8}{9} & \frac{19372}{6561} & -\frac{25360}{2187} & \frac{64448}{6561} & -\frac{212}{729} & & & \\
1 & \frac{9017}{3168} & -\frac{355}{33} & \frac{46732}{5247} & \frac{49}{176} & -\frac{5103}{18656} & & \\
1 & \frac{35}{384} & 0 & \frac{500}{1113} & \frac{125}{192} & -\frac{2187}{6784} & \frac{11}{84} & \\
\hline
 & \frac{35}{384} & 0 & \frac{500}{1113} & \frac{125}{192} & -\frac{2187}{6784} & \frac{11}{84} & \\
 & \frac{5179}{57600} & 0 & \frac{7571}{16695} & \frac{393}{640} & -\frac{92097}{339200} & \frac{187}{2100} & \frac{1}{40}
\end{array}
\quad . \tag{2.150}
$$

The error between the RK 5 and RK 4 for step n is calculated with

$$
\mathrm{err}_n = \boldsymbol{M}_{n+1} - \boldsymbol{M}^*_{n+1} \tag{2.151}
$$

and used to update the step size

$$
h_n = h_{n-1}\theta \left(\frac{\delta}{\mathrm{err}_n} \right)^{\frac{1}{5}} , \tag{2.152}
$$

which is based on the tolerance δ, the step size of the previous step h_{n-1} and an additional factor θ that improves convergence.

2.3.4. State-Transition Matrices

The previous section extended the simulation from homogeneously sampled rotation techniques to RK solvers incorporating an adaptive step size and higher convergence. While both improvements reduce the computational efforts markedly, an additional trick can reduce them even further. Following the idea of the matrix exponentials in Section 2.3.2, their concept is a special case of the generic time-ordered exponential. These generic solutions can be found with ODE solvers avoiding the assumption of fine homogeneous sampling in time domain. The resulting state-transition matrices $\boldsymbol{S}_{t_1 \to t_2}$ transform the magnetization $\boldsymbol{M}$ from time t_1 to t_2,

$$
\boldsymbol{M}(\boldsymbol{c},t_2) = \mathcal{T} \left\{ e^{\int_{t_1}^{t_2} \boldsymbol{A}(\boldsymbol{c},t)\mathrm{d}t} \right\} \boldsymbol{M}(\boldsymbol{c},t_1) = \boldsymbol{S}_{t_1 \to t_2} \boldsymbol{M}(\boldsymbol{c},t_1) , \tag{2.153}
$$

incorporating the time-varying system matrix $\boldsymbol{A}(\boldsymbol{c},t)$. They are a solution to the time-ordered exponential $e^{\int_{t_1}^{t_2} \boldsymbol{A}(\boldsymbol{c},t)\mathrm{d}t}$.

A detailed explanation of the novel simulation technique based on state-transition matrices

is presented in Section 4.2.2. A visualization of the concept is added to Figure 2.26.

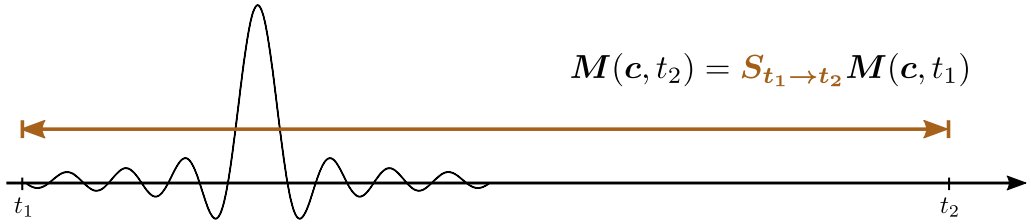

Figure 2.26: Visualization of the concept of simulations based on state-transition matrices. A state-transition matrix $\boldsymbol{S}_{t_1 \to t_2}$ is calculated from the generic time-ordered exponential solution of the Bloch equations transforming the magnetization from t_1 to t_2.

2.4. Partial Derivative Estimation

Exploiting complex signal models based on simulations has great advantages for QMRI because it allows the estimation of various physical properties for arbitrary sequences. One of the major challenges in QMRI is to design a reconstruction that allows to include such signal models. As presented in Section 2.2, many techniques are based on iterative algorithms. Most of them are gradient-based methods requiring knowledge about the partial derivatives of the signal with respect to the determined parameters. In QMRI, the temporary changing field $\boldsymbol{B}(t)$ in the Bloch equations (2.139) is typically known and $\boldsymbol{c}$ is determined. The required gradient information for parameter $\boldsymbol{c}_j$ and component M_i is

$$Z_{ij}(t) = \frac{\partial M_i(\boldsymbol{c},t)}{\partial c_j} \,. \tag{2.154}$$

Many techniques to find Z_{ij} exist but they vary depending on the complexity of the signal model.

2.4.1. Symbolic Differentiation

Starting with the application presented in Section 2.2, the easiest way to calculate partial derivatives is to derive an analytical expression g for the signal M_{xy} from the Bloch equations,

$$M_{xy} = g(\boldsymbol{c},t) \,, \tag{2.155}$$

and symbolically derive the partial derivatives with respect to the component $c_j \in \boldsymbol{c}$:

$$\frac{\partial M_{xy}}{\partial c_j} = \frac{\partial g(\boldsymbol{c},t)}{\partial c_j} \,. \tag{2.156}$$

An example is presented in Section 4.7.6 for an IR-bSSFP sequence.

2.4.2. Automatic Differentiation

If no single analytical representation of the whole M_{xy} is given, it might be possible to find piece-wise analytical functions and chain them similar to the rotation matrix simulations that are introduced in Section 2.3.1. With the knowledge of the piece-wise analytical partial derivatives, automatic differentiation can be exploited to calculate the overall derivatives. To demonstrate the basic concept, two intervals with piece-wise analytical signal representations g_1 for $t \in [0,1]$ and g_2 with $t \in [1,2]$ are assumed. The magnetization at $t = 2$ follows

$$\boldsymbol{M}(\boldsymbol{c},t=2) = g_2(g_1(\boldsymbol{M}(\boldsymbol{c},t=0),\boldsymbol{c},t)) = g_2(\boldsymbol{M}(\boldsymbol{c},t=1),\boldsymbol{c},t) \,. \tag{2.157}$$

With the i-th component of $\boldsymbol{M}$ and the j-th constant coefficient, the partial derivative can be calculated with the chain rule

$$\frac{\partial M_i}{\partial c_j} = \frac{\partial M_i}{\partial m_1}\frac{\partial m_1}{\partial c_j} = \frac{\partial g_2(m_1,\boldsymbol{c},t)}{\partial m_1}\frac{\partial g_1(m_0,\boldsymbol{c},t)}{\partial c_j} \,, \tag{2.158}$$

and $m_\tau = \boldsymbol{M}(\boldsymbol{c},t=\tau)$.
Two different types of automatic differentiation exist: The forward mode evaluates the chain rule from the inside out

$$\frac{\partial m_\tau}{\partial c_j} = \frac{\partial m_\tau}{\partial m_{\tau-1}}\frac{\partial m_{\tau-1}}{\partial c_j} \,, \tag{2.159}$$

with $m_2 = M_i$. The backwards mode runs in the opposite direction,

$$\frac{\partial M_i}{\partial m_\tau} = \frac{\partial M_i}{\partial m_{\tau+1}}\frac{\partial m_{\tau+1}}{\partial m_\tau} \,, \tag{2.160}$$

with $m_0 = c_j$. Both techniques have been used in various MRI applications but are dominantly present in machine learning based techniques.

2.4.3. Difference Quotients

If sequences have no analytical or piece-wise analytical signal representation, partial derivatives can be estimated with a generic difference quotient:

$$\frac{\partial M_i(\boldsymbol{c},t)}{\partial c_j} = \lim_{h\to 0} \frac{M_i(\boldsymbol{c},t)\Big|_{c_j+h} - M_i(\boldsymbol{c},t)\Big|_{c_j}}{h} \,. \tag{2.161}$$

It is calculated from two evaluations of the signal model $M_i(\boldsymbol{c},t)\Big|_{c_j}$ and $M_i(\boldsymbol{c},t)\Big|_{c_j+h}$ with small perturbation h in the desired parameter c_j. In practice, h needs to be tuned for each parameter c_j individually to ensure an accurate approximation of the derivative without amplification of numerical noise.
A visualization of the difference quotient technique is given in Figure 2.27.

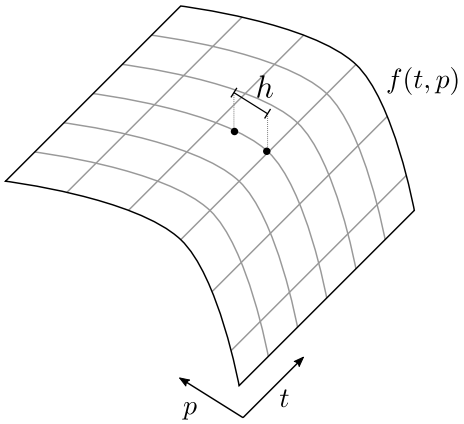

$$\frac{\partial}{\partial p} f(t,p) = \lim_{h\to 0} \frac{f(t,p+h)-f(t,p)}{h}$$

Figure 2.27: Visualization of a difference quotient for a generic function f depending on the parameters t and p. The partial derivative of f with respect to p can be approximated in the limit of a vanishing perturbation h from the difference between two evaluations of f with and without perturbated parameter p.

2.4.4. Direct Sensitivity Analysis

The direct sensitivity analysis [85] provides partial derivatives for generic non-analytical signals. It exploits an ODE-based temporal description of the signal and assumes that the partial derivative with respect to the parameter c_j exchanges with the total time derivative. A detailed explanation of the direct sensitivity analysis and its application to the Bloch equation is given in Section 4.2.1.

3. Methods

After introducing the fundamental basics of classical and quantitative magnetic resonance imaging (MRI), Bloch simulations and partial derivative estimation, this chapter is focused on the hardware and software of the performed experiments of Chapter 4 and 5. It does not provide a detailed explanation of the individual experiments performed in the analysis but rather discusses concepts and gives additional details compared to the Section 4.3.

3.1. Hardware

The methodological section starts with details about the used hardware components. The measurement devices, the physical reference objects and details about the computational resources are given.

3.1.1. Scanner System

In the fundamentals, the classical description of MRI is introduced in Section 2.1.1. It provides details about the Zeemann splitting for spin 1/2 particles and therefore about the origin of the macroscopic magnetization used for imaging. Without any measurement device, every object on earth already experiences a magnetic field. In Göttingen, the field strength is 49 μT [86, p.66]. This already leads to a Zeeman splitting and a resulting macroscopic magnetization. Following Equation (2.5) and (2.6), this low field strength leads to similar populations on both energy levels, $E_\downarrow$ and $E_\uparrow$. Therefore, exploiting only earth's magnetic field for MRI imaging leads to a small macroscopic magnetization and a low signal-to-noise ratio (SNR). To create a stronger signal, the magnetic field is increased with an experimental device: the MRI scanner presented in Figure 3.1.

In this work, two whole body systems have been used: a Siemens MAGNETOM Skyra and MAGNETOM Vida scanner (Siemens Healthineers AG, München, Germany). They increase the population difference between the spins' ground and excited state by providing a 3 T strong main magnetic field $\boldsymbol{B}_0$. It is created with superconductive electromagnets that are cooled with liquid helium. From Equation (2.8), the resonance frequency of the

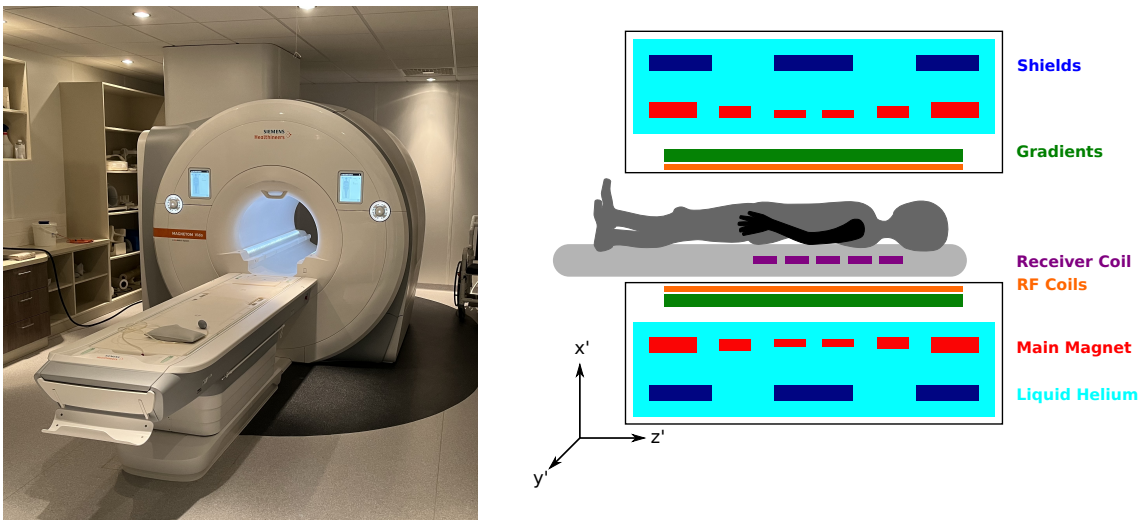

Figure 3.1: Image of the MAGNETOM Vida MRI scanner on the left. Visualization of the major components in a conventional scanner system on the right. Figure partially adapted from [13].

spin system can be derived for $\boldsymbol{B}_0$. This Larmor frequency is 127.74 MHz for H^1. For spatial encoding, which is explained in Section 2.1.7, both scanners incorporate strong gradients. The Skyra system has a Siemens XQ gradient system with a maximum strength of 45 mT/m at a slew rate of 200 T/m/s, whereas the Vida system has Siemens XT gradients with 60 mT/m and 200 T/M/s, respectively. Both can exploit a high number of independent receiver channels for parallel imaging (PI) (Section 2.1.7), but in this work only 20 channel head coils have been used to reduce the amount of acquired data. The excitation of the measured objects, which is introduced in Section 2.1.3, is achieved with radio frequency (RF) coils that are placed around the measured object. To improve the homogeneity of the main magnetic field, both scanners have been passively shimmed during setup and have been equipped with three first-order and five second-order shim coils (Section 5.4).

3.1.2. Reference Objects

Physical reference objects, also referred to as physical phantoms, are important for the development of new acquisition and reconstruction techniques. They are typically used after validations of methods with numerical phantoms, which are discussed in Section 3.2.1. Similarly to their numerical versions, physical phantoms allow for a controlled increase in complexity of the setup. In in vivo experiments, this is not possible due to hardware imperfections, motion and various interacting compartments in tissue. Thus, physical phantoms are important for verification and validation of reconstruction techniques,

especially for quantitative measurements like in quantitative magnetic resonance imaging (QMRI). In this study, mainly two physical reference objects have been used and those are introduced in the following.

NIST Phantom

The first physical phantom that was used is the NIST reference phantom [87], more precisely the system standard model 130. It is designed with five layers, each specialized for specific QMRI applications. A schematic visualization of it is given in Figure 3.2.

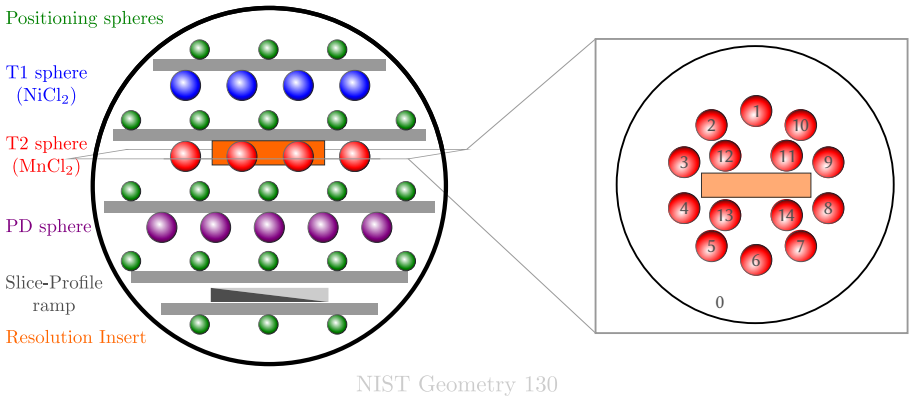

Figure 3.2: Visualization of the geometry of the NIST reference phantom (model 130) with focus on the T_2 sphere.

Due to the focus of this thesis on relaxation parameters, the T_2 sphere containing a $MnCl_2$ array of varying T_1 and T_2 relaxation times has been measured. The reference relaxation parameters are determined in a single slice with two gold-standard single-echo spin-echo measurements. Both techniques are discussed in more detail in Section 2.2.1 and their acquisition parameters are added to Table 4.1. The calculated reference values for the NIST phantom's T_2 sphere for a field strength of 3 T are listed in Table 3.1 [87].

Table 3.1: NIST phantom reference results of the T_2 sphere components [87]. The 0-th component defines the background. The numbers correspond to the labelled spheres in Figure 3.2.

Sphere No.	0	1	2	3	4	5	6	7
T_1 [s]	3	2.48	2.173	1.907	1.604	1.332	1.044	0.802
T_2 [s]	1	0.581	0.404	0.278	0.191	0.133	0.097	0.064

Sphere No.	8	9	10	11	12	13	14
T_1 [s]	0.609	0.458	0.337	0.244	0.177	0.127	0.091
T_2 [s]	0.046	0.032	0.023	0.016	0.011	0.008	0.006

SONAR Phantom

The second physical reference object is the SONAR phantom which consists of tubes with different gels of the Eurospin II line produced by Diagnostic Sonar LTD (Scotland, UK). The phantom includes the gels numbered 3, 4, 7, 10, 14 and 16. Their relaxation parameters have been measured in previous publications [9, 88]. T_1 is described by Wang in 2018 [9] and T_2 by Sumpf in 2014 [88]. Follow-up scans showed a good robustness of the gels against aging, so it can be assumed that the relaxation values from the publications mentioned above are still valid (see Table 3.2).

Table 3.2: SONAR phantom reference values taken from T_1 [9] and T_2 [88]. The 0th component defines the background and the 7th component a tube containing the same substance as the 0th.

Tube No.	0	1	2	3	4	5	6	7
T_1 [s]	3	0.311	0.458	0.633	0.805	1.116	1.441	3
T_2 [s]	1	0.046	0.081	0.101	0.132	0.138	0.166	1

3.1.3. Computational Resources

After discussing the measurement system and physical reference objects the computational resources of this work are described in detail in this section. The simulations, reconstructions and analysis of this thesis have been performed mainly on two server systems: The first server system is a Supermicro Super-Server (Supermicro Inc., San Jose, USA) with two Intel Xeon Gold 6132 14-Core CPU clocked at a base frequency of 2.60GHz with up to 3.7 GHz, and four Tesla V100-SXM2-32GB GPUs as well as 378 GB of RAM. The second server is also from Supermicro Super-Server (Supermicro Inc., San Jose, USA) but includes two AMD EPYC 7662 64-Core CPUs clocked at 2.0 GHz, 1 TB of RAM, and four Nvidia A100-SXM-80GB GPUs. Both systems run latest Debian linux distributions.

3.2. Software

Besides the always active main magnetic field, programs define how multiple gradients in all spatial directions are executed and when and how time-varying RF fields are switched on. They define pipelines to receive the data, demodulate it and reconstruct it in the end. Therefore, this project was mostly about designing own software, controlling the scanner, building reconstructions and simulations. In this section, an overview of the design of realistic numerical phantoms and reconstruction tools is provided.

3.2.1. Realistic Numerical Phantoms

The goal of this thesis is to develop a new generalized model-based reconstruction technique for multi-parameter mapping. In the long term, it should provide a new tool to determine physical quantities in patients, which can improve the diagnostic and potential treatments. While the final steps involve actual measurements on volunteers and physical reference objects, the initial tests were performed on numerical phantoms. Compared to their physical conter part, they allow for an even more gradual and controlled increase in complexity, which simplifies the debugging and testing of algorithms. Additionally, they do not require potentially expensive measurements and allow a careful preparation. A realistic numerical representation of a phantom needs to satisfy three major conditions:

1. Simulation of multi-coil receiver channels with realistic spatial sensitivities
2. Simulation of objects in image and frequency domain to include effects through finite sampling, as introduced in Section 2.1.9
3. Simulation of realistic temporal evolutions of the magnetization during an acquisition, as introduced in Section 2.3.

In the following, it is discussed why the created numerical phantom satisfies all of them.

Modelling Coil Sensitivities

Following the Biot-Savart law, the spatial sensitivity of receiver channels in MRI is generally smooth. Mathematically, smoothness can be modelled with various techniques, like the Sobolev norm [36], polynomials [56, 89] or sinusoid functions [90]. While polynomials work well, their accuracy increases less with more parameters compared to sinusoid models [90]. Therefore, this work focuses on a sinusoid sensitivity model.

The coil-sensitivity $S(\boldsymbol{r})$ at spatial location $\boldsymbol{r}$ is defined as a linear combination of sinusoids in their exponential form [90],

$$S(\boldsymbol{r}) = \sum_{\boldsymbol{v}} \boldsymbol{s}_{\boldsymbol{v}} e^{i\boldsymbol{r}\cdot\boldsymbol{v}} \,, \tag{3.1}$$

weighted with angular frequencies $\boldsymbol{s}_{\boldsymbol{v}}$ at position $\boldsymbol{v} = (v_x\ v_y)^T$ on a frequency grid. The distance between the frequency samples in $\boldsymbol{v}$ is set to $\Delta v_x = \frac{1}{2\cdot \mathrm{FoV}_x}$ and $\Delta v_y = \frac{1}{2\cdot \mathrm{FoV}_y}$. The frequencies $\boldsymbol{s}_{\boldsymbol{v}}$ are precalculated from a reference sensitivity scan with an 8-channel coil and are stored in a look-up table accessible for the simulation. Guerquin-Kern *et al.*

propose to limit the involved angular frequencies to a factor L [90]. In this implementation, L is set to 5.

Simulation in Frequency Space

After discussing how coil-sensitivities can be modelled mathematically, the focus is on the measured object in this section. Their geometry is constraint to elliptical regions $\mathcal{E}$ because of their analytical frequency space representation. This concept can be generalized to b-splines [90]. The individual regions are defined by their center $\boldsymbol{r}_c$ and angle of rotation θ between its two axis A and B. To find the frequency representation of $\mathcal{E}$, the operators $\boldsymbol{D} = \mathrm{diag}(A,B)$ and the rotation $\boldsymbol{R}_\theta$ around θ are required to transform $\mathcal{E}$ to a unit disc $\boldsymbol{u}$ [90],

$$\boldsymbol{u} = \boldsymbol{D}^{-1}\boldsymbol{R}^T(\boldsymbol{r} - \boldsymbol{r}_c)\,, \tag{3.2}$$

with a Fourier transform defined with the jinc-function

$$G(\boldsymbol{\omega}) = \frac{J_1(\boldsymbol{\omega})}{\boldsymbol{\omega}}\,, \tag{3.3}$$

based on a Bessel function of the first kind J_1. The Fourier transformation of the elliptical region $\mathcal{E}$ follows with [90, 91]

$$FT_{\mathcal{E}}(\omega) = 2\pi|\boldsymbol{D}|e^{-j\boldsymbol{\omega}\cdot\boldsymbol{r}_c}G\left(\boldsymbol{D}\boldsymbol{R}^T\boldsymbol{\omega}\right)\,, \tag{3.4}$$

and the absolute value operation $|\cdot|$.

By convolving the frequency representation of the elliptical region in Equation (3.4) with the angular frequencies from Equation (3.1), an analytical model for ellipses can be derived that is acquired with smooth spatial sensitivities in frequency space [90]:

$$FT_{\mathcal{E},\mathrm{sens}}(\omega) = 2\pi|\boldsymbol{D}|e^{-j\boldsymbol{\omega}\cdot\boldsymbol{r}_c}\sum_{\boldsymbol{v}}\boldsymbol{s}_{\boldsymbol{v}}e^{i\boldsymbol{r}\cdot\boldsymbol{v}}G\left(\boldsymbol{D}\boldsymbol{R}_{-\theta}(\boldsymbol{\omega}+\boldsymbol{v})\right)\,. \tag{3.5}$$

An object simulated analytically in frequency space can be sampled at arbitrary discrete points. Therefore, such phantoms enable testing of non-Cartesian sampling. In addition, they show the same errors through discrete and limited sampling like real measurements (Section 2.1.9). The resulting Gibbs ringing can be observed in the two inverse Fourier transformed geometries, as shown in Figure 3.4.

Combined Numerical Phantom

After discussing the design of an elliptical region $\mathcal{E}$ with its Fourier representation including spatial sensitivities in Equation (3.5), it is now discussed how multiple of these regions can be combined to form complex geometrical objects. They consist of different geometric components $\boldsymbol{G} \in \mathbb{C}^{M \times N}$ defined by $M \times N$ complex samples. An example of a numerical phantom that consists of four components, $C = 4$, is illustrated in Figure 3.3.

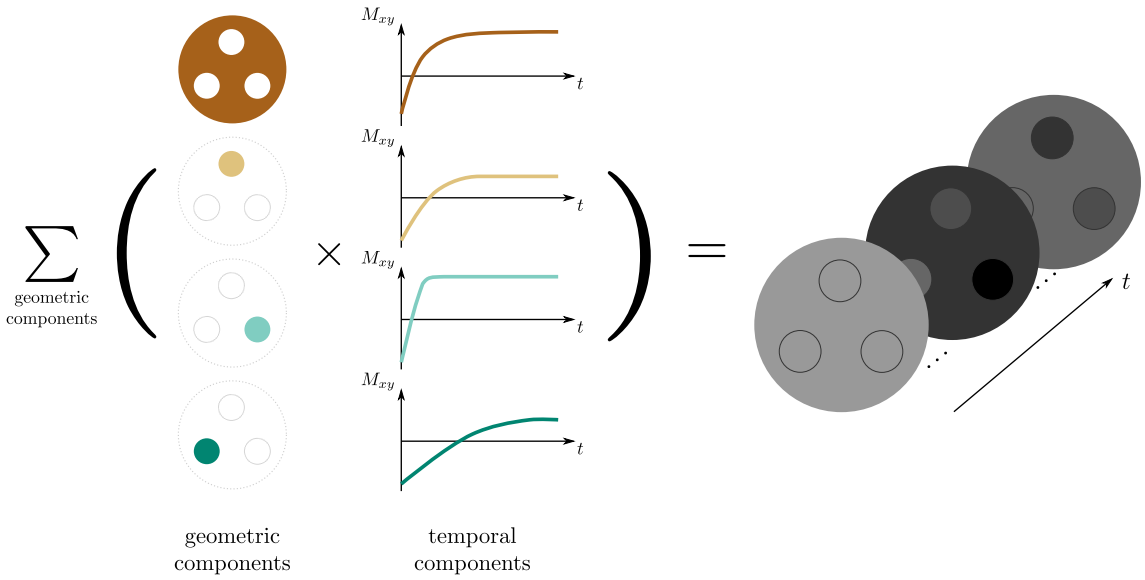

Figure 3.3: Visualization of the concept of the numerical phantom. A reference geometry is created from elliptical regions to provide individual tubes and a background. The components are element-wisely multiplied with simulated signal evolutions. The simulated phantom is the sum over all components.

It is defined by one background and three single elliptical, here circular, inner tube components. The geometric component of the background is designed as the sum of multiple ellipses with the same absolute intensity but opposite signs. This creates holes in the background component and avoids overlapping regions, which might lead to partial volume effects. Due to the linearity of the Fourier transform, the superposition of the individual tubes can be performed in the image and the frequency domain. By choosing the cutout ellipses in the background slightly larger than their component equivalents, signal-free black circles are created in the final phantom. They model plastic or glass tubes and are visualized on the right in Figure 3.3 and in Figure 3.4.
The component-wise design of the geometry allows for simple integration of temporary changing signals $\boldsymbol{S} \in \mathbb{C}^{C \times T}$, as presented in Section 2.3. Each geometric component is a signal evolution that is assigned by an element-wise multiplication in the pixel or the

frequency domain,

$$\boldsymbol{\mathcal{G}}_{\mathrm{sim},c} = \boldsymbol{\mathcal{G}}_c \odot \boldsymbol{S}_c \,, \tag{3.6}$$

leading to the simulated geometrical components $\boldsymbol{\mathcal{G}}_{\mathrm{sim}} \in \mathbb{C}^{M\times N\times C\times T}$. The element-wise multiplication includes the assumption of homogeneous characteristics for each component. Multiple different characteristics within a voxel, referred to as partial volume effect, can be created with overlapping spatial regions with different signal behavior. The final phantom $\mathbf{Pha} \in \mathbb{C}^{M\times N\times T}$ follows as sum over all spatial components:

$$\mathbf{Pha} = \sum_{c=1}^{C} \boldsymbol{\mathcal{G}}_{\mathrm{sim},c} \,. \tag{3.7}$$

The numerical phantom's geometries designed in this work follow their physical examples. The SONAR and T_2 sphere of the NIST phantom (model 130) have been implemented and are visualized in Figure 3.4. The relaxation values for their individual components are the same as listed in Table 3.1 and 3.2 if not stated otherwise.

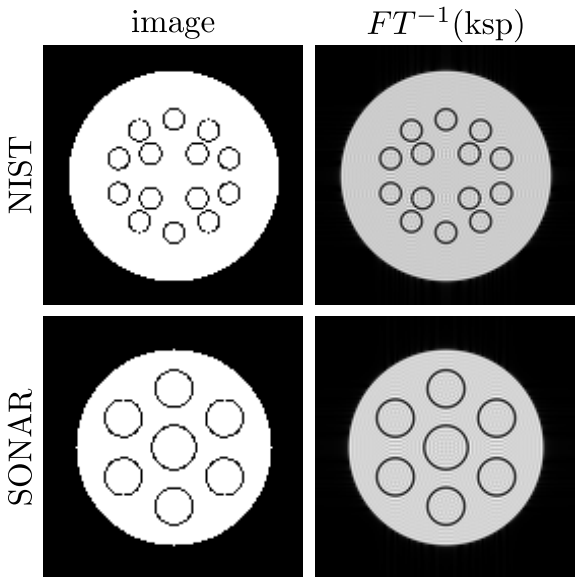

Figure 3.4: Visualization of the numerical phantom geometries for the T_2 sphere of the NIST (model 130) and the Diagnostic Sonar phantom. Both are presented as simulation in the image and the inverse Fourier transformed frequency domain.

3.2.2. Reconstruction and Simulation Software

All simulations and reconstructions of this work have been implemented and published in the Berkeley Advanced Reconstruction Toolbox (BART). Its command line interface (CLI) is convenient for prototyping and its C backend libraries provide a large variety of algorithms from simple matrix operators up to complex optimizations. This work exploits many of the implemented tools in BART, like a singular value decomposition (SVD) based coil-compression, a radial spoke intersections for gradient delay estimation (RING) based gradient delay estimation, parallel imaging and compressed sensing reconstructions, and a non-uniform fast Fourier transform (nuFFT). BARTs nonlinear operator framework [92] directly incorporates GPU support and advanced optimization algorithms, like the iteratively regularized Gauss-Newton method (IRGNM). The center of the Bloch model-based reconstruction tool is a simulation that is implemented with a Runge-Kutta (RK) solver, state-transition and rotation matrices. The nonlinear problem is solved with an IRGNM. Compared to the original regularized nonlinear inverse reconstruction (NLINV), introduced in Section 2.1.9, no conjugate gradient method (CG) but fast iterative shrinkage/thresholding algorithm (FISTA) is exploited to solve the linearized problem within each Gauss-Newton step which allows for enforcing a non-negativity constraint on the parameter maps. In the current implementation the whole linearized problem can be solved on GPUs. The simulation only runs on multiple CPUs which makes it the main contributor to the overall reconstruction time.

3.3. Reproducibility

After discussing some details about the implementation of the Bloch model-based reconstruction method, this section focuses on how the code and data can be accessed. It should give the reader the opportunity to reproduce all figures and more easily build up upon this work. The data for reproducing the results of this thesis has been uploaded to Zenodo:

1. Data @doi:10.5281/zenodo.7654462 for reproducing the figures in Section 4
2. Data @doi:10.5281/zenodo.7837312 for reproducing the figures in Section 5.

The figures can be reproduced with the scripts published on Github:

1. Scripts @mrirecon/bloch-moba for reproducing the figures in Section 4

2. Scripts @mrirecon/bloch-moba-misc for reproducing the figures in Section 5.

All reconstruction and simulation tools have been implemented and published in BART with commit `0c847a2`. Tutorials have been created to guide the reader interactively through the initial steps of applying the developed techniques:

1. Link→Simulation Tool Tutorial
2. Link→Bloch model-based Reconstruction Tutorial
3. Link→Abstract reproduction: Direct Sensitivity Analysis of the Bloch Equations.

4. Quantitative Magnetic Resonance Imaging by Nonlinear Inversion of the Bloch Equations

This chapter contains a reprint of the original article:

Original Article

N. Scholand, X. Wang, V. Roeloffs, S. Rosenzweig, and M. Uecker. Quantitative MRI by nonlinear inversion of the Bloch equations. *Magn. Reson. Med.* 2023; 90: 520-538. doi: 10.1002/mrm.29664

Contributions The numerical experiments and measurements in this work were performed by NS. The technique was implemented by NS, XW and MU. VR and SR provided conceptual guidance and help with the implementation. The majority of the manuscript and its revisions was written by NS. All authors contributed to the preparation of this manuscript.

Abstract

Purpose: Development of a generic model-based reconstruction framework for multi-parametric quantitative MRI that can be used with data from different pulse sequences.

Methods: Generic nonlinear model-based reconstruction for quantitative MRI estimates parametric maps directly from the acquired k-space by numerical optimization. This requires numerically accurate and efficient methods to solve the Bloch equations and their partial derivatives. In this work, we combine direct sensitivity analysis and pre-computed state-transition matrices into a generic framework for calibrationless model-based reconstruction that can be applied to different pulse sequences. As a proof-of-concept, the method is implemented and validated for quantitative T_1 and T_2 mapping with single-shot inversion-recovery (IR) FLASH and IR-bSSFP sequences in simulations, phantoms, and the human brain.

Results: The direct sensitivity analysis enables a highly accurate and numerically stable calculation of the derivatives. The state-transition matrices efficiently exploit repeating patterns in pulse sequences, speeding up the calculation by a factor of 10 for the examples considered in this work, while preserving the accuracy of native ODE solvers. The generic model-based method reproduces quantitative results of previous model-based reconstructions based on the known analytical solutions for radial IR-FLASH. For IR-bSSFP it produces accurate T_1 and T_2 maps for the NIST phantom in numerical simulations and experiments. Feasibility is also shown for human brain, although results are affected by magnetization transfer effects.

Conclusion: By developing efficient tools for numerical optimizations using the Bloch equations as forward model, this work enables generic model-based reconstruction for quantitative MRI.

Keywords: model-based reconstruction, sensitivity analysis, state-transition matrix, nonlinear inversion, Bloch equations, quantitative MRI

4.1. Introduction

Conventional quantitative magnetic resonance imaging is based on a two-step process, where first intermediate images are reconstructed and then physical models are fitted pixel-wisely to obtain parameter maps. Acquiring a sufficient amount of high quality images with carefully designed contrasts is required for achieving a good fit. For this reasons, these methods are too slow for many clinical applications. In contrast, nonlinear model-based reconstruction methods formulate image reconstruction as a single inverse problem. They exploit a physical model of the measurement process and directly estimate quantitative parameter maps from k-space. Thus, they make optimal use of the available data and enable highly efficient parameter mapping from signals acquired with sequences that make use of transient magnetization dynamics [5–8, 70]. These techniques have two problems: They are computationally demanding and they need to be specially designed for each application.

Alternatively, fingerprinting [11] uses a lookup dictionary obtained by Bloch simulations to map the pixels of intermediate images computed directly from undersampled data to quantitative parameter maps. This enables multi-parametric mapping with high acceleration in a flexible and computationally efficient framework, but is not optimal due to its lack of a least-squares data consistency term. Subspace models can be exploited for a more efficient mapping by approximating the physical signal with a larger linear subspace. They reduce the computational demand of the reconstruction very efficiently [65–69], but are still not optimal because a linear subspace is used to approximate the manifold of possible signals. For complicated spin dynamics a larger number of subspace coefficients may be needed to accurately represent the signal, rendering subspace methods less efficient [8].

The aim of this work is to develop a generic framework for nonlinear model-based reconstruction with accurate signal models for different MRI sequences even with complicated spin dynamics. The generalization of the forward model then allows the use of optimized sequences for which no analytical expression for their signal can be derived. Fundamentally, such a generic method requires efficient techniques to compute the partial derivatives of the Bloch equations. So far, two different methods were used in MRI. First, symbolic derivatives can be calculated for analytical solutions of the Bloch equations for special sequences [9, 10, 72] and this can be generalized to chains of small blocks using automatic differentiation [93, 94]. These methods require idealized assumptions such as hard pulse approximation and perfect inversion. In more complicated scenarios with long pulses or imperfect inversion they require high discretization rates or suffer from errors.

Second, derivatives can be estimates using difference quotients [73, 74]. This method fully exploits the generality of full Bloch simulations, but is computational expensive and requires careful tuning to balance accuracy and noise amplification.

To overcome these limitations, this work uses a direct sensitivity analysis [85] to compute the derivatives of the Bloch equations for arbitrary sequences with high accuracy by solving an extended system of ordinary differential equations (ODE). The technique is validated using an analytical model of an IR-bSSFP sequence and is compared to results obtained from difference quotients methods. To further improve computation speed, pre-computed state-transition matrices are applied to arbitrary initial conditions solving the required ODEs for all repeating parts of an MRI sequence efficiently. They are validated by comparing them to the direct application of a Runge-Kutta ODE solver. We further integrate both techniques in a nonlinear model-based reconstruction with integrated calibration-less parallel imaging. For IR-FLASH, we show that the methods reproduce the results of an analytical model. In a numerical and measured phantom study with an IR-bSSFP sequence we refine the flexible forward model of the generic model-based reconstruction to include realistic simulations with slice-selective excitations and hyperbolic secant inversion pulses. Thus, we show that the reconstruction quality benefits much from the more physically accurate modelling leading to accurate T_1 and T_2 parameter maps. Finally, we test the developed technique on in vivo brain data from a healthy volunteer.

Parts of this work have been published in [95–98].

4.2. Theory

In the following, we briefly explain the concepts of a direct sensitivity analysis and its application to the Bloch equations (SAB). We then describe how state-transition matrices (STMs) can be used to accelerate the solution of the ODEs. Afterwards, both methods are integrated into a nonlinear model-based reconstruction method.

4.2.1. Sensitivity Analysis of the Bloch Equations

We consider the temporal evolution of a magnetization vector $\boldsymbol{M}(\boldsymbol{c},t)$ depending on a vector of parameters $\boldsymbol{c}$ and time t. The temporal behavior of its components $M_i(\boldsymbol{c},t)$ is described by the Bloch equations as a system of ODEs

$$\frac{\mathrm{d}}{\mathrm{dt}} M_i(\boldsymbol{c},t) = f_i(\boldsymbol{M}(\boldsymbol{c},t),\boldsymbol{c},t)\,, \tag{4.1}$$

where f defines the dynamics. The partial derivative of the component M_i with respect to the parameter $\boldsymbol{c}_j$ defines the (i,j)-th entry

$$Z_{ij}(t) = \frac{\partial M_i(\boldsymbol{c},t)}{\partial c_j} \tag{4.2}$$

of the sensitivity matrix $\boldsymbol{Z}(t)$.

Using direct sensitivity analysis [85] one obtains $\boldsymbol{Z}(t)$ by solving an additional set of ODEs. Assuming that the partial and ordinary derivatives interchange, the time derivative of the (i,j)-th entry of $\boldsymbol{Z}$ is

$$\frac{\mathrm{d}}{\mathrm{d}t} Z_{ij}(t) = \frac{\mathrm{d}}{\mathrm{d}t}\left(\frac{\partial M_i(\boldsymbol{c},t)}{\partial c_j}\right) = \frac{\partial}{\partial c_j}\left(\frac{\mathrm{d}M_i(\boldsymbol{c},t)}{\mathrm{d}t}\right) . \tag{4.3}$$

Substituting $\frac{\mathrm{d}M_i(\boldsymbol{c},t)}{\mathrm{d}t}$ then yields

$$\frac{\mathrm{d}}{\mathrm{d}t} Z_{ij}(t) = \frac{\partial}{\partial \boldsymbol{c}_j} f_i(\boldsymbol{M}(\boldsymbol{c},t),\boldsymbol{c},t) . \tag{4.4}$$

With the chain rule, the resulting ODE becomes

$$\begin{aligned}\frac{\mathrm{d}}{\mathrm{d}t} Z_{ij}(t) &= \frac{\partial f_i(\boldsymbol{M}(\boldsymbol{c},t),\boldsymbol{c},t)}{\partial \boldsymbol{c}_j} + \sum_j \frac{\partial f_i(\boldsymbol{M}(\boldsymbol{c},t),\boldsymbol{c},t)}{\partial M_j} \frac{\partial M_j(\boldsymbol{c},t)}{\partial \boldsymbol{c}_j} \\ &= \frac{\partial f_i(\boldsymbol{M}(\boldsymbol{c},t),\boldsymbol{c},t)}{\partial \boldsymbol{c}_j} + \sum_j \frac{\partial f_i(\boldsymbol{M}(\boldsymbol{c},t),\boldsymbol{c},t)}{\partial M_j} Z_{ij},\end{aligned} \tag{4.5}$$

where $\frac{\partial f_i(\boldsymbol{M}(\boldsymbol{c},t),\boldsymbol{c},t)}{\partial M_j}$ describes the (i,j)-th element of the Jacobian $J_{i,j}$. This can be written compactly for the sensitivity matrix $\boldsymbol{Z}(t)$ as

$$\frac{\mathrm{d}}{\mathrm{d}t} \boldsymbol{Z}(t) = \boldsymbol{f_c}(\boldsymbol{M}(\boldsymbol{c},t),\boldsymbol{c},t) + \boldsymbol{J}(\boldsymbol{M}(\boldsymbol{c},t),\boldsymbol{c},t) \cdot \boldsymbol{Z}(t) . \tag{4.6}$$

If a direct sensitivity analysis is applied to the Bloch equations for the parameters R_1, R_2 and B_1, the ODE in Equations 4.6 describing the temporal evolution of the sensitivities becomes

$$\tfrac{\mathrm{d}}{\mathrm{d}t}\boldsymbol{Z} = \begin{pmatrix} 0 & -M_x & -\gamma \sin\phi\, M_z \\ 0 & -M_y & \gamma \cos\phi\, M_z \\ M_0 - M_z & 0 & \gamma(\sin\phi\, M_x - \cos\phi\, M_y) \end{pmatrix} + \begin{pmatrix} -R_2 & \gamma B_z & -\gamma \sin\phi\, B_1 \\ -\gamma B_z & -R_2 & \gamma \cos\phi\, B_1 \\ \gamma \sin\phi B_1 & -\gamma \cos\phi\, B_1 & -R_1 \end{pmatrix} \cdot \boldsymbol{Z} . \tag{4.7}$$

depending on the x, y and z components of the magnetization $\boldsymbol{M}$, the magnetic fields B_z and B_1 as well as the RF pulse phase ϕ. Equation 4.7 is solved jointly with the Bloch Equations 4.1 which provide the time-dependent solutions for M_x, M_y, and M_z.

4.2.2. State-Transition Matrices

By embedding the magnetization vector into a four-dimensional space

$$\boldsymbol{M}(\boldsymbol{c},t) = \begin{pmatrix} M_x(\boldsymbol{c},t) \\ M_y(\boldsymbol{c},t) \\ M_z(\boldsymbol{c},t) \\ 1 \end{pmatrix}, \tag{4.8}$$

we obtain a formulation of the Bloch Equations 4.1 as a system of homogeneous ODEs

$$\frac{\mathrm{d}\boldsymbol{M}(\boldsymbol{c},t)}{\mathrm{d}t} = \boldsymbol{f}(\boldsymbol{M}(\boldsymbol{c},t),\boldsymbol{c},t) = \boldsymbol{A}(\boldsymbol{c},t)\ \boldsymbol{M}(\boldsymbol{c},t)\ , \tag{4.9}$$

with the system matrix

$$\boldsymbol{A}(\boldsymbol{c},t) = \begin{pmatrix} -R_2 & \gamma \boldsymbol{G}_z(t)\cdot\boldsymbol{r} & -\gamma B_y(t) & 0 \\ -\gamma \boldsymbol{G}_z(t)\cdot\boldsymbol{r} & -R_2 & \gamma B_x(t) & 0 \\ \gamma B_y(t) & -\gamma B_x(t) & -R_1 & M_0 R_1 \\ 0 & 0 & 0 & 0 \end{pmatrix}, \tag{4.10}$$

at location $\boldsymbol{r}$ depending on time t, the z-gradient $\boldsymbol{G}_z$ and the magnetic fields $B_{x,y}$.

The Bloch equations can be solved directly for time-dependent coefficients $\boldsymbol{A}(t)$ using standard ODE solvers. Here we describe the pre-computation of STMs as more efficient way to solve the equations for MRI sequences with repeating patterns. A STM $\boldsymbol{S}_{t_1\to t_2}$ describes the evolution of an arbitrary starting magnetization $\boldsymbol{M}(\boldsymbol{c},t_1)$ for the time span from t_1 to t_2 including all effects from relaxation and time-dependent external RF fields. This compresses the temporal evolution to a single matrix multiplication

$$\boldsymbol{M}(\boldsymbol{c},t_2) = \boldsymbol{S}_{t_1\to t_2}\boldsymbol{M}(\boldsymbol{c},t_1)\ . \tag{4.11}$$

The computation of $\boldsymbol{S}_{t_1\to t_2}$ is based on derivation of Equation 4.11

$$\frac{\mathrm{d}\boldsymbol{M}(\boldsymbol{c},t_2)}{\mathrm{d}t_2} = \frac{\mathrm{d}}{\mathrm{d}t_2}\left(\boldsymbol{S}_{t_1\to t_2}\boldsymbol{M}(\boldsymbol{c},t_1)\right)\ . \tag{4.12}$$

Using the Bloch Equations 4.9 to replace the time derivative on the left side and using $\frac{\mathrm{d}\boldsymbol{M}(t_1)}{\mathrm{d}t_2} = 0$ for the right, we obtain

$$\boldsymbol{A}(t_2)\boldsymbol{M}(\boldsymbol{c},t_2) = \left(\frac{\mathrm{d}}{\mathrm{d}t_2}\boldsymbol{S}_{t_1\to t_2}\right)\ \boldsymbol{M}(\boldsymbol{c},t_1)\ . \tag{4.13}$$

By using Equations 4.11 and switching both sides we obtain

$$\frac{\mathrm{d}}{\mathrm{d}t_2} \boldsymbol{S}_{t_1 \to t_2}\, \boldsymbol{M}(\boldsymbol{c}, t_1) = \boldsymbol{A}(t_2) \boldsymbol{S}_{t_1 \to t_2} \boldsymbol{M}(\boldsymbol{c}, t_1)\ . \tag{4.14}$$

As this holds for arbitrary $\boldsymbol{M}(\boldsymbol{c}, t_1)$ and by renaming t_2 as t a system of ODEs

$$\frac{\mathrm{d}}{\mathrm{d}t} \boldsymbol{S}_{t_1 \to t} = \boldsymbol{A}(t) \boldsymbol{S}_{t_1 \to t} \tag{4.15}$$

for the entries of the STM is derived. This ODEs 4.15 can be solved for estimating $\boldsymbol{S}_{t_1 \to t_2}$ column-wisely with an ODE solver [81, 82] with initial conditions

$$\boldsymbol{S}_{t_1 \to t_1} = \mathbb{1}\ . \tag{4.16}$$

The solution of the state-transition ODE in Equation 4.15 can be formally defined as a time ordered exponential

$$\boldsymbol{S}_{t_1 \to t_2} = \prod_{t_1}^{t_2} e^{\boldsymbol{A}(\tau)\mathrm{d}\tau} \equiv \mathcal{T} \left\{ e^{\int_{t_1}^{t_2} \boldsymbol{A}(\tau)\mathrm{d}\tau} \right\} \tag{4.17}$$

$$\equiv \lim_{N \to \infty} \left(e^{\boldsymbol{A}(t_N)\Delta t} e^{\boldsymbol{A}(t_{N-1})\Delta t} \dots e^{\boldsymbol{A}(t_1)\Delta t} e^{\boldsymbol{A}(t_0)\Delta t} \right)\ . \tag{4.18}$$

This links the proposed technique to approximation methods based on matrix-exponentials computed using discretized sampling [12, 80].

This technique is not limited to the Bloch Equations, but can be extended to also include the sensitivity analysis for the three partial derivatives R_1, R_2 and B_1. This is further described in Appendix 4.7.1.

4.2.3. Bloch Model-Based Reconstruction

In the following, we integrate the generic Bloch operator $\mathcal{B}$ into a nonlinear model-based reconstruction framework with non-Cartesian, calibrationsless, parallel imaging and compressed sensing as illustrated in Figure 4.1. The reconstruction method solves the nonlinear inverse problem for the maps $\boldsymbol{x} = (\boldsymbol{x_p}\ \boldsymbol{x_c})^T$ with the physical parameters $\boldsymbol{x_p} = (R_1\ R_2\ M_0\ B_1)^T$ and coil sensitivities $\boldsymbol{x_c} = (c_1\ \dots\ c_N)^T$ by optimizing

$$\hat{\boldsymbol{x}} = \underset{\boldsymbol{x}}{\operatorname{argmin}} \|\boldsymbol{y} - \mathcal{A}(\boldsymbol{x})\|_2^2 + \alpha \boldsymbol{Q}(\boldsymbol{x_c}) + \beta \boldsymbol{R}(\boldsymbol{x_p})\ . \tag{4.19}$$

Equation 4.19 includes the forward-operator $\mathcal{A}$, the measured data $\boldsymbol{y}$, the Sobolev norm $\boldsymbol{Q}$ with its regularization parameter α to enforce the smoothness of coil profiles [36] and B_1 maps. A joint sparsity constraint $\boldsymbol{R}$ is applied to the other parameter maps [99,

$$\hat{x} = \underset{\boldsymbol{x_c}, \boldsymbol{x_p}}{\operatorname{argmin}} (\|\boldsymbol{y} - \mathcal{PFC}(\boldsymbol{x_c}, \mathcal{B}(\boldsymbol{x_p}))\|_2^2 + \alpha \boldsymbol{\mathcal{Q}}(\boldsymbol{x_c}) + \beta \boldsymbol{\mathcal{R}}(\boldsymbol{x_p}))$$

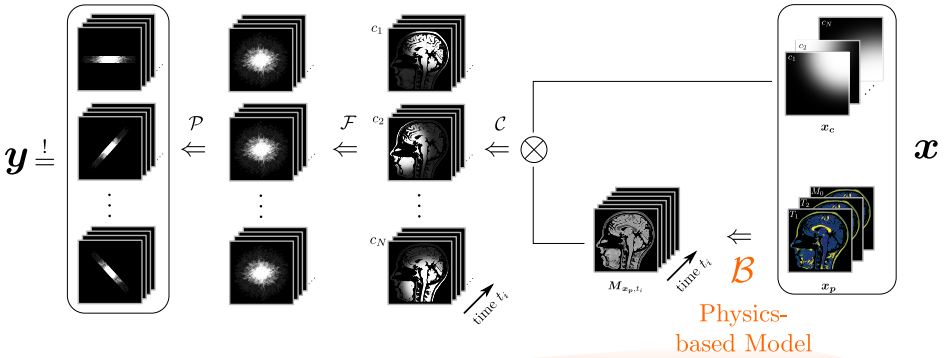

Bloch ODE

$$\frac{\mathrm{d}\boldsymbol{M}}{\mathrm{d}t} = \begin{pmatrix} -R_2 & \gamma B_z & -\gamma \sin\phi\ B_1 & 0 \\ -\gamma B_z & -R_2 & \gamma \cos\phi\ B_1 & 0 \\ \gamma \sin\phi B_1 & -\gamma \cos\phi B_1 & -R_1 & R_1 M_0 \\ 0 & 0 & 0 & 0 \end{pmatrix} \begin{pmatrix} M_x \\ M_y \\ M_z \\ 1 \end{pmatrix}$$

Sensitivity ODE

$$\frac{\mathrm{d}}{\mathrm{d}t}\boldsymbol{Z} = \begin{pmatrix} 0 & -M_x & -\gamma \sin\phi\ M_z \\ 0 & -M_y & \gamma \cos\phi\ M_z \\ M_0 - M_z & 0 & \gamma(\sin\phi\ M_x - \cos\phi\ M_y) \end{pmatrix} + \begin{pmatrix} -R_2 & \gamma B_z & -\gamma \sin\phi\ B_1 \\ -\gamma B_z & -R_2 & \gamma \cos\phi\ B_1 \\ \gamma \sin\phi B_1 & -\gamma \cos\phi\ B_1 & -R_1 \end{pmatrix} \cdot \boldsymbol{Z}$$

Figure 4.1: Illustration of the operators used in the Bloch model-based reconstruction. The bottom part presents the ODEs for the signal and the derivatives.

100]. The full forward operator is $\mathcal{A} = \mathcal{PFCB}$. It is solved by the Iteratively Regularized Gauss-Newton Method (IRGNM)

$$\begin{aligned} \hat{\boldsymbol{x}}_{n+1} = \underset{\boldsymbol{x}}{\operatorname{argmin}} \|D\mathcal{A}(\boldsymbol{x}_n)(\boldsymbol{x} - \boldsymbol{x}_n) + \mathcal{A}(\boldsymbol{x}_n) - \boldsymbol{y}\|_2^2 \\ + \alpha_n \boldsymbol{\mathcal{Q}}(\boldsymbol{x_c}) + \beta_n \boldsymbol{\mathcal{R}}(\boldsymbol{x_p}) \end{aligned} \tag{4.20}$$

with the Jacobian $D\mathcal{A}(\boldsymbol{x}_n)$ and the regularization parameters $\alpha_n = \alpha_0 \cdot q^n$ and $\beta_n = \beta_0 \cdot q^n$ at the nth iteration step. Here, C is the nonlinear parallel imaging operator combining the signal with the coil profiles, $\mathcal{F}$ represents the Fourier operator, $\mathcal{P}$ the sampling pattern. The generic operator $\mathcal{B}$ takes information about the applied sequence and outputs the simulated signal based on the STM technique. The partial derivatives of $\mathcal{B}$ are calculated using the direct sensitivity analysis. The derivatives of $\mathcal{A}$ are described in Appendix 4.7.2.

4.3. Methods

4.3.1. Implementation

All simulations and reconstructions are implemented in the Berkeley Advanced Reconstruction Toolbox (BART) using single-precision floating point arithmetic [101]. The Bloch operator $\mathcal{B}$ is implemented in BARTs nonlinear operator framework [92]. The calibrationless model-based reconstruction is based on an IRGNM-FISTA following Wang *et al.* [9] and we refer to this work for further details. The Bloch operator includes a pixel-wise calculation of the signal evolution using STMs (Section 4.2.2) and of the partial derivatives with SAB (Section 4.2.1). ODEs are solved using the a Runge-Kutta algorithm (RK54) with adaptive step-sizes. The error tolerances are chosen to be 10^{-7} for the simulation comparisons in Section 4.2.1 and 4.2.2 as well as 10^{-6} for further reduced computational costs in the Bloch model-based reconstructions. The Runge-Kutta solver exploits weights published by Dormand and Prince [84]. For balancing the relative scaling of the partial derivatives during the optimization of Equation 4.19 pre-conditioning following Wang *et al.* [9] is used. The initial wavelet regularization is set to α_0=β_0=1 and decreased by q=1/2 in each Newton iteration. The output of the Bloch model operator $\mathcal{B}$ is scaled according to Section 4.7.4. As a globalized Newton method, the IRGNM does not require fine tuning of initial values. Here, the maps are initialized with the constants $R_1 = 1\,\text{Hz}$, $R_2 = 1\,\text{Hz}$, $M_0 = 1$, $B_1 = 0$ and the coil profiles are initialized with zero.

For comparison, we also implemented the reparameterized Look-Locker model from equation 4.29 in the same model-based reconstruction framework following Wang *et al.* [9].

4.3.2. Validation of Bloch Simulation

The accuracy of the SAB technique is validated with an IR-bSSFP sequence for tissue with $T_1/T_2 = 1250/45$ ms. An analytical solution for the IR-bSSFP signal can be derived from the Bloch equations [3] assuming hard pulses, a perfect inversion and a perfect non-selective excitation. The symbolic partial derivatives with respect to the parameters R_1, R_2, M_0 and B_1 are calculated in Appendix 4.7.6 and are used as ground truth. For validation of the derivatives the ODE simulation parameters are chosen to be close to the assumptions of the analytical model. The ODE solution for the derivatives is also compared to the difference quotient techniques (DQ) calculated using two simulations $M_{t,p}$ and $M_{t,p+h}$ differing by a small perturbation h for all parameters $p \in (T_1, T_2, M_0, B_1)$ and time points t:

$$\frac{\partial \boldsymbol{M}_t}{\partial p} \approx \frac{M_{t,p+h} - M_{t,p}}{h} \tag{4.21}$$

The size of the perturbation is decreased until numerical noise dominates.

To validate the STM approach in the presence of RF pulses, gradients, and relaxation, a slice-selective excitation of a Hamming-windowed sinc-shaped inversion pulse with T_{RF} = 1 ms, BWTP=1, Δz =10 mm, G_z = 10 mT/m is simulated. Relaxation parameters are selected based on typical human white matter values at 3 T: T_1/T_2 =832/80 ms [102]. The STM simulation is computed with the Runga-Kutta solver and the magnetization just before the slice rewinder is compared to a direct simulation exploiting the same solver. For comparison a traditional Bloch simulation technique based on temporal discretization with rotation matrices (ROT) is performed using a discretization rate of 1 MHz. According to the analysis shown in Figure S3, a sampling rate of 1 MHz is required for ROT to accurately model complex spin dynamics that include slice-selective RF pulses.
The simulation speed is analyzed for a FLASH sequence with FA=8°, TR/TE=3.1/1.7 ms and T_{RF}=1 ms simulated for 101 isochromats homogeneously distributed along a slice of 0.02 m width and using a slice-selection gradient of 12 mT/m. The tissue parameters are set to relaxation times of white matter at 3 T. The simulations were executed on a single Intel(R) i7-8565U CPU core at 1.80 GHz.

4.3.3. Validation of Reconstruction

To validate the model-based reconstruction we further perform validations on numerical and experimental phantoms as well as in vivo data for both single-shot IR-FLASH and IR-bSSFP sequences with tiny golden-angle based radial sampling. The IR-bSSFP sequence includes a prior $\alpha/2$-TR/2 pulse to achieve a smooth signal evolution during the transient state [103, 104]. To be able to decouple the information of T_1 and T_2 for an IR-bSSFP sequence (see section 4.7.5) a B_1 map is acquired on the same slice using a vendor protocol based on rapid B_1 estimation with preconditioned RF pulses and Turbo-FLASH readout [62]. All sequence parameters are shown in Table 4.1.

Phantom data for an IR-FLASH sequence published by Wang et al. [105] was downloaded from Zenodo [106]. This data was measured on a 3 T Magnetom Skyra by Siemens Healthcare (Erlangen, Germany) with a 20 channel head-coil. The measured phantom is a commercial reference phantom (Diagnostic Sonar LTD, Scotland, UK, Eurospin II, gel 3, 4, 7, 10, 14, and 16) consisting of six tubes with known T_1 relaxation values surrounded by water. A digital phantom of the dataset is created with the same sequence and acquisition

characteristics as the downloaded measurement. The relaxation parameters were set to the estimated reference T_1 and T_2 values from previous studies [9, 88]. Additional phantom data for a radial single-shot IR-bSSFP sequence was acquired on the T_2 spheres of a National Institute of Standards and Technology (NIST) phantom [87] on the same scanner and the same 20 channel head-coil. For comparison gold-standard maps of T_1 and T_2 are estimated on the same slice of the NIST phantom using fully-sampled single-echo spin-echo sequences. All phantom measurements were performed at constant room temperature (~21°C). The estimated quantitative values from gold-standard scans were used to simulate a second digital phantom with the same geometry as the measured T2-spheres of the NIST geometry (model 130).

Radial single-shot IR-FLASH and IR-bSSFP data for a brain of a healthy volunteer was acquired with a 20 channel head-coil on a Siemens Skyra 3T system (Siemens Healthcare, Erlangen, Germany) after obtaining written informed consent. The IR-FLASH data was measured with a TR/TE of 4.1/2.58 ms, a flip angle of 6°, a band-width-time-product (BWTP) of 4 and a RF pulse duration of 1 ms. The field-of-view (FoV) was 220x220 mm^2 measured at 512 samples with two-fold oversampling. The single-shot IR-bSSFP data was acquired with two different pulse durations: 1 ms and 2.5 ms respectively. The repetition and echo times were set to 4.88/2.44 ms and 10.8/5.4 ms. A FoV of 200x200 mm^2, a flip angle of 45°, a BWTP of 4 and a base resolution of 256 was chosen and the same for both measurements.

The phantom and in vivo IR-FLASH datasets are reconstructed with both the Look-Locker model and the Bloch model-based technique. As the IR-FLASH sequence is insensitive to R_2, its estimation in the Bloch model-based reconstruction was turned off by setting the scaling in the pre-conditioner to zero. The initial free decay of 15.3 ms during the non-selective hyperbolic secant inversion pulse is corrected in both cases using the correction published by Deichmann et al. [107].

The flexibility of the Bloch model-based reconstruction with its ability to also model more complex sequences is demonstrated using single-shot IR-bSSFP. In the analysis of the measured dataset the B_1 map is used in the forward model for scaling the nominal flip angle for each pixel. Additionally, the B_1 estimation is turned off by setting the scaling to zero in the pre-conditioning.

The method is numerically validated using a digital phantom of the T_2 sphere of the NIST phantom (model version 130) implemented in BART. The multi-coil phantom is simulated in the frequency domain with the same sequence parameters as the measurement. The eight coils are compressed to four virtual coils using a singular-value decomposition (SVD). Complex Gaussian noise is added before coil compression to further avoid an

inverse crime. To ensure realistic physical conditions the simulated signal model includes a non-selective hyperbolic secant inversion pulse and slice-selective excitations using multiple isochromats distributed over equally spaced slice-selection gradient positions. While analytical solutions of the Bloch equations require the assumption of perfect inversions and ideal non-selective excitation, the generic simulation of the Bloch model-based reconstruction technique can simulate more realistic signal models. We show how step-wise improvements to the model allow more accurate modelling of actual measurements. This is demonstrated on the numerical and measured NIST phantom datasets by performing reconstructions with various different assumptions about the signal model. The first reconstruction uses a model close to the analytical formula by assuming a perfect inversion and a non-selective excitation. We then add a realistic slice-selective excitation simulated as mean signal of various homogeneously spaced isochromats along the slice-selection gradient. To also model the effect of non-optimal inversion efficiency, the final reconstruction includes an extended model with realistic non-selective hyperbolic secant inversion.

The radial single-shot IR-bSSFP in vivo data is reconstructed using the most realistic model. For comparison, the single-shot IR-FLASH measurement was acquired on the same slice and reconstructed with the Bloch model-based reconstruction assuming a realistic IR-FLASH signal model with non-selective hyperbolic secant inversion and gradient based slice-selective excitation model to estimate a T_1 map.

Details about the measurements can be found in Table 4.1.

4.4. Results

4.4.1. Validation of Bloch Simulation

Figure 4.2 shows the partial derivatives for an IR-bSSFP sequence with respect to R_1, R_2 and B_1 for the analytical reference, the SAB technique and difference quotient (DQ) techniques with different perturbations h on the left. On the right Figure 4.2 presents the differences of DQ and SAB to the analytical reference.
As expected, the error of DQ decreases for small perturbations until numerical noise starts to dominate for very small h.

The SAB technique demonstrates a high accuracy and precision of estimating partial derivatives without requiring tuning of the perturbation level.

Figure 4.3.A compares the simulation results of a Hamming-windowed sinc-shaped inversion pulse using the Runge-Kutta 54 method with Dormand-Prince weights (RK54)

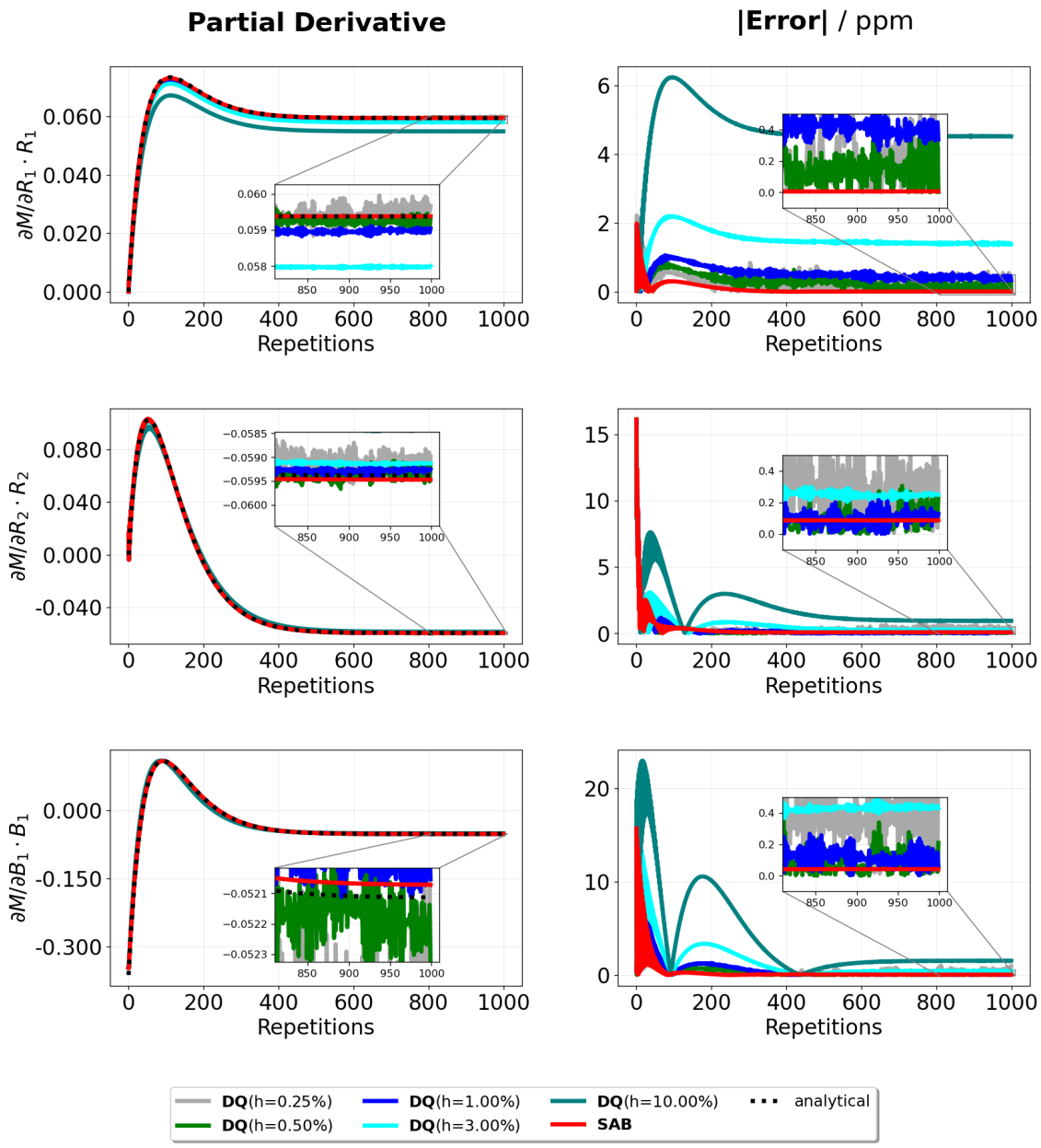

Figure 4.2: **Left**: Temporal evolution of the partial derivatives with respect to R_1, R_2 and B_1 estimated for an IR-bSSFP sequence with the SAB, DQ with varying perturbation levels h and the analytical references. **Right**: Plot with point-wise errors of the various DQ methods and the SAB with respect to the analytical reference. Note that the errors are presented in ppm for visualization.

[84], STM, and ROT technique.

The error of the STM simulation is dominated by numerical noise due to limited floating point precision. With the parameters used here, the STM technique has

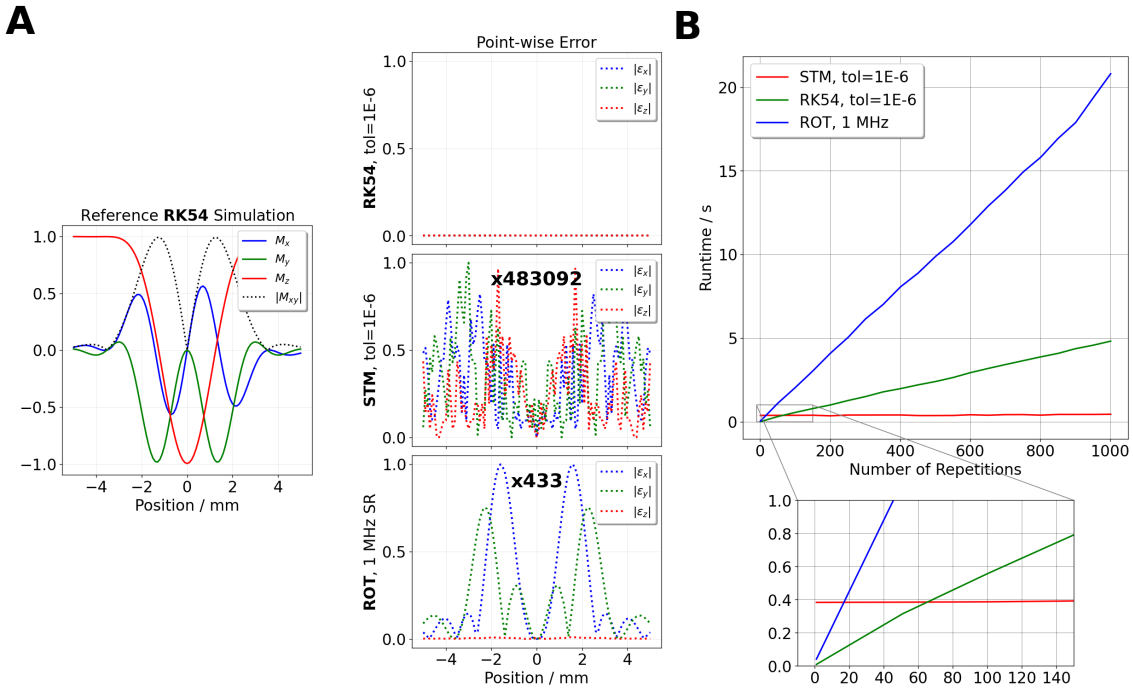

Figure 4.3: **A**: The slice-selection gradient based simulation for a Hamming-windowed sinc-shaped inversion pulse simulated with the RK54 framework is shown (left). The point-wise errors of the RK54 (top), the STM technique (center) and the ROT method (bottom) with sampling rate 1 MHz are plotted for the x-, y- and z- component of the magnetization. Note that the errors are scaled by large factors for visualization. **B**: The runtime of the STM technique is compared to the reference RK54 method and a ROT simulation performed with a sampling rate of 1 MHz. The simulation is performed for 101 isochromats homogeneously distributed along a slice-selection gradient during a FLASH sequence for various numbers of repetitions. The maximum of 1000 is chosen to cover about 4 s of acquisition, required to measure enough data points for mapping high T_1 values. A more detailed version of this figure has been added to the Supplementary Section S3.

substantially lower point-wise errors than ROT.

It demonstrates that STM reproduces the RK54 technique for finding solutions to the Bloch equations extremely well, while ROT is affected by errors due to the discretization with fixed sampling rate and its nature of being a first order method constrained to single floating point precision here. The runtime of RK54, STM and ROT is shown in Figure 4.3.B. The computational cost of ROT increases linear with higher sampling rates. The STM has higher initial costs than the other techniques which reflect the initial calculation of the state-transition matrices. The other methods are therefore faster for a small number

of repetitions. For more repetitions, the STM becomes much faster as it requires only a few matrix multiplications per TR. A detailed comparison of the computational cost and accuracy of the RK54, STM and ROT techniques for various error tolerances and sampling rates can be found in Supplementary Section S3 and Supplementary Figure S3.

4.4.2. Validation of Reconstruction

The Bloch model-based reconstruction was compared to the Look-Locker model-based version for simulated (Figure 4.4.A) and measured single-shot IR-FLASH phantom data (Figure 4.4.B). Both methods recover high quality T_1 maps with small differences. Values for the same Regions-of-Interests (ROIs) are very similar leading to their position on the diagonal of the Bloch vs. Look-Locker plot on the most right of Figure 4.4.A and Figure 4.4.B. The reconstructed tubes are very homogeneous in both reconstructions leading to low standard deviations. Reconstructions using different regularization parameters or no regularization are shown in Supplementary Figure S4 and Supplementary Figure S6, respectively.

In the difference map between the T_1 maps of the two methods only the water background shows areas with minor differences. This probably results from small differences in the Sobolev regularization on the flip angle map in both techniques. At the walls of the inner tubes there is not enough signal and the T_1 maps are not well defined. Results for the radial single-shot in vivo IR-FLASH data are shown in Figure 4.4.C. The parameter maps are visually indistinguishable except for minor artifacts in the areas of the head with flow related effects, which are not modelled by both signal models. The T_1 values in the marked ROIs for representative white and gray matter areas show a very good correspondence. The homogeneity within the white matter is high corresponding to a small standard deviation.

The complex M_0 parameter map in Figure 4.4.D reconstructed with the Bloch model-based reconstruction is of good quality showing no artifacts and a homogeneous phase. Only in border regions phase changes are present which are most likely caused by fat. The relative flip angle map is globally lower than one. It combines the effect of an imperfect slice-selective excitation and the present B_1 field. The intensity and phase of the estimated SVD-compressed virtual coil sensitivities is comparable to intensity and phase of sensitivities estimated with ESPIRiT [55](results not shown).

Figure 4.5 shows the reconstructed T_1 and T_2 maps of the digital NIST phantom (4.5.A) and the measurement (4.5.B) using the radial single-shot IR-bSSFP acquisition for different models compared to the reference values in Bland-Altman plots. The most simplistic model

assumes a perfect inversion and an ideal non-selective excitation (**Perfect Inversion**) and shows inaccuracies in the T_1 and T_2 estimation. By integrating a slice-selective excitation (**Slice**) the errors in T_2 are significantly reduced leaving an offset in T_1. Adding a realistic hyperbolic secant inversion pulse to the forward model (**Pulse+Slice**) corrects for the T_1 offset leading to an accurate estimation of the relaxation parameters. These effects are present in both: the simulation and the measured data reconstructions. Important to note is that the NIST phantoms contains some spheres with extreme T_1 and T_2 parameters [87], which were excluded from the Bland-Altman analysis in Figure 4.5.A and 4.5.B for improved visualization. In particular, the three highest T_2 values (1.450 s, 0.388 s and 0.271 s) were removed for the reconstruction from simulated data and the highest and lowest T_2 values (1.450 s, 0.006 s) for the measured data. Especially the simple model has difficulties in finding the correct relaxation parameters in the reconstruction of the measured data, so that the mean value is outside the plotted region. A direct comparison of reference and estimated parameters in a diagonal plot can be found in Supplementary Figure S1. A Bland-Altman plot with all data points is shown in Supplementary Figure S2.

Reconstructed T_1 and T_2 parameter maps for the two single-shot IR-bSSFP scans of a human brain are shown in Figure 4.6. For comparison, a map with the Look-Locker model-based reconstruction of the IR-FLASH scan of the same slice is added. Both IR-bSSFP reconstructions show large offsets in T_1 compared to the IR-FLASH reference. The relaxation values for the two analyzed ROIs are listed in Table 4.2. The differences are smaller for the longer TR and longer RF pulse duration T_{RF} compared to the short pulse protocol. This is likely due to the magnetization transfer effect (MT) that affects the IR-bSSFP sequence but is not included in the current study.

The reconstruction times depend on the complexity of the forward model. The reconstruction of the IR-FLASH datasets took about 80 s on a AMD EPYC 7662 64-Core CPU and a Nvidia A100-SXM-80GB GPU. The reconstruction of the simple forward model of the IR-bSSFP NIST phantom dataset took 60 s, while the most complex model reconstruction took 38 min. The longest reconstruction times were required for the in vivo IR-bSSFP dataset with short RF pulse. The strong slice-selection gradient prolonged the reconstruction to about 75 min.

4.5. Discussion

A nonlinear model-based reconstruction framework can be used in combination with well-crafted sequences and their analytical signal representations to accelerate quantitative

MRI. This work presents a generalization of this well-known approach to arbitrary MRI sequences by exploiting the Bloch equations directly as forward model. This method becomes computationally feasible by including a direct sensitivity analysis of the Bloch equations. It allows us to use a generic ODE solver to compute the derivatives required by efficient nonlinear optimization algorithms such as the IRGNM. In comparison to techniques based on difference quotients it produces highly stable and accurate partial derivatives without the need of fine-tuning perturbation levels. This was shown by estimating partial derivatives of an IR-bSSFP experiment with the mentioned techniques and by comparing their results to the underlying analytical reference.

To further reduce computational demand, we exploit pre-computed STMs. They are used to solve the Bloch equations and the system describing their sensitivities simultaneously for arbitrary initial conditions for a given time span. They reduce the spin dynamics even in the presence of external fields, gradients, and relaxation to single matrix multiplications. It dramatically speeds up the reconstruction whenever the MRI sequence contains repeated patterns as it is often the case. In the presented example of the FLASH sequence with 101 isochromats along a slice and simulated for 1000 repetitions, the run-time of the simulation was reduced by a factor of 10 from 5 s down to 0.5 s in comparison to a regular Runge-Kutta ODE solver. Even in the presence of gradients, RF pulses and relaxation the slice profile analysis showed the high accuracy of the STM technique in reproducing the ODE solver results.

Experimentally we confirmed that the Bloch model-based reconstruction reproduces the Look-Locker model as a special case. A comparison between both techniques showed only minor differences in the T_1 maps reconstructed from the single-shot phantoms and single-shot in vivo data.

The integration of a generic Bloch simulation into the reconstruction adds the flexibility to analyze a broad variety of sequences. As an initial example, we applied the technique to IR-bSSFP sequence and validated it using a numerical and measured NIST phantom dataset. By correctly modelling the slice-selective excitation and a non-selective hyperbolic secant inversion pulse highly accurate T_1 and T_2 maps could be obtained.

For a human brain, T_1 maps estimated from an IR-bSSFP sequence were compared to Bloch model-based reconstructions of an IR-FLASH acquisition of the same slice both including non-selective hyperbolic inversion and a slice-selective excitation. Here, differences could be observed which are likely caused by MT [45]. This hypothesis is supported by the fact that prolonging the RF pulse duration and increasing the TR reduced the differences, but preliminary results (Supplementary Section S5) suggest that this does not explain the complete discrepancy and that other effects may also play a role. The

NIST phantom measurement is not affected by MT effects, because it is based on water [87]. The IR-FLASH measurement is assumed to be unaffected by MT because of its small flip angle [108].

At this stage, the most relevant practical limitation is the need to manually tune the scaling factors used for pre-conditioning. For each analyzed sequence the relative scaling between the partial derivatives needs to be balanced manually to ensure smooth convergence. Future work is going to investigate automatic scaling techniques [109, 110].

Further extensions could be the application to hybrid state free precession sequences [12, 111], multi-echo inversion-recovery sequences [112], and magnetization transfer models [80].

4.6. Conclusion

This work developed a generic framework for model-based reconstruction using the Bloch equations. The approach is validated numerically and tested experimentally using phantom and in vivo scans.

Acknowledgments

We thank Moritz Blumenthal and Christian Holme for discussions and help with BART.

This project was supported by the DZHK (German Centre for Cardiovascular Research), and funded in part by the Deutsche Forschungsgemeinschaft (DFG, German Research Foundation) under Germany's Excellence Strategy - EXC 2067/1- 390729940, and funded in part by NIH under grant U24EB029240. We also gratefully acknowledge the support of the NVIDIA corporation with the donation of one NVIDIA TITAN Xp GPU for this research.

Data Availability

The data of this work was uploaded to Zenodo @doi:10.5281/zenodo.7654462.
The scripts reproducing all figures of this manuscript are published at Github @mrirecon/bloch-moba.
The reconstruction code is implemented in BART with commit `0c847a2`.
A tutorial about the usage of the Bloch model-based reconstruction with BART can be found at Github @mrirecon/bloch-tutorial.

4.7. Appendix

4.7.1. Combining Sensitivity Analysis With a State-Transition Matrix Simulation

The system matrix $\boldsymbol{A}(t)$ in equation 4.10 can be extended to include the sensitivity analysis for the three partial derivatives R_1, R_2 and B_1:

$$\boldsymbol{A}(t) = \begin{pmatrix}
-R_2 & \gamma B_z(t) & -\gamma \sin(\phi(t)) B_1(t) B_z(t) & 0 & 0 & 0 & 0 & 0 & 0 & 0 & 0 & 0 & 0 \\
-\gamma B_z(t) & -R_2 & \gamma \cos(\phi(t)) B_1(t) B_z & 0 & 0 & 0 & 0 & 0 & 0 & 0 & 0 & 0 & 0 \\
\gamma \sin(\phi(t)) B_1(t) B_z(t) & -\gamma \cos(\phi(t)) B_1(t) B_z(t) & -R_1 & 0 & 0 & 0 & 0 & 0 & 0 & 0 & 0 & 0 & M_0 R_1 \\
0 & 0 & 0 & -R_2 & \gamma B_z(t) & -\gamma \sin(\phi(t)) B_1(t) B_z(t) & 0 & 0 & 0 & 0 & 0 & 0 & 0 \\
0 & 0 & 0 & -\gamma B_z(t) & -R_2 & \gamma \cos(\phi(t)) B_1(t) B_z(t) & 0 & 0 & 0 & 0 & 0 & 0 & 0 \\
0 & 0 & -1 & \gamma \sin(\phi(t)) B_1(t) B_z(t) & -\gamma \cos(\phi(t)) B_1(t) B_z(t) & -R_1 & 0 & 0 & 0 & 0 & 0 & 0 & M_0 \\
-1 & 0 & 0 & 0 & 0 & 0 & -R_2 & \gamma B_z(t) & -\gamma \sin(\phi(t)) B_1(t) B_z(t) & 0 & 0 & 0 & 0 \\
0 & -1 & 0 & 0 & 0 & 0 & -\gamma B_z(t) & -R_2 & \gamma \cos(\phi(t)) B_1(t) B_z(t) & 0 & 0 & 0 & 0 \\
0 & 0 & 0 & 0 & 0 & 0 & \gamma \sin(\phi(t)) B_1(t) B_z(t) & -\gamma \cos(\phi(t)) B_1(t) B_z(t) & -R_1 & 0 & 0 & 0 & 0 \\
0 & 0 & -\gamma \sin(\phi(t)) B_1(t) & 0 & 0 & 0 & 0 & 0 & 0 & -R_2 & \gamma B_z(t) & -\gamma \sin(\phi(t)) B_1(t) B_z(t) & 0 \\
0 & 0 & \gamma \cos(\phi(t)) B_1(t) & 0 & 0 & 0 & 0 & 0 & 0 & -\gamma B_z(t) & -R_2 & \gamma \cos(\phi(t)) B_1(t) B_z(t) & 0 \\
\gamma \sin(\phi(t)) B_1(t) & -\gamma \cos(\phi(t)) B_1(t) & 0 & 0 & 0 & 0 & 0 & 0 & 0 & \gamma \sin(\phi(t)) B_1(t) B_z(t) & -\gamma \cos(\phi(t)) B_1(t) B_z(t) & -R_1 & 0 \\
0 & 0 & 0 & 0 & 0 & 0 & 0 & 0 & 0 & 0 & 0 & 0 & 0
\end{pmatrix}.$$

with its corresponding parameter vector from equation 4.9:

$$\boldsymbol{M}(t) \rightarrow \boldsymbol{x}(t) = \begin{pmatrix}
M_x(t) \\ M_y(t) \\ M_z(t) \\ Z_{R_1,x}(t) \\ Z_{R_1,y}(t) \\ Z_{R_1,z}(t) \\ Z_{R_2,x}(t) \\ Z_{R_2,y}(t) \\ Z_{R_2,z}(t) \\ Z_{B_1,x}(t) \\ Z_{B_1,y}(t) \\ Z_{B_1,z}(t) \\ 1
\end{pmatrix}. \tag{4.23}$$

4.7.2. Forward Model Derivatives

The derivative of $\mathcal{A}$ in equation 4.19 follows by exploiting the Jacobi matrix and the product rule similar to [9, 36]:

$$D\mathcal{A}(\boldsymbol{x})\begin{pmatrix} \mathrm{d}R_1 \\ \mathrm{d}R_2 \\ \mathrm{d}M_0 \\ \mathrm{d}B_1 \\ \mathrm{d}c_1 \\ \vdots \\ \mathrm{d}c_N \end{pmatrix} = \begin{pmatrix} \mathcal{PF}\left(\mathrm{d}c_1 M_{t_1} + c_1\left[\frac{\partial M_{t_1}}{\partial R_1}\mathrm{d}R_1 + \frac{\partial M_{t_1}}{\partial R_2}\mathrm{d}R_2 + \frac{\partial M_{t_1}}{\partial M_0}\mathrm{d}M_0 + \frac{\partial M_{t_1}}{\partial B_1}\mathrm{d}B_1\right]\right) \\ \vdots \\ \mathcal{PF}\left(\mathrm{d}c_N M_{t_1} + c_N\left[\frac{\partial M_{t_1}}{\partial R_1}\mathrm{d}R_1 + \frac{\partial M_{t_1}}{\partial R_2}\mathrm{d}R_2 + \frac{\partial M_{t_1}}{\partial M_0}\mathrm{d}M_0 + \frac{\partial M_{t_1}}{\partial B_1}\mathrm{d}B_1\right]\right) \\ \vdots \\ \mathcal{PF}\left(\mathrm{d}c_N M_{t_n} + c_N\left[\frac{\partial M_{t_n}}{\partial R_1}\mathrm{d}R_1 + \frac{\partial M_{t_n}}{\partial R_2}\mathrm{d}R_2 + \frac{\partial M_{t_n}}{\partial M_0}\mathrm{d}M_0 + \frac{\partial M_{t_n}}{\partial B_1}\mathrm{d}B_1\right]\right) \end{pmatrix}. \tag{4.24}$$

The adjoint of the derivative becomes

$$D\mathcal{A}^H(\boldsymbol{x})\begin{pmatrix} y_{1,1} \\ y_{2,1} \\ \vdots \\ y_{n,N} \end{pmatrix} = \begin{pmatrix} \mathrm{d}R_1 \\ \mathrm{d}R_2 \\ \mathrm{d}M_0 \\ \mathrm{d}B_1 \\ \mathrm{d}c_1 \\ \vdots \\ \mathrm{d}c_N \end{pmatrix} = \begin{pmatrix} \sum_{j=1}^{N}\sum_{k=1}^{n}\overline{\left(\frac{\partial M_{t_k}}{\partial R_1}\right)}\cdot\overline{c_j}\cdot\mathcal{F}^{-1}\left[\mathcal{P}^H y_{k,j}\right] \\ \sum_{j=1}^{N}\sum_{k=1}^{n}\overline{\left(\frac{\partial M_{t_k}}{\partial R_2}\right)}\cdot\overline{c_j}\cdot\mathcal{F}^{-1}\left[\mathcal{P}^H y_{k,j}\right] \\ \sum_{j=1}^{N}\sum_{k=1}^{n}\overline{\left(\frac{\partial M_{t_k}}{\partial M_0}\right)}\cdot\overline{c_j}\cdot\mathcal{F}^{-1}\left[\mathcal{P}^H y_{k,j}\right] \\ \sum_{j=1}^{N}\sum_{k=1}^{n}\overline{\left(\frac{\partial M_{t_k}}{\partial B_1}\right)}\cdot\overline{c_j}\cdot\mathcal{F}^{-1}\left[\mathcal{P}^H y_{k,j}\right] \\ \sum_{k=1}^{n}\overline{M_{t_k}}\cdot\mathcal{F}^{-1}\left[\mathcal{P}^H y_{k,1}\right] \\ \vdots \\ \sum_{k=1}^{n}\overline{M_{t_k}}\cdot\mathcal{F}^{-1}\left[\mathcal{P}^H y_{k,N}\right] \end{pmatrix}. \tag{4.25}$$

4.7.3. Look-Locker Reparameterization

The Look-Locker model represents a special solution of the Bloch equations for an IR-FLASH sequence [42]. It assumes a perfect inversion, a small flip angle and short repetition times compared to the relaxation effects. Initial relaxation effects between the inversion and the first echo can be compensated analytically [107]. The original formulation of the Look-Locker model with the parameters M_0, M_{ss} and R_1^* is

$$M_z(M_{ss}, M_0, R_1^*, t) = M_{ss} - (M_{ss} + M_0)\cdot e^{-R_1^*\cdot t}\ . \tag{4.26}$$

These parameters are related to the underlying physical parameters M_0, R_1 and α_{eff}. With the assumption of short repetition times [113]

$$\frac{M_0}{M_{ss}} = \frac{R_1^*}{R_1} \tag{4.27}$$

the effective relaxation rate

$$R_1^* = R_1 + R_1' = R_1 - \frac{1}{\mathrm{TR}} \ln \cos \alpha_{\mathrm{eff}} \tag{4.28}$$

splits into R_1 and the readout relaxation rate R_1' determined by the effective flip angle α_{eff} [43]. The reparameterized Look-Locker model can be formulated as

$$M_z(M_0, R_1, R_1', t) = M_0 \cdot \left(\frac{R_1}{R_1 + R_1'} - \left(1 + \frac{R_1}{R_1 + R_1'} \right) \cdot e^{-(R_1 + R_1')t} \right). \tag{4.29}$$

Here, Equation 4.29 depends directly on the physical parameters M_0, R_1 and $R_1' = -\frac{1}{\mathrm{TR}} \ln \cos \alpha_{\mathrm{eff}}$ and allows adding prior knowledge about smooth B1 maps [107, 114] to the reconstruction [43]. This reparameterized model can be directly compared to a Bloch model-based reconstruction using the same set of parameters.

4.7.4. Scaling Factors

The output of the forward operator $\mathcal{B}$ in equation 4.19 is the strength of the signal estimated by the Bloch simulation and its partial derivatives. The strength of the signal depends on the sequence and especially the applied flip angle. Therefore, the signals output differs for classical FLASH or bSSFP sequences influencing the weighting between the data fidelity and regularization terms changing the optimization behavior.

A generic reconstruction aims for robustness against variations of the sequence parameters. It requires a scaling of the signal and its partial derivatives simulated within $\mathcal{B}$. The implemented scaling is motivated by the Look-Locker model assumption that the longitudinal magnetization M_z in equation 4.29 is proportional to the measured signal M_{xy} and scaled to 1. Thus, the signal of a simulation with an initial magnetization of length 1 requires scaling of the simulated signal output M_{xy} by the applied flip angle α and the relaxation effect $e^{-\frac{t_{\mathrm{TE}}}{T_2}}$ during the echo time interval Δt_{TE}:

$$M_z = \frac{e^{-\frac{\Delta t_{\mathrm{TE}}}{T_2}}}{\sin \alpha} \cdot M_{xy} \, . \tag{4.30}$$

Because of the short echo times of the sequences used in this work, the T_2 relaxation effect can be neglected. This assumption avoids additional T_2 dependencies of the estimated derivatives. The final scaling factor $\frac{1}{\sin \alpha}$ increases the robustness of the forward operator $\mathcal{B}$ in equation 4.19 to the choice of the applied flip angle in FLASH based sequences. For a bSSFP type sequence the flip angle in equation 4.30 needs to be halved to take its dynamics on the $\alpha/2$ cone into account [49].

4.7.5. IR-bSSFP Information Encoding

The IR-bSSFP signal behavior is described by a limited exponential growth similar to the IR-FLASH sequence [3]. A single inversion recovery can encode information for estimating 3 parameters. While the IR-FLASH sequence is sensitive to exactly 3 parameters, the IR-bSSFP is also sensitive to T_2, leading to 4 parameters in total. With a single limited exponential growth this additional parameter can not be encoded and two parameters need to be coupled. For bSSFP sequences the relaxation parameters T_1 and T_2 are coupled. Prior knowledge about B_1 can be used to decouple both relaxation parameters [3, 115, 116].

4.7.6. Symbolic Derivatives of IR-bSSFP

The analytical signal model for an IR-bSSFP can be derived from the Bloch equations with the assumptions of hard RF pulses, a perfect inversion and an ideal $\alpha/2 - \mathrm{TR}/2$ magnetization preparation.

The signal is modelled by [3]:

$$M(M_{ss}, M_0^*, R_1^*, t) = M_{ss} - (M_0^* + M_{ss}) \cdot e^{-R_1^* \cdot t} \tag{4.31}$$

with

$$\begin{aligned} R_1^* &= R_1 \cos^2\left(\frac{\alpha}{2}\right) + R_2 \sin^2\left(\frac{\alpha}{2}\right) \\ M_{ss} &= \frac{M_0(1-E_1)\sin\alpha}{1-(E_1-E_2)\cos\alpha - E_1E_2} \\ &\underset{\mathrm{TR}<<T_{1,2}}{=} \frac{M_0 \sin\alpha}{\left(\frac{R_1}{R_2}+1\right) - \cos\alpha \cdot \left(\frac{R_2}{R_1}-1\right)} \\ M_0^* &= M_0 \sin\left(\frac{\alpha}{2}\right) \end{aligned} \tag{4.32}$$

for

$$E_{1,2} = e^{-R_{1,2} \cdot t} \,. \tag{4.33}$$

This can be reparameterized to the physical parameters R_1, R_2, M_0 and α:

$$
\begin{aligned}
M(R_1, R_2, M_0, \alpha, t) = & \frac{M_0 \sin\alpha}{\frac{R_2}{R_1} + 1 - \cos\alpha\left(\frac{R_2}{R_1} - 1\right)} \\
& - \frac{M_0 \sin\alpha \cdot e^{-R_1 \cos^2\left(\frac{\alpha}{2}\right)\cdot t - R_2 \sin^2\left(\frac{\alpha}{2}\right)\cdot t}}{\frac{R_2}{R_1} + 1 - \cos\alpha\left(\frac{R_2}{R_1} - 1\right)} \\
& - M_0 \sin\left(\frac{\alpha}{2}\right) \cdot e^{-R_1 \cos^2\left(\frac{\alpha}{2}\right)\cdot t - R_2 \sin^2\left(\frac{\alpha}{2}\right)\cdot t}
\end{aligned} \tag{4.34}
$$

with its symbolic derivatives:

$$
\begin{aligned}
\frac{\partial M(R_1,R_2,M_0,\alpha,t)}{\partial R_1} = & -M_0 R_2 \sin\alpha \cdot (\cos\alpha - 1) \cdot \frac{1 - C(R_1, R_2, \alpha, t)}{B^2(R_1, R_2,\alpha)} \\
& + M_0 R_1 t \sin\alpha \cos\left(\frac{\alpha}{2}\right) \cdot \frac{C(R_1, R_2, \alpha, t)}{B(R_1, R_2,\alpha)} \\
& + M_0 t \sin\left(\frac{\alpha}{2}\right) \cos^2\left(\frac{\alpha}{2}\right) \cdot C(R_1, R_2, \alpha, t)
\end{aligned} \tag{4.35}
$$

$$
\begin{aligned}
\frac{\partial M(R_1,R_2,M_0,\alpha,t)}{\partial R_2} = & M_0 R_1 \sin\alpha \cdot (\cos\alpha - 1) \cdot \frac{1 - C(R_1, R_2, \alpha, t)}{B^2(R_1, R_2,\alpha)} \\
& + M_0 R_1 t \sin\alpha \sin^2\left(\frac{\alpha}{2}\right) \cdot \frac{C(R_1, R_2, \alpha, t)}{B(R_1, R_2,\alpha)} \\
& + M_0 t \sin^3\left(\frac{\alpha}{2}\right) \cdot C(R_1, R_2, \alpha, t)
\end{aligned} \tag{4.36}
$$

$$
\begin{aligned}
\frac{\partial M(R_1,R_2,M_0,\alpha,t)}{\partial \alpha} = & \frac{M_0 R_1 \sin^2\alpha (R_2 - R_1) \cdot (C(R_1, R_2, \alpha, t) - 1)}{B^2(R_1, R_2,\alpha)} \\
& - \frac{M_0 R_1 \sin\alpha \cdot C(R_1, R_2, \alpha, t) t \sin\left(\frac{\alpha}{2}\right) \cos\left(\frac{\alpha}{2}\right) (R_1 - R_2)}{B(R_1, R_2,\alpha)} \\
& - \frac{M_0 R_1 \cos\alpha \cdot (C(R_1, R_2, \alpha, t) - 1)}{B(R_1, R_2,\alpha)} \\
& - \frac{M_0}{2} \cos\left(\frac{\alpha}{2}\right) \cdot C(R_1, R_2, \alpha, t) \\
& - M_0 \sin^2\left(\frac{\alpha}{2}\right) \cos\left(\frac{\alpha}{2}\right) (R_1 - R_2) \cdot C(R_1, R_2, \alpha, t) t
\end{aligned} \tag{4.37}
$$

$$\begin{aligned}\frac{\partial M(R_1,R_2,\alpha,t)}{\partial M_0} = & \frac{\sin\alpha}{\frac{R_2}{R_1}+1-\cos\alpha\left(\frac{R_2}{R_1}-1\right)} \\ & - \frac{\sin\alpha\cdot e^{-R_1\cos^2\left(\frac{\alpha}{2}\right)\cdot t - R_2\sin^2\left(\frac{\alpha}{2}\right)\cdot t}}{\frac{R_2}{R_1}+1-\cos\alpha\left(\frac{R_2}{R_1}-1\right)} \\ & - \sin\left(\frac{\alpha}{2}\right)\cdot e^{-R_1\cos^2\left(\frac{\alpha}{2}\right)\cdot t - R_2\sin^2\left(\frac{\alpha}{2}\right)\cdot t}\end{aligned} \tag{4.38}$$

with

$$\begin{aligned}B(R_1,R_2,\alpha) &= (R_1-R_2)\cos\alpha + R_1 + R_2 \\ C(R_1,R_2,\alpha,t) &= \exp\left(-R_1\cos^2\left(\frac{\alpha}{2}\right)\cdot t - R_2\sin^2\left(\frac{\alpha}{2}\right)\cdot t\right)\ .\end{aligned} \tag{4.39}$$

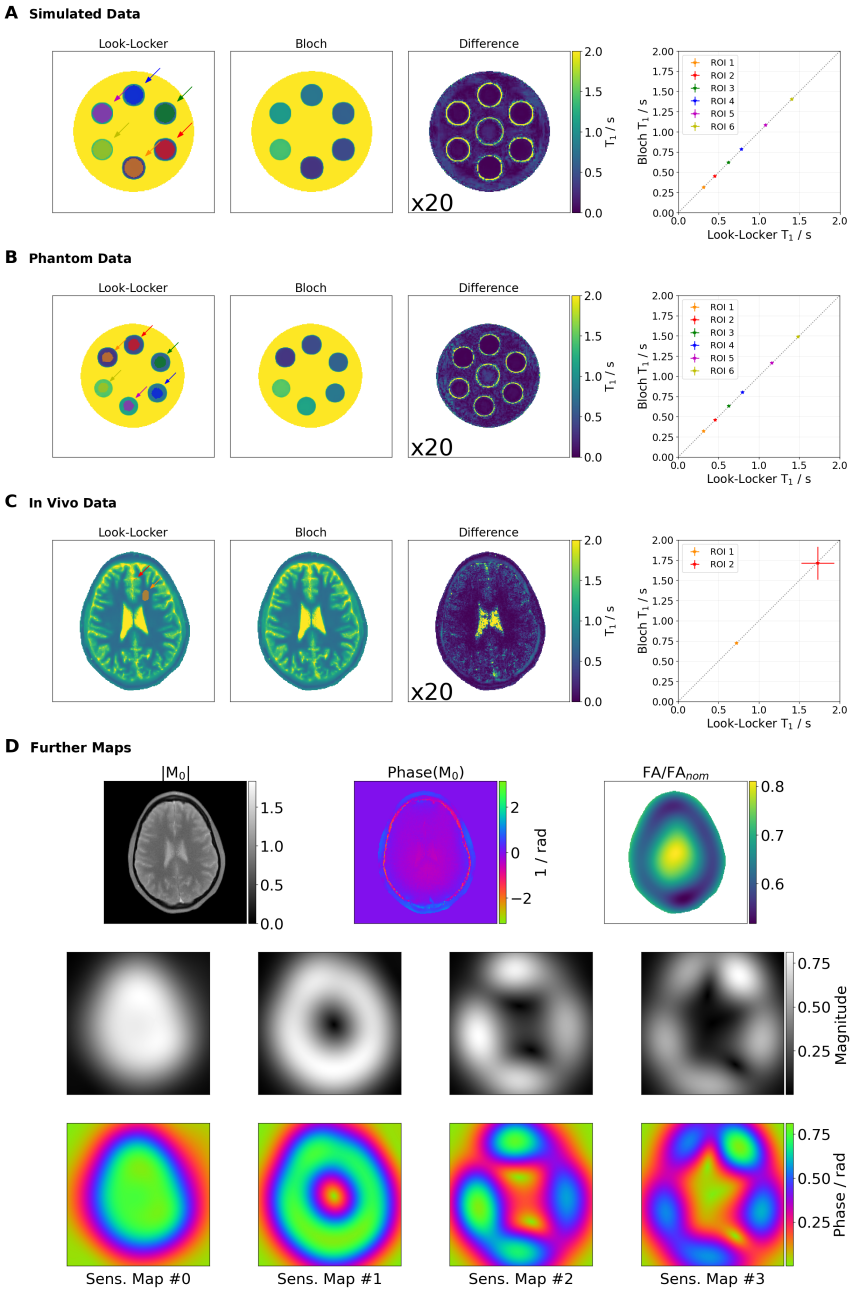

Figure 4.4: Reconstructed T_1 parameter maps for radial single-shot IR-FLASH data acquired from a numerical (**A**) and measured phantom (**B**) as well as a human brain (**C**). The Bloch model-based reconstruction and the differences between the two methods are shown in the middle. The difference map is scaled up by a factor of 20 to improve visualization. On the right the T_1 values of the color-coded ROIs (arrows) of the Bloch reconstruction vs. Look-Locker reconstruction are plotted together with standard deviations. Besides the in vivo T_1 map presented in **C**, the Bloch model-based technique reconstructs a complex valued M_0 map, a relative flip angle map and complex coil sensitivities shown in **D**.

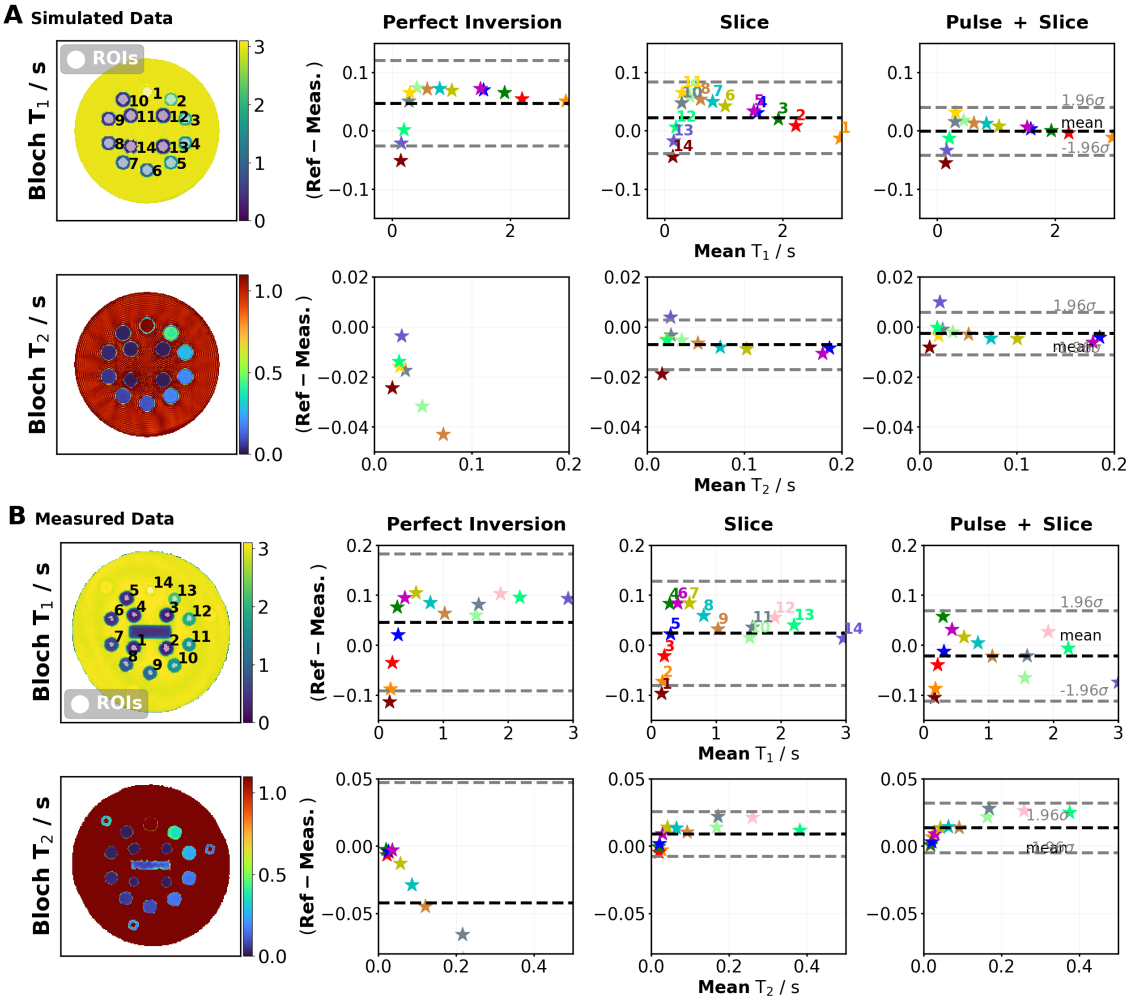

Figure 4.5: **A**: Reconstructed T_1 and T_2 parameter maps and the corresponding ROI values for numerical radial single-shot IR-bSSFP data of a digital multi-coil reference object simulated in k-space. The left side shows the reconstructed parameter maps and the right the ROI analysis results in Bland-Altman plots relative to the simulated reference values. The analyzed ROIs are marked and numbered in the T_1 map. **B**: Reconstructed T_1 and T_2 parameter maps and the corresponding ROI values for a radial single-shot IR-bSSFP measurement of the T_2 spheres of the NIST system phantom. The left side corresponds to the rightmost ROI analysis. The right side presents the comparison of the analyzed ROIs reconstructed with the Bloch model-based technique for various signal model assumptions compared with gold-standard reference values in Bland-Altman plots. For improved visualization individual outliers are removed from the plot.

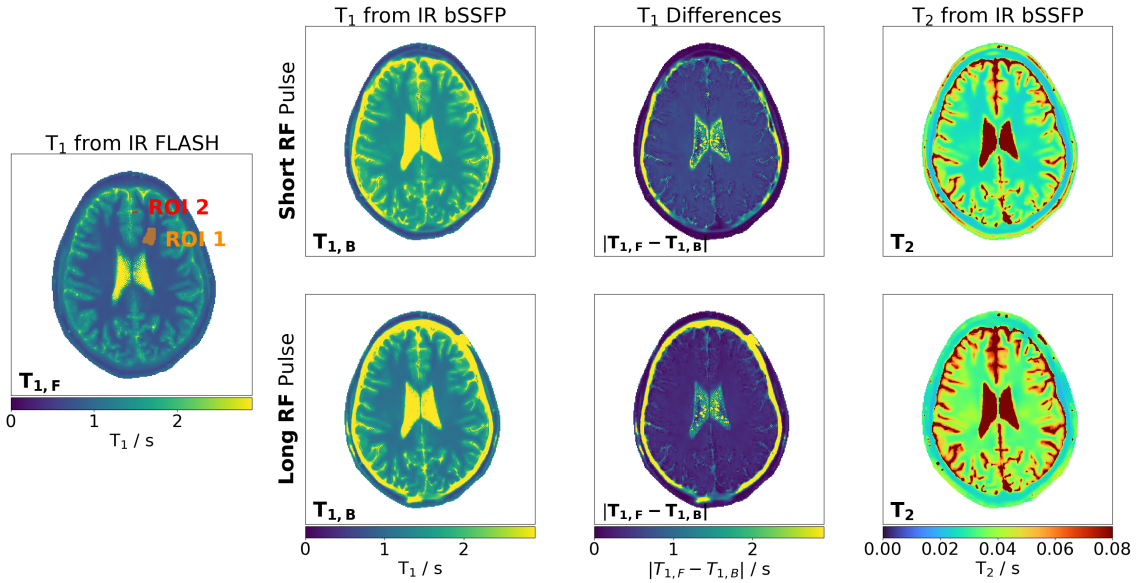

Figure 4.6: The T_1 parameter map reconstructed from a radial single-shot IR-FLASH in vivo dataset with a Look-Locker model-based reconstruction is shown on the left. It also shows the reconstructed T_1 parameter maps of a radial single-shot IR-bSSFP in vivo dataset acquired on the same brain slice for short RF pulses (T_{RF}: 1 ms, TR: 4.88 ms) on the top and long RF pulses (T_{RF}: 2.5 ms, TR: 10.8 ms) on the bottom reconstructed with the Bloch model-based reconstruction. In the center column the difference maps are shown. The values corresponding to the colored ROIs are listed in Table 4.2. On the right the T_2 parameter maps for the short and long RF pulse experiments are shown reconstructed from the IR-bSSFP sequence.

Table 4.1: Table listing the sequence parameters for the performed measurements of this work.

Sequence	IR-FLASH		IR-bSSFP			Turbo FLASH		Spin-Echo	
Object	phantom	in vivo	phantom	in vivo	in vivo	phantom	in vivo	phantom	phantom
Figure	4.4.B	4.4.C, 4.4.D, 4.6.B	4.5	4.6	4.6	4.5	4.6	4.5	4.5
TR|TE [ms]	4.1|1.84	4.1|2.58	4.88|2.44	4.88|2.44	10.8|5.4	2000|2.14	2000|2.14	8000|15	8000|(15:40:455)
FA [°]	6	6	45	45	45	8	8	-	-
T_{RF} [ms]	1	1	1	1	2.5	-	-	-	-
Nominal Slice Thickness [mm]	5	5	5	5	5	5	5	5	5
Repetitions	1020	1000	1000	1000	500	1	1	1	1
Coils	20	20	20	20	20	20	20	20	20
BWTP	4	4	4	4	4	-	-	-	-
BR	256	256	192	256	256	192	256	256	256
FoV [mm]	192	200	200	200	200	200	200	200	200
Duration [min:s]	0:04	0.04	0:05	0:05	0:06	0:04	0:04	34:16	34:16
others	#tiny GA=7	#tiny GA=7	#tiny GA=7	#tiny GA=7	#tiny GA=7			T_{inv}=30:250:2530 ms	

Table 4.2: Table listing the single-shot in vivo IR-bSSFP ROI analysis results presented in Figure 4.6.

	$T_{1,\text{IR-FLASH}}$ [s]	$T_{1,\text{IR-bSSFP, short}}$ [s]	$T_{1,\text{IR-FLASH, long}}$ [s]	$T_{2,\text{IR-bSSFP, short}}$ [s]	$T_{2,\text{IR-bSSFP, long}}$ [s]
ROI 1	0.737±0.016	1.35±0.019	1.061±0.019	0.024±0.001	0.033±0.001
ROI 2	1.736±0.299	2.434±0.413	2.226±0.456	0.066±0.02	0.096±0.088

4.8. Supporting Information

S1. Supporting Figure S1

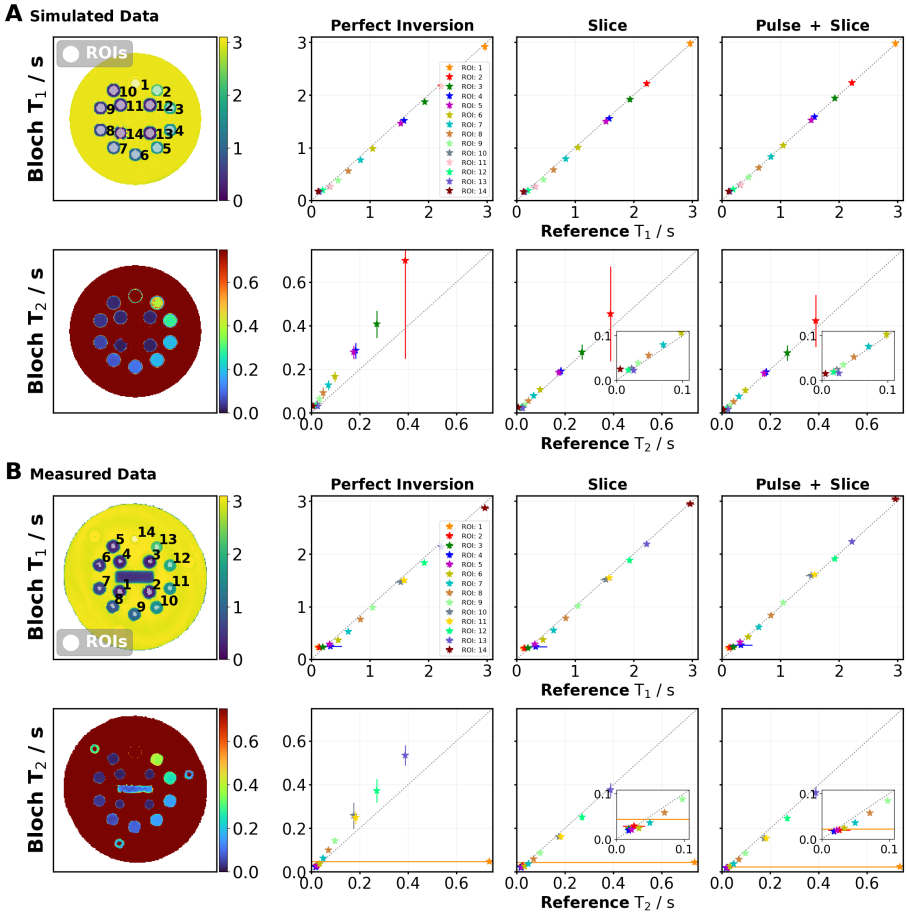

Figure S1: **A**: Reconstructed T_1 and T_2 parameter maps and the corresponding ROI values for numerical radial single-shot IR-bSSFP data of a digital multi-coil reference object simulated in k-space. The left side shows the reconstructed parameter maps and the right the ROI analysis results relative to the simulated reference values with standard deviations. The analyzed ROIs are marked and numbered in the T_1 map. **B**: Reconstructed T_1 and T_2 parameter maps with corresponding ROI values for a radial single-shot IR-bSSFP measurement of the T_2 spheres of the NIST phantom. The left side corresponds to the rightmost ROI analysis. The right side presents the comparison of the analyzed ROIs reconstructed with the Bloch model-based technique for various signal model assumptions. It is compared to gold-standard reference values.

S2. Supporting Figure S2

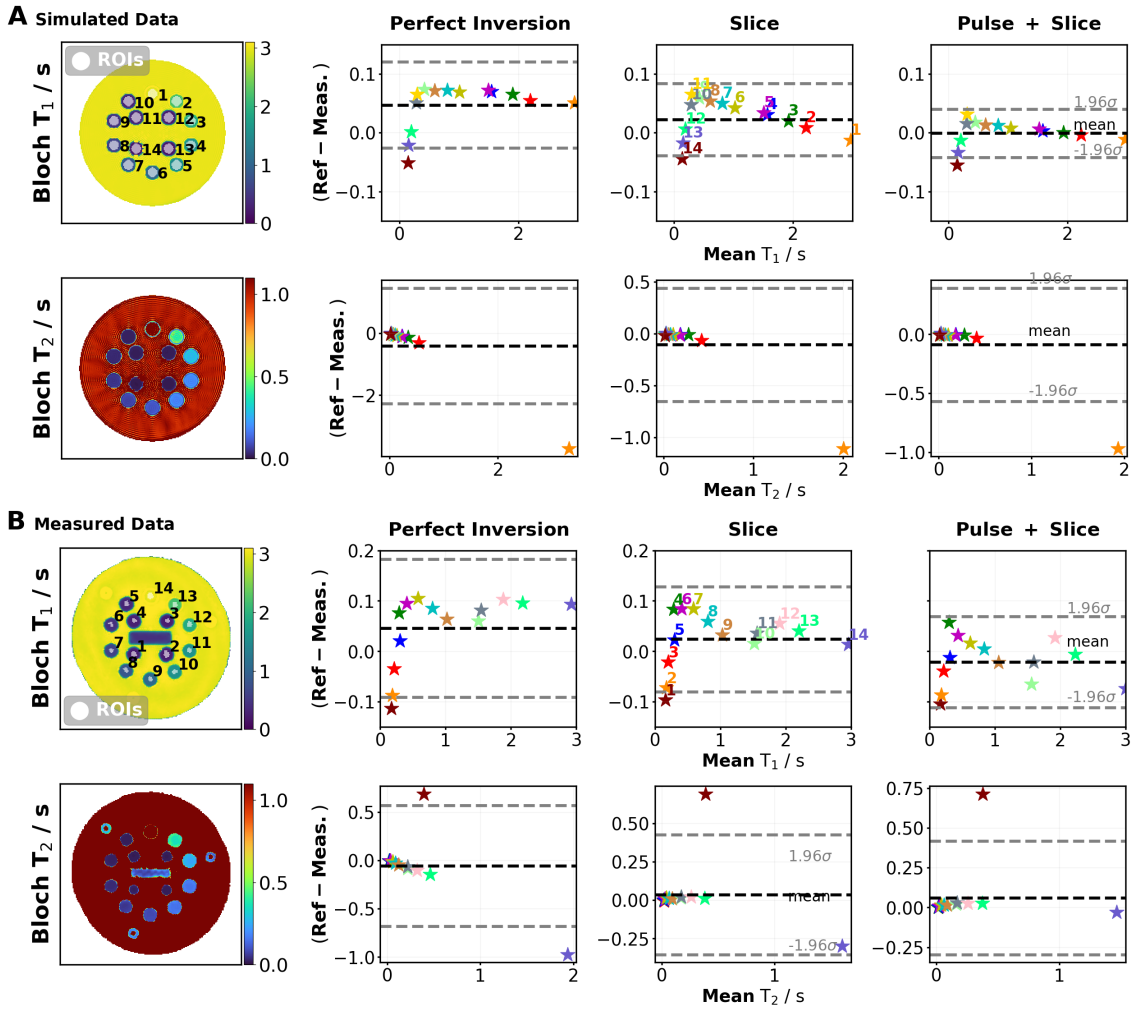

Figure S2: **A**: Reconstructed T_1 and T_2 parameter maps and all corresponding ROI values for simulated radial single-shot IR-bSSFP data. Here, the data points removed to improve the visualization in Figure 4.5 are included. Reconstructed parameter maps are shown on the left. Bland-Altman plots comparing to the simulated reference values are added on the right. The ROIs are marked and numbered in the T_1 map. **B**: Reconstructed T_1 and T_2 parameter maps and the corresponding ROI values for a radial single-shot IR-bSSFP measurement of the T_2 spheres of the NIST phantom. The left side corresponds to the rightmost ROI analysis. The right shows the Bland-Altman plots comparing the values of the ROIs reconstructed with the Bloch model-based technique for various assumptions used in the signal model compared with gold-standard reference values.

S3. Supporting Figure S3: Simulation Accuracy

This section discusses the simulation accuracy of the ODE solvers for different tolerances and sampling rates in more detail. In Figure S3.A reconstructions of the IR-FLASH phantom from Figure 4.4.B using the Bloch model-based reconstruction with signal model assumptions of only on-resonant spins and with spins distributed along a slice-selection gradient are shown. The reconstructions are performed with varying tolerances for the STM simulation method while keeping the initial step-size of the RK54 solver constant at 1E-4.

For the on-resonance results the difference values are small. Here, the reconstructed parameter maps for higher error tolerances are very similar to the reference map. For the signal model with simulation of the slice-selection gradient the reconstructed parameter maps are similar up to a tolerance of 0.001, while lower values result in large variations in the T_1 parameter map. The important result is that the error of the simulation from an STM tolerance value of 0.001 still allows accurate reconstructions even for complex spin dynamics.

In Figure S3.B the error plot from Figure 4.3 is extended to include more simulations with different tolerances and sampling rates. The required STM tolerance of 0.001 from Figure S3.A for complex dynamics is translated to the required sampling rate for the ROT simulation. It shows the point-wise errors (PWEs) for RK54, STM and ROT for the same simulation with slice-selection gradient. The tolerance value for the estimated limit of STM of 0.001 produces an error similar to the 1 MHz sampling rate. This leads to the conclusion that at least a sampling rate of 1 MHz is required for an accurate reconstruction of complex spin dynamics involving slice-selection gradients.

The simulation times for the same analysis with a slice-selection gradient, as presented in Figure 4.3, are shown in Figure S3.C for multiple tolerances and sampling rates.

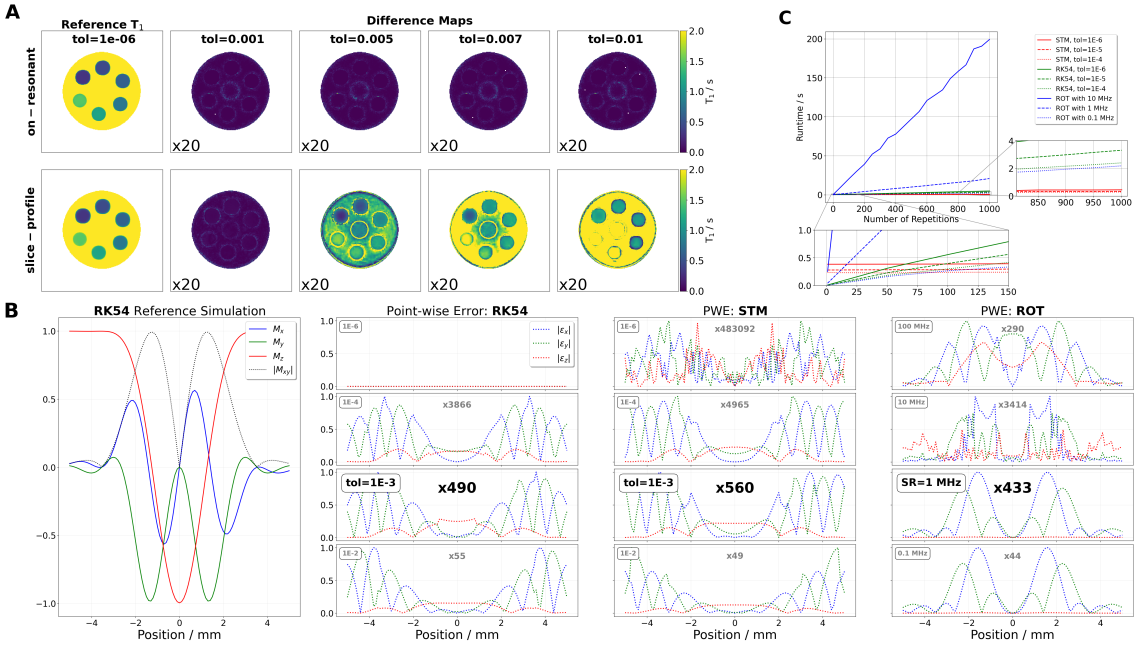

Figure S3: **A**: T_1 maps reconstructed from single-shot IR-FLASH (same as for Figure 4.4.B) with varying tolerances of the STM simulation. The forward model assumes on-resonant spins. The differences of the reconstructions for tolerances of 1e-5 to 1e-2 compared to the 1e-6 reference are shown in the bottom row. The differences are scaled by large factors for improved visualization. **B**: Extension of Figure 4.3.A with varying tolerances for RK54 and STM and sampling rates for ROT. **C**: Extension of Figure 4.3.B with varying tolerances for RK54 and STM and sampling rates for ROT.

S4. Supporting Figure S4

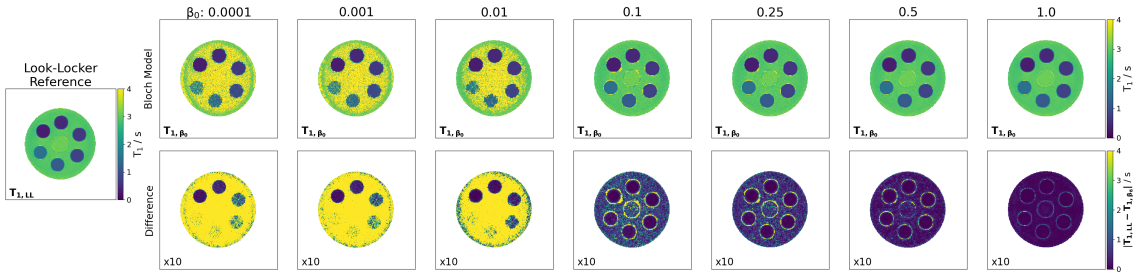

Figure S4: Reconstructed T_1 parameter maps similar to Figure 4.4.B for varying wavelet regularization strength β_0 for the Bloch model-based reconstruction (upper row). On the left a reference reconstruction estimated with the reparameterized Look-Locker model-based technique is shown. In the bottom row the differences between Bloch model-based reconstruction and the reference map are shown scaled by a factor of 10 for improved visualization.

S5. Supporting Figure S5: Influence of the Magnetization Transfer Effect

To estimate the influence of the magnetization transfer effect (MT) on the reconstructed T_1 parameter maps multiple single-shot IR-bSSFP experiments were performed with varying TR and T_{RF}. The sequence parameters are shown in Table S2. The analytical representation of the signal behavior during an IR-bSSFP experiment can be described by Equation (4.31). Following [115] the MT effect reduces the T_1^* and the steady-state magnetization M_{ss}, while not affecting M_0. They propose an exponential model for correction of the effect of MT on M_{ss}:

$$M_{ss}(\beta) = \left(M_{ss}^{\text{no MT}} - M_{ss}^{\text{full MT}}\right) \cdot \left(1 - e^{-k\cdot\beta}\right) + M_{ss}^{\text{full MT}} \tag{4.40}$$

Here, the signal which is not affected by MT is denoted as $M_{ss}^{\text{no MT}}$, the signal from a fully-saturated solid pool is $M_{ss}^{\text{full MT}}$, the rate constant is k and the increase in RF pulse duration is β.

The T_1 value for an IR-bSSFP can be estimated by

$$T_1 = \frac{T_1^*}{M_{ss}} M_0 \cos(\frac{\alpha}{2}) \tag{4.41}$$

with the flip angle α.

Taking into account that T_1^* is less affected by MT than M_{ss} [115], we assume that the MT influence on T_1 follows the model:

$$T_1(\beta) \approx \frac{1}{(a-b)\cdot\left(1 - e^{-k'\cdot\beta}\right) + b}\,. \tag{4.42}$$

Equation 4.42 is fitted to the different relaxation parameters from various acquisitions with different TR and T_{RF} (Figure S5).

The estimated parameters a, b and k' have no direct physical interpretation, but can be used to interpolate an MT-free T_1 for $\beta \rightarrow \infty$. The parameters of the fits are shown in Table S1.

The results for $T_1(\beta \rightarrow \infty)$ suggest that the MT effect plays a significant role in the T_1 offset observed in Figure 4.6, but also indicates that it might not explain the complete discrepancy.

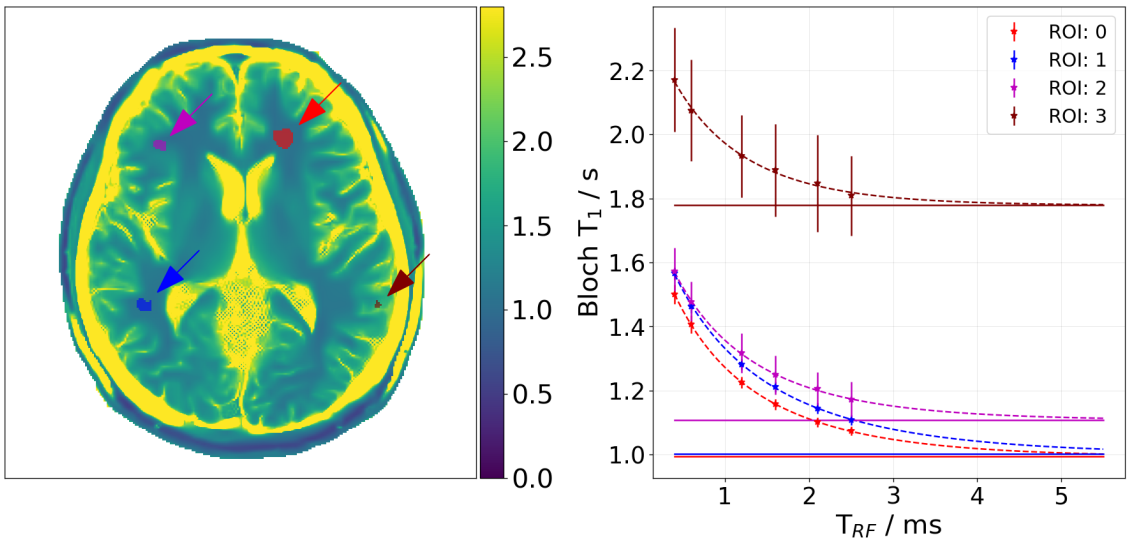

Figure S5: Visualization of the magnetization transfer effect in T_1 maps reconstructed from an IR-bSSFP sequence with varying TR and T_{RF}. On the left the T_1 map corresponding to the longest $T_{RF} = 2.5$ ms is plotted with colored ROIs. The mean values of the relaxation values for the colored areas are plotted with their standard deviation on the right for various lengths of RF pulses T_{RF}. The dotted lines represent the fitted functions following the analysis of Section S5.

S6. Supporting Figure S6

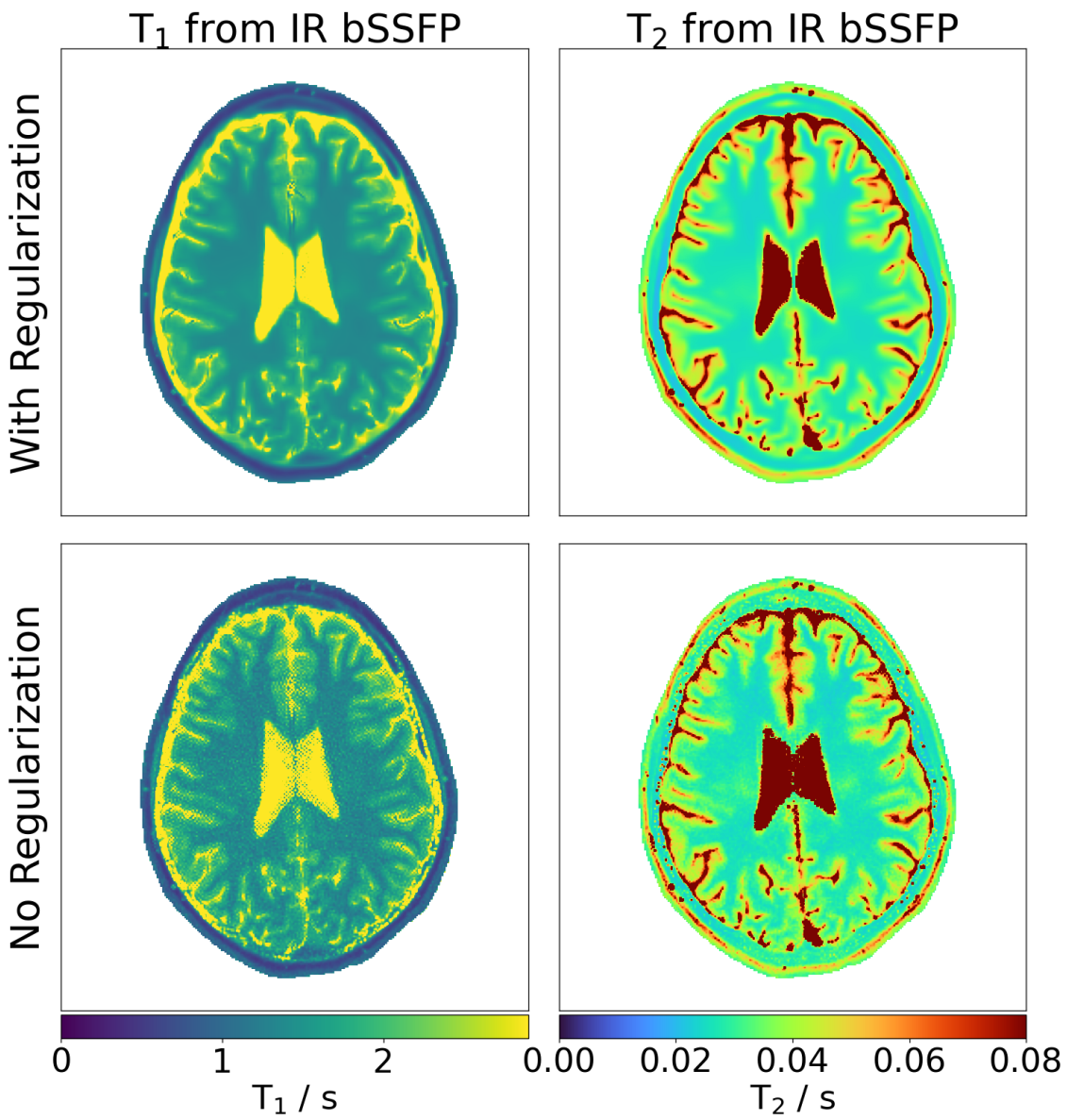

Figure S6: Bloch model-based reconstruction of an in vivo single-shot IR-bSSFP dataset acquired with 1 ms long RF pulses. The coil-sensitivities have been estimated with the regular Bloch model-based method and have been added as fixed prior knowledge to both reconstructions afterwards. The top presents the regularized reconstruction, while the bottom results do not include any regularization on the parameter maps.

S7. Supporting Table S1

Table S1: Table listing the fitting parameters estimated for Figure S5.

	a [s]	b [s]	k' [s]
ROI 1	0.931±0.006	0.510±0.003	0.723±0.023
ROI 2	0.923±0.013	0.498±0.005	0.620±0.041
ROI 3	0.834±0.01	0.498±0.006	0.786±0.059
ROI 4	0.519±0.007	0.382±0.008	0.992±0.158

S8. Supporting Table S2

Table S2: Table listing the sequence parameters for the analysis in Figure S5.

Sequence	IR-bSSFP	IR-bSSFP	IR-bSSFP	IR-bSSFP	IR-bSSFP	IR-bSSFP
Object	in vivo	in vivo	in vivo	in vivo	in vivo	in vivo
TR|TE [ms]	3.8|1.9	4.0|2.0	4.6|2.3	5|2.5	5.5|2.75	6.14|3.07
FA [°]	35	35	35	35	35	35
T_{RF} [ms]	0.4	0.6	1.2	1.6	2.1	2.5
Nominal Slice Thickness [mm]	5	5	5	5	5	5
Repetitions	1000	1000	1000	1000	1000	1000
Coils	20	20	20	20	20	20
BWTP	1	1	1	1	1	1
BR	256	256	256	256	256	256
FoV [mm]	200	200	200	200	200	200
Duration [min:s]	0:04	0.04	0:05	0:05	0:06	0:06
others	#tiny GA=13	#tiny GA=13	#tiny GA=13	#tiny GA=13	#tiny GA=14	#tiny GA=13

5. Additional Factors Affecting the Quantitative Accuracy

The Bloch model-based reconstruction is developed, verified and discussed in Chapter 4. Inversion-recovery fast low angle shot (IR-FLASH) datasets from numerical and physical phantoms as well as in vivo brain scans are successfully reconstructed, which result in accurate T_1 relaxation parameter maps. For inversion-recovery balanced steady-state free precession (IR-bSSFP) sequences, T_1 and T_2 are determined in a numerical and physical phantom study but show offsets to the expected references for in vivo datasets. While effects like magnetization transfer (MT) influence the accuracy of most parameter maps, as described in Section S5, they do not explain the full offset.
In this chapter, the effects of additional physical model inaccuracies and conceptual error sources in the optimization is investigated. In the beginning the robustness of the optimization with respect to the initialization of the parameter maps is tested. Further, the influence of different relaxation parameter distributions on the resulting parameter maps within the object is investigated. Afterwards, potential physical model discrepancies that result from field inhomogeneities, shimming procedures, and eddy currents are discussed. The validity of the data consistency in the optimization is verified with a pixel-wise fitting on reconstructed intermediate images. In the end, it is tested how averaged spokes influence the accuracy of the reconstructed parameter maps. The chapter closes with an investigation of the offset of the IR-bSSFP acquisition with respect to different flip angles.

5.1. General Initialization of the Reconstruction

Due to the high nonlinearity of combining the Bloch model with the parallel imaging (PI) model, the initialization of the parameter maps influences the convergence of the optimization. The analysis in this section investigates the sensitivity of the Bloch model-based reconstruction to its initialization. Therefore, T_1 and T_2 parameter maps are calculated from the same single-shot IR-bSSFP in vivo dataset but are reconstructed with different

initializations of the individual maps.

Methods A radially sampled single-shot IR-bSSFP dataset is acquired on a volunteer's brain with repetition time (TR)/echo time (TE)=4.88/2.44 ms, radio frequency (RF) pulse duration T_{RF}=1 ms, and a bandwidth time product (BWTP) of 4. More information on the acquisition is listed in Table 4.1. An additional preconditioned RF pulse sequence is used to acquire a B_1 map of the same slice. It is passed to the Bloch model-based reconstruction to improve the prior knowledge about the actual flip angles that are executed during the acquisition. The reconstruction is performed with a forward model that incorporates a slice profile simulation based on a known slice-selection gradient strength. 24 Bloch model-based reconstructions are carried out with varying initializations of $R_1 \in [0.5,1,2,3,5,10]$ Hz and $R_2 \in [1,5,10,20]$ Hz. For pre-conditioning similar to Wang [9], the individual parameter maps are scaled with the scalars s_{R_1}:s_{M_0}:s_{R_2}:s_{B_1}=1:1:30:0. The M_0 map is initialized with 1, while the B_1 map requires to be initialized with 0 because it is kept constant for IR-bSSFP reconstructions.

Results The reconstructed parameter maps for T_1 and T_2 are plotted in Figure 5.1 and 5.2. The reconstruction is robust over a large range of initialization values. While white matter relaxation parameters are close to 1 s for T_1 and close to 0.1 s for T_2 at the measured 3 T, the initialization leads to the same results for values from 1 to 5 Hz for R_1. The reconstruction is robust against changes in the initialization of R_2 for a robust choice of R_1. If R_1 is too large, changes in R_2 lead to strong artifacts in the reconstruction. This is observed in the combinations of (R_1/R_2) : (10/1), (10/5), (10/10) and (10/20) Hz.

Discussion The Bloch model-based reconstruction is robust for many initialization combinations of R_1 and R_2. R_2 showed a relatively higher robustness for a reasonable choice of R_1, which can result from the stronger enforced prior knowledge due to regularization and scaling with $s_{R_2} = 30$ during preconditioning. Artifacts always occur in the T_1 and T_2 map simultaneously due to the joint regularization of all parameter maps.

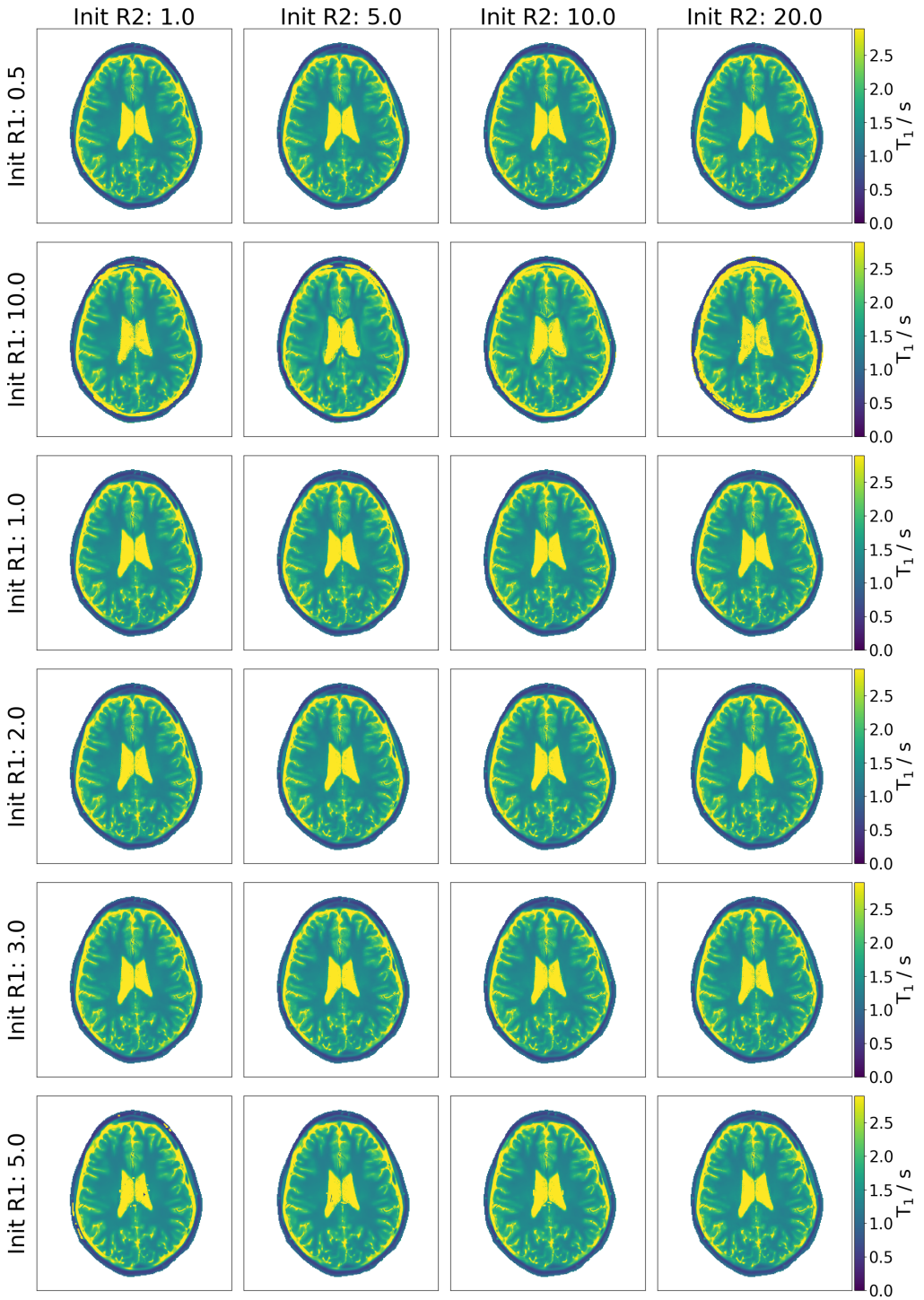

Figure 5.1: T_1 parameter maps reconstructed from single-shot IR-bSSFP data using the Bloch model-based reconstruction with different R_1 and R_2 initializations. The individual columns have constant R_2 and the rows constant R_1.

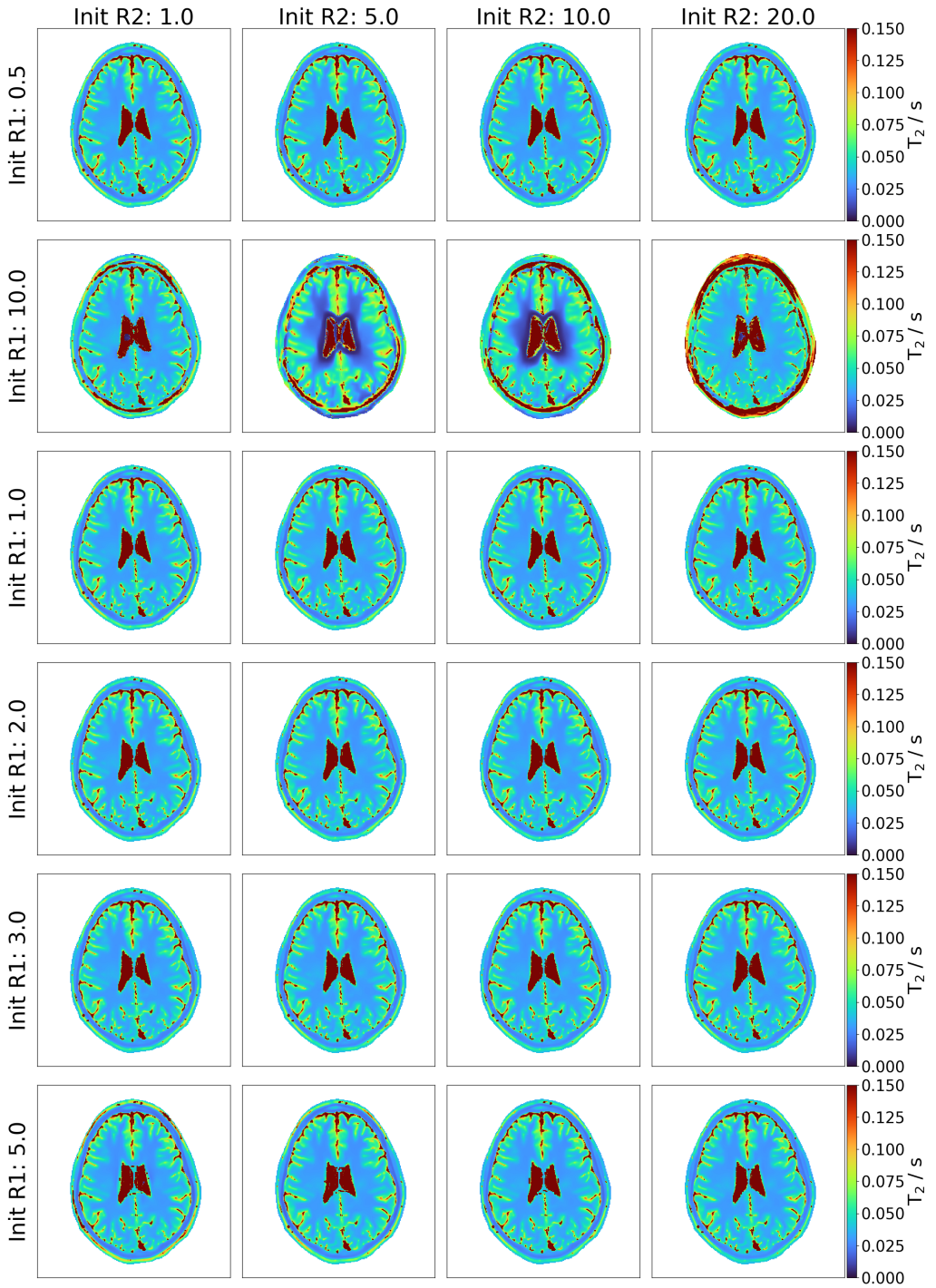

Figure 5.2: T_2 parameter maps reconstructed from single-shot IR-bSSFP data using the Bloch model-based reconstruction with different R_1 and R_2 initializations. The individual columns have constant R_2 and the rows constant R_1.

5.2. Effect of Parameter Distributions Within the Object

By formulating the entire reconstruction as a single nonlinear inverse problem, all parameter maps are calculated directly from k-space. This is generally ill-conditioned for small amounts of data and requires additional regularization which needs to be tuned manually. As the regularization is relative to the overall data scaling, its strength can be changed by different parameter distributions.
In this section, it is investigated how such relaxation parameter distributions can affect the quality of the reconstructed parameter maps.

Methods To investigate the influence of different parameter distributions, flexibility is required in changing the environment. While physical phantoms can be designed in such a manner that they have the same geometries with differently doped ingredients, additional experimental errors can not be excluded. Therefore, this analysis is based on a numerical phantom. Two NIST phantom geometries of the model number 130 are simulated with the Berkeley Advanced Reconstruction Toolbox (BART) following the acquisition with a single-shot IR-bSSFP sequence similarly to the analysis shown in Figure 4.5.A. The relaxation parameters of the small tubes are kept the same and the background values, which were set to water at 3 T (T_1 = 3 s and T_2 = 1 s), are changed to white matter with T_1/T_2=0.834/0.08 s [102]. All other simulation, regularization and Bloch model-based reconstruction parameters are kept the same. Multiple regions of interests (ROI) of the reconstructed T_1 and T_2 parameter maps are extracted and their mean values are compared to the known reference values, which were passed to the simulation tool.

Results The results of the reconstruction with the water and white matter background relaxation are presented in Figure 5.3. The error in both T_1 and T_2 for the most simplistic model (Perfect Inversion) is similar. The two more complex models with slice profile and additional hyperbolic secant inversion pulse are more accurate and precise in both parameter maps compared to the white matter background analysis, even though the relaxation rates of the inner tubes have not been changed.

Discussion The reconstruction results of the numerical NIST phantom with white matter background demonstrate the sensitivity of the current implementation of the nonlinear Bloch model-based reconstruction to different relaxation parameter distributions within the object. By choosing a lower background relaxation, the precision, and accuracy

of the smaller tubes increases, even though their reference relaxation characteristics have not been changed. This can result from different regularization strengths in both experiments. While the passed optimization parameters were kept the same in both reconstructions, the data in the current implementation is scaled internally before being further processes based on its l_2-norm. This is meant to increase the robustness of the reconstruction towards differently scaled datasets. The background relaxation parameters contribute strongly to the overall signal, which leads to different temporal evolutions of the overall signal. This effect can not be compensated for data scaling that is based on the l_2-norm. Thus, the relative strength of the regularization differs between both experiments, which influences the convergence and the solution of the optimization.
Another effect to consider is that the reconstruction incorporates an l_1 norm on the wavelet representation of the parameter maps to remove radial undersampling artifacts. This spatial constraint enforces smoothness in the maps, which can shift the tubes' relaxation values towards the background value. Even though the effect is weak, it can influence the water background experiments more strongly. This potentially leads to the reduced precision and accuracy. A future study should perform the same analysis without any regularization. While the precision of the parameter maps is expected to be reduced, it would provide valuable information about the influence on their accuracy.
In physical phantom models, strongly varying relaxation parameters typically go along with rapid changes in the susceptibility, which introduce inhomogeneities in the main magnetic field $\boldsymbol{B}_0$. This effect is not part of the simulation in this study, but is investigated in the following section.

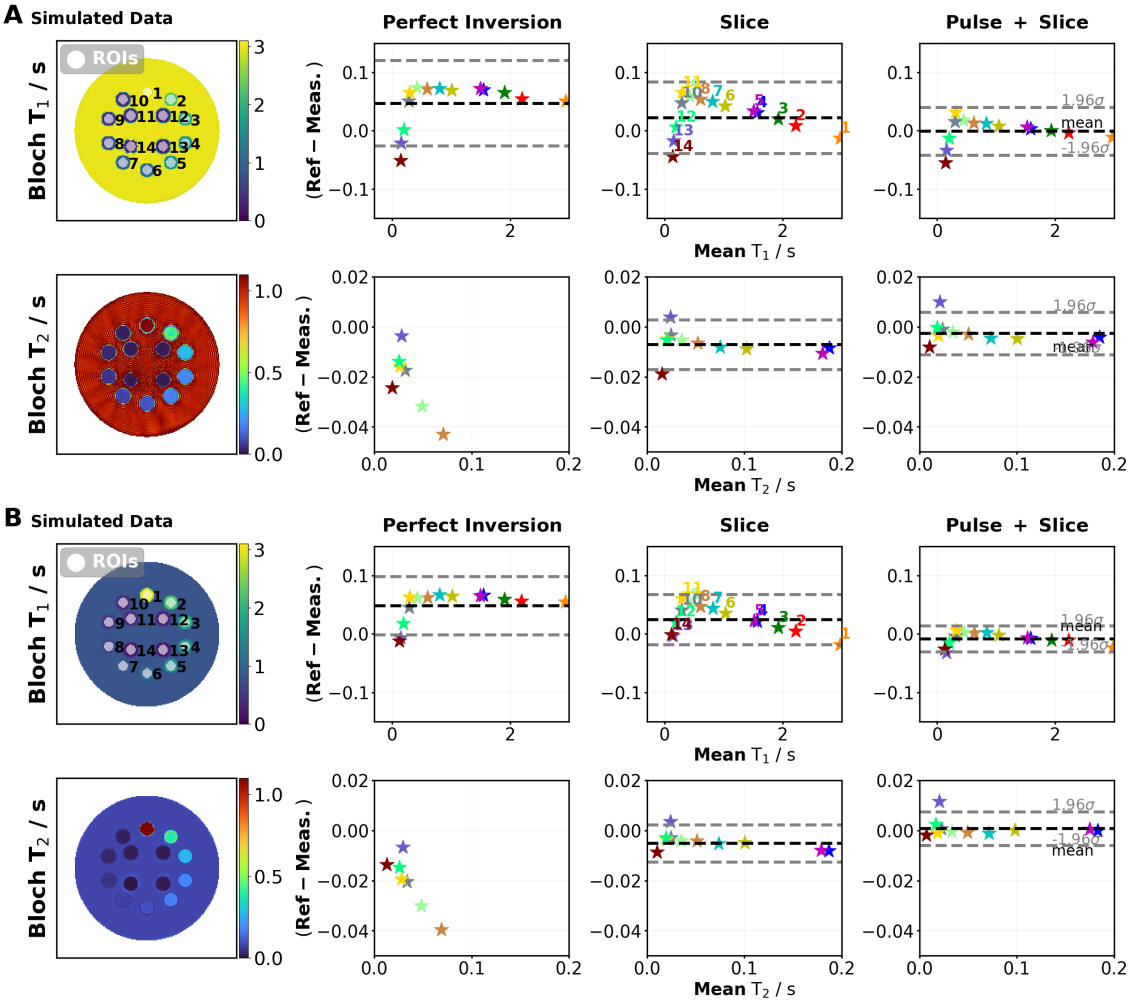

Figure 5.3: Comparison of reconstructions from simulated single-shot IR-bSSFP NIST phantom data with different background relaxations. For **A** and **B**, the same simulations and analyzes as for the numerical study presented in Figure 4.5 were performed. Both simulations only differ in their background relaxation values. **A** uses $T_1 = 3$ s and $T_2 = 1$ s to represent water at 3 T, and **B** uses values for white matter at 3 T ($T_1/T_2 = 0.834/0.08$ s) [102]. The most left column presents the reconstructed T_1 and T_2 parameter maps as well as the chosen region of interest (ROI) for the Bland-Altman analysis shown to its right. In the individual Bland-Altman plots the extracted ROI values are compared to the reference parameters that are passed to the simulation. The complexity of the forward model increases from the left to the right.

5.3. Influence of B_0 Inhomogeneities

Scanner systems in magnetic resonance imaging (MRI) are designed to provide a central volume with a homogeneous magnetic field $\boldsymbol{B}_0$. This homogeneity holds for single

substances with constant susceptibility but adding multiple different ones introduces susceptibility gradients. For the human head, these changes are strong close to the nasal cavities, where air and tissue are close together. The susceptibility differences introduce local changes in $\boldsymbol{B}_0$, which leads to off-resonances ω and changes the Larmor frequency during acquisition. If the forward model does not include ω, the reconstruction is physically biased towards a different solution and the accuracy of the mapping is reduced.
In the following analysis, the influence of $\boldsymbol{B}_0$ inhomogeneities ΔB_0 on the transient state signal of an IR-bSSFP sequence is investigated. The effect is simulated for representative ΔB_0 which are estimated from a volunteer's brain slice and their influence on analytically fitted relaxation parameters is observed. In the end, the Bloch model-based reconstruction is extended to include the prior knowledge about B_0 and to model them with pixel-wise off-resonances. The influence of this correction on the T_1 and the T_2 parameter maps that are reconstructed from in vivo single-shot IR-bSSFP data is presented.

Theoretical Background The magnetic (volume) susceptibility χ is a property of materials that defines their influence on external magnetic fields. It is defined by the relation between the magnetization $\boldsymbol{M}$ and the magnetic field strength $\boldsymbol{H}$:

$$\boldsymbol{M} = \chi \boldsymbol{H} \, . \tag{5.1}$$

The magnetic field $\boldsymbol{B}$ follows with χ and the permeability in a vacuum μ_0:

$$\boldsymbol{B} = \mu_0 (1 + \chi) \boldsymbol{H} \, . \tag{5.2}$$

It describes the change in $\boldsymbol{B}_0$ when heterogeneous materials are placed in it.
The inhomogeneities ΔB_0 in the main magnetic field $\boldsymbol{B}_0$ introduce variations of the resonance frequency,

$$\omega = \gamma \Delta B_0 \, , \tag{5.3}$$

which leads to additional precession effects and locally modified influences of RF pulses. A crucial part of this work is the IR-bSSFP sequence of the balanced steady-state free precession (bSSFP) type sequences, as introduced in Section 2.1.8. It is based on the assumption that the magnetization switches between two positions on opposite sites of the z-axis (Figure 5.4, top left). Being accurately prepared, the magnetization follows a transient state located on a cone. It requires a phase difference of π rad between consecutive RF excitations and balanced gradient moments.

The bSSFP sequences are sensitive to field inhomogeneities ΔB_0 because they introduce additional rotations during each TR. This moves the magnetization away from its ideal position on the cone. The effect is illustrated in the top center of Figure 5.4. With an increased rotation during TE, the signal intensity rapidly decreases[1] for higher ΔB_0 until it vanishes for $\Delta B_0 = \boldsymbol{\pi}$. This results in characteristic banding artifacts, which are visualized on the bottom of Figure 5.4.

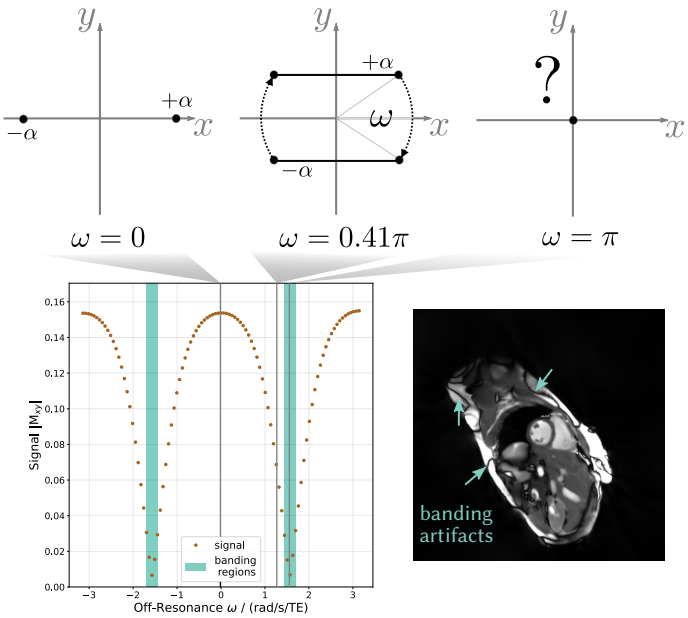

Figure 5.4: Visualization of banding artifacts in bSSFP sequences. The top provides an illustration of the two positions of the magnetization projected onto the transversal plane. The two positions for flip angles with alternating phases are presented in the on-resonant case on the top left. The top middle shows both positions for an off-resonance that leads to a precession angle ω within one TR. The top right illustrates that the two states are not valid for off-resonances of π rad. The bottom left plots the steady-state signal of a bSSFP with flip angle 45°, TR/TE=4.5/2.25 ms, T_{RF}= 1 ms and BWTP=4. The marked areas present the signal drop, which causes banding artifacts. The bottom right shows a cardiac frame with banding artifacts in regions associated with fat. Figure modified from [13].

Influence of ΔB_0 on IR-bSSFP Fitting To investigate the influence of ΔB_0 on relaxation parameters, which are determined by analytical fitting of a IR-bSSFP signal, ΔB_0 reference values are extracted from an actual in vivo experiment. The map is acquired with two gradient recalled echo (GRE) sequences with different TE and post-processed

[1]The signal can increase in spikes for low flip angles [117].

following Section 2.2.1. From the resulting ΔB_0 map, the mean value of three representative ROIs is calculated covering the whole range of occurring ΔB_0 values. Afterwards, simulations of IR-bSSFP sequences are performed for each ΔB_0. The shared sequence parameters are TR/TE=4.5/2.25 ms, 1000 repetitions, 45° flip angle and a BWTP of 4. The relaxation values are set to human white matter at 3 T: T_1/T_2=0.834/0.08 s [102]. The absolute signal curves are visualized next to the ROIs in the in vivo ΔB_0 map in Figure 5.5.

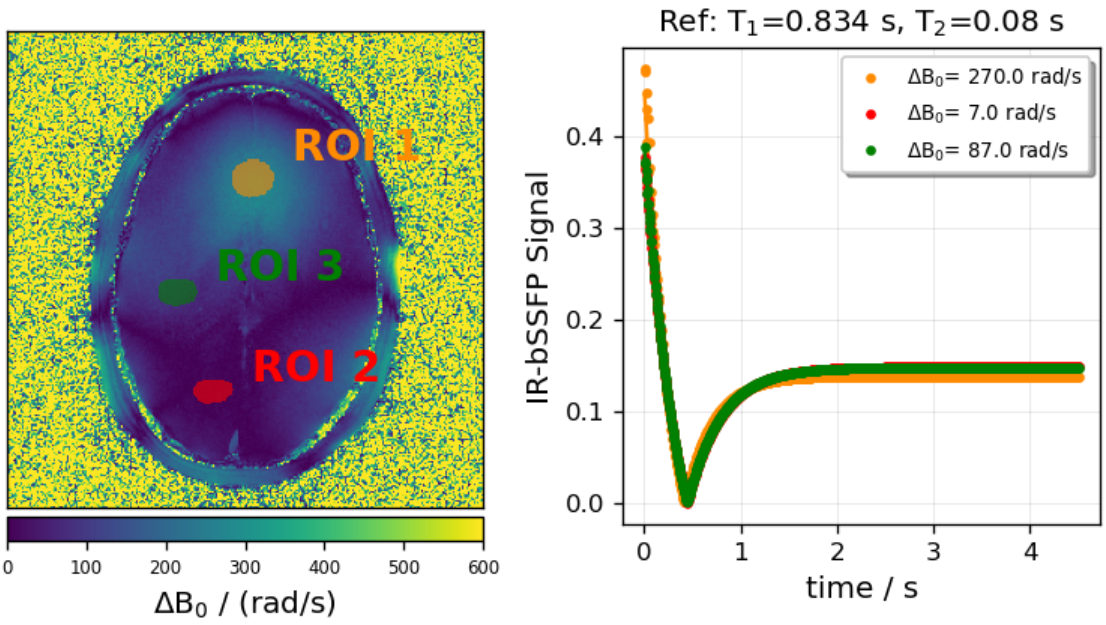

Figure 5.5: Investigation into the influence of off-resonances on the signal evolution of an IR-bSSFP sequence. The left presents a ΔB_0 map of a volunteer's brain. It includes colored ROIs, which are analyzed for their mean ΔB_0 values. The right presents signal simulations of representative white matter with T_1=0.834 s and T_2=0.08 s and the extracted mean off-resonances. The signals are fitted with an analytical IR-bSSFP model and the corresponding signal curves are plotted. The fitted parameters are listed in Table 5.1.

The signals are fitted with an analytical IR-bSSFP model, which is shown in Equation (4.31). The underlying physical tissue characteristics are determined from Equations (4.32) and follow with

$$
\begin{aligned}
T_1 &= T_1^* \frac{M_0}{M_{ss}} \cos\left(\frac{\alpha}{2}\right), \\
T_2 &= T_1^* \sin^2\left(\frac{\alpha}{2}\right)\left[1 - \frac{M_{ss}}{M_0}\cos\left(\frac{\alpha}{2}\right)\right], \quad \text{and} \\
M_0 &= \frac{M_0}{\sin\left(\frac{\alpha}{2}\right)} .
\end{aligned} \tag{5.4}
$$

The fitting errors for σ_{M_0}, $\sigma_{M_{ss}}$ and $\sigma_{R_1^*}$ are calculated from the covariance matrix. They are propagated to σ_{T_1}, σ_{T_2} and σ_{M_0} using the Gaussian error propagation:

$$
\sigma_{T_1} = \sqrt{\sigma_{T_1^*}^2 \left(\frac{M_0}{M_{ss}}\cos\left(\frac{\alpha}{2}\right)\right)^2 + \sigma_{M_0}^2 \left(\frac{T_1^*}{M_{ss}}\cos\left(\frac{\alpha}{2}\right)\right)^2 + \sigma_{M_{ss}}^2 \left(-\frac{M_0 T_1^*}{M_{ss}^2}\cos\left(\frac{\alpha}{2}\right)\right)^2}, \tag{5.5}
$$

$$
\sigma_{T_2} = \sqrt{\sigma_{T_1^*}^2 \left(\frac{\sin^2\left(\frac{\alpha}{2}\right)}{1-\frac{M_{ss}}{M_0}\cos\left(\frac{\alpha}{2}\right)}\right)^2 + \sigma_{M_0}^2 \left(-\frac{T_1^* \sin^2\left(\frac{\alpha}{2}\right)\left[\frac{M_{ss}}{M_0^2}\cos\left(\frac{\alpha}{2}\right)\right]}{\left[1-\frac{M_{ss}}{M_0}\cos\left(\frac{\alpha}{2}\right)\right]^2}\right)^2 + \sigma_{M_{ss}}^2 \left(-\frac{T_1^* \sin^2\left(\frac{\alpha}{2}\right)\left[-\frac{\cos\left(\frac{\alpha}{2}\right)}{M_0}\right]}{\left[1-\frac{M_{ss}}{M_0}\cos\left(\frac{\alpha}{2}\right)\right]^2}\right)^2}, \tag{5.6}
$$

and

$$
\sigma_{M_0} = \frac{\sigma_{M_0}}{\sin\left(\frac{\alpha}{2}\right)} . \tag{5.7}
$$

The nominal flip angle α was corrected by B_1 variations within the slice of the brain that was measured with a preconditioned RF pulse sequence following Section 2.2.1. The fitted parameters and errors are listed in Table 5.1.

Table 5.1: Fitting results of the simulated white matter with IR-bSSFP sequence, including off-resonances extracted from the in vivo brain slice. The corresponding plots are presented in Figure 5.5.

ω [rad/s]	T_1 [s]	T_2 [s]	M_0 [a.u.]
7.0	0.834±0.001	0.08±0.001	1.0±0.001
87.0	0.837±0.001	0.078±0.001	1.017±0.001
270.0	0.863±0.004	0.058±0.001	1.183±0.003

While for a small ω of 7 rad/s the fitting result shows the same relaxation parameters as the underlying reference values, an increase in ω leads to higher T_1 and decreased T_2 results.

Bloch Model-Based Correction of ΔB_0 After estimating the influence of the field inhomogeneities ΔB_0 on the fitting of IR-bSSFP data, the Bloch model-based reconstruction

technique is extended to include a ΔB_0 correction. The inhomogeneities are determined with two GRE acquisitions with different TE. ΔB_0 is calculated following Section 2.2.1. Similarly to the B_1 map, the ΔB_0 map is passed to the reconstruction pixel-wisely as prior knowledge. As the Bloch simulation in the forward model is based on the rotating frame, ΔB_0 is modelled as off-resonance in each voxel following Equation 5.3.

The reconstruction with and without additional ΔB_0 correction is presented in Figure 5.6 on the left, while the differences between both parameter maps are visualized on the right.

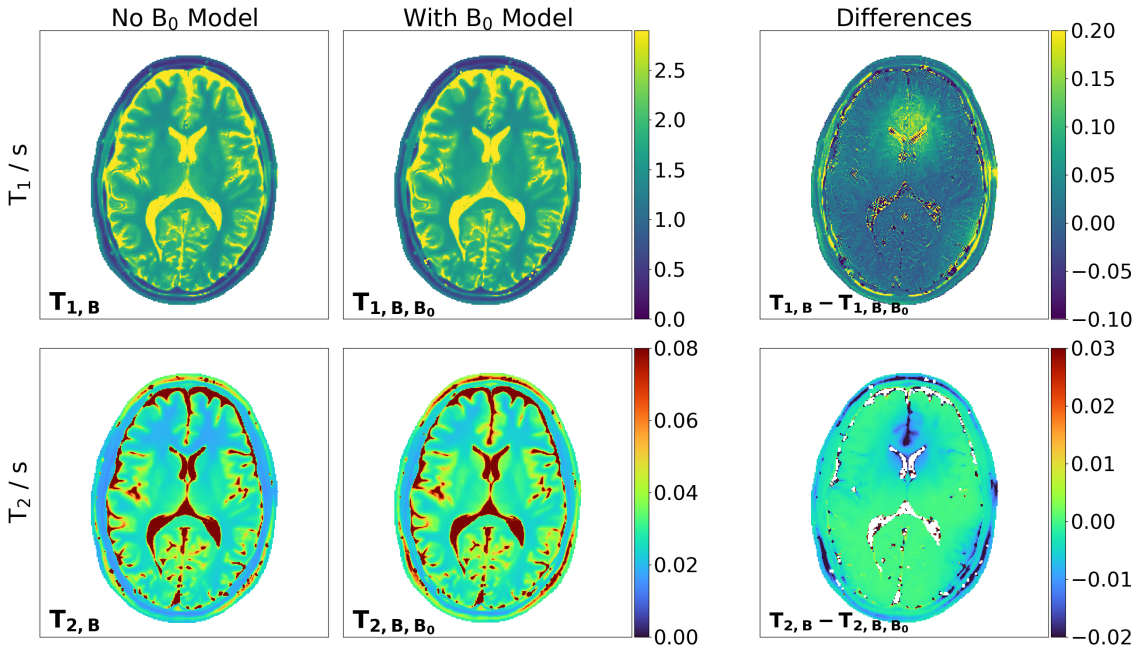

Figure 5.6: Influence of B_0 inhomogeneities on a Bloch model-based reconstruction of single-shot IR-bSSFP data. The left presents the T_1 and T_2 maps calculated with and without additional B_0 correction. On the right, their difference maps are shown.

When the difference maps are compared to the underlying ΔB_0 map, which is presented in Figure 5.5 on the left, the strong influence of the accuracy of the parameter mapping with respect to ΔB_0 can be observed. Correcting the model with the inhomogeneity map decreased the T_1 values and increased T_2 in areas showing high ΔB_0 values. In the future, more detailed studies should compare these off-resonance dependencies with their analytical special cases, which were derived by Ganter in 2004 [118] and the numerical study for IR-bSSFP sequences by Pfister in 2019 [116]. Future studies should also focus on sequences that are more robust to off-resonance effects [12].

5.4. Effects of Prior Shimming

In the previous section, the influences of B_0 inhomogeneities on the accuracy of reconstructed relaxation parameter maps from IR-bSSFP data are discussed. Due to the strong effects of ΔB_0 on many sequences, typical MRI protocols use automatic shimming procedures before the measurements. The execution of these corrections depends on the chosen shim type, the chosen accuracy, and the positioning of the shim volume. Shimming can drive the magnetization out of equilibrium and can modify the transient state of an IR-bSSFP sequence. If this effect is not modelled correctly, the accuracy of the determined parameter maps is reduced. Accurate modelling requires control over the exact time between shimming and data acquisition, which is not possible on the used MAGNETOM Skyra and Vida MRI scanners of this work. An alternative offers a temporal break between shimming and IR-bSSFP acquisition. It can ensure a relaxation to the equilibrium before the start of measurement.
In this section, the influence of prior shimming and relaxation breaks on the parameter quantification with an IR-bSSFP sequence is investigated. Two cases are compared, without shimming procedure and with shimming directly before the data acquisition.

Theoretical Background of Shimming MRI requires a homogeneous magnetic field $\Delta \boldsymbol{B} = 0$. In clinical scanner setups the x- and y-component of $\boldsymbol{B}$ are small compared to z, which leads to a reduction of the goal of shimming to

$$\Delta B_z = 0\,, \tag{5.8}$$

for a heterogeneous object placed in the scanner's magnetic field. Heterogeneity in the measured materials leads to varying magnetic susceptibilities χ that modify the magnetic field $\boldsymbol{B}$ according to Equation (5.3).

Two different classes of shimming were developed: Passive shimming exploits the different χ of materials, modifies $\boldsymbol{B}$ in a static but controlled way and compensates field inhomogeneities. Techniques range from ferromagnetic materials installed in the bore during the setup of the scanner system up to diamagnetic intraoral shims placed in the mouth during acquisitions [119]. Active shims on the other hand are created with wires placed around the measured object. This can be close to the measured objects as external system, integrated into the magnet as superconductive arrays or placed within the bore but outside the helium cooled area. Active shims are based on the idea of modifying $\boldsymbol{B}_0$ with magnetic fields that are created from current running through the additional wires. To understand the basic concept, the cylindrical symmetry of the magnet gives rise to a

description of $\boldsymbol{B}_0$ as spherical harmonics [120],

$$B_z(r,\theta,\phi) = \sum_{n=0}^{\infty} \sum_{m=-n}^{n} A_{nm} r^n P_n^m(\theta,\phi) \,, \tag{5.9}$$

with the spherical harmonics $P_n^m(\theta,\phi)$ weighted by the factors A_{nm}. Shim coils aim for creating the same harmonics as produced by the inhomogeneities, but with opposite sign for compensation. Clinically, $B_z(r,\theta,\phi)$ is approximated up to an order of two or three with specially designed coils [121]. For example, the used MAGNETOM Vida Scanner in this work provides three first order and five second order active shimming channels. Shim coils can be designed to show a perfect harmonic response, which is the foundation of projection-based shimming techniques. They calculate the weighting factors A_{nm} from diagonal projections along the surfaces of the shim volume [122, 123]. These techniques can work with small amounts of acquired data and are efficient and fast. Although in practice, shim coils generally do not have a perfectly harmonic response, which reduces the accuracy of projection-based methods. Volume-based shimming does not require a theoretically perfect harmonic coil system. It determines ΔB_0 maps from low resolution GRE images with different TE [124, 125] similar to the $\boldsymbol{B}_0$ mapping method that was introduced in Section 2.2.1. With provided reference scans performed on a homogeneous phantom $\boldsymbol{B}_0^{\text{ref}}$, the optimal currents $\boldsymbol{I}$ are found as a solution to the least-squares optimization [120]:

$$\hat{\boldsymbol{I}} = \underset{\boldsymbol{I}}{\operatorname{argmin}} \| \boldsymbol{B}_0^{\text{ref}}(\boldsymbol{r})\boldsymbol{I} - \Delta B_0(\boldsymbol{r}) \|_2^2 \,. \tag{5.10}$$

The currents determined on the homogeneous reference phantom during the setup of the scanner $\boldsymbol{I}^{\text{ref}}$ can be chosen as correction on Siemens systems. The corresponding shim mode is called *Tune-Up*. Siemens scanners provide further modes like *Standard* and *Advanced*, which are defined by the number of optimization steps and by the tolerated error of the shimming optimization (Equation (5.10)).

Methods In this work, the shim mode *Advanced* is the default in all acquisitions. The shimming is performed automatically prior to every first measurement with a new shim volume. In the studies of this work, the default shim volumes are the measured slices themselves. Two acquisitions on an in vivo brain are performed with a single-shot IR-bSSFP sequence. Both run the same shim currents $\boldsymbol{I}$ and have the sequence parameters TR/TE = 4.5/2.25 ms, 1000 acquired spokes, 45° nominal flip angle, T_{RF}=1 ms and BWTP=4. The shimming procedure runs only at the beginning of one acquisition without any waiting time until the start of the IR-bSSFP sequence. The reconstructions are performed

with the Bloch model-based reconstruction and the same assumptions for the forward model and the same optimization settings. The nominal flip angle is corrected pixel-wisely with an external B_1 map acquired with a preconditioned RF pulse sequence, as introduced in Section 2.2.1.

Results The resulting T_1 and T_2 parameter maps, which were reconstructed with the Bloch model-based technique, are presented in Figure 5.7 on the left. On the right, the differences between the same parameter maps acquired with and without prior shimming are presented. The shimming leads to decreased T_1 values, which strength correlates with the T_1 relaxation time of the tissue. Longer relaxation times are influenced more strongly. The T_2 map is less affected than T_1.

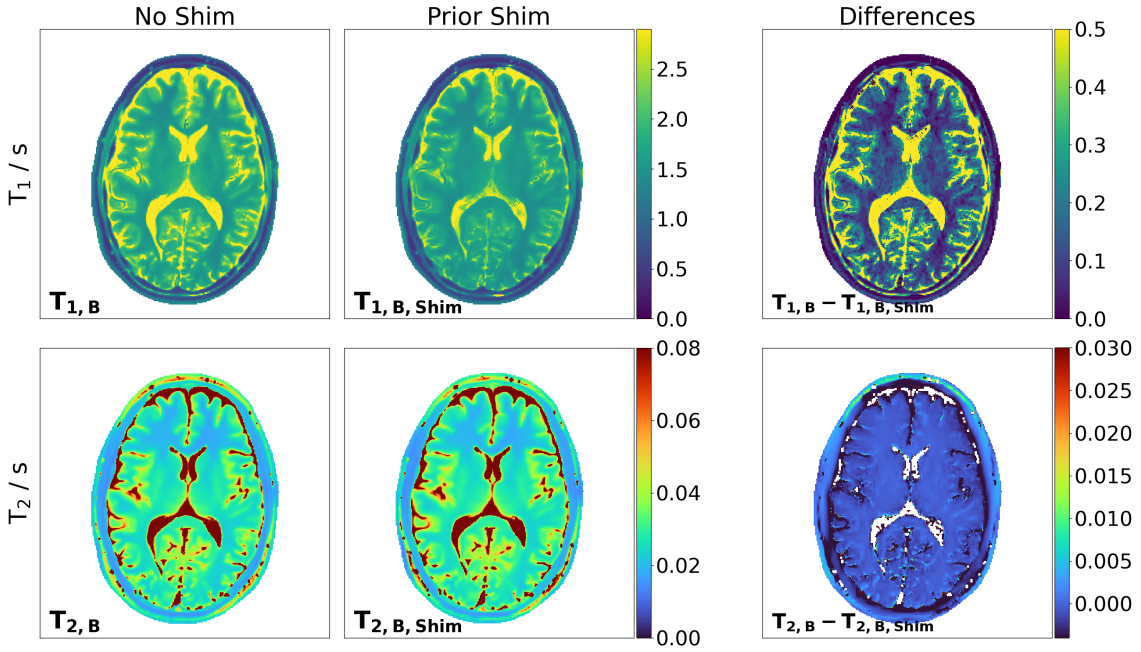

Figure 5.7: Influence of shimming on a Bloch model-based reconstruction of single-shot IR-bSSFP data. Two reconstructions of T_1 and T_2 maps from datasets with and without prior shimming are presented on the left. The right shows their differences.

Discussion Due to the fact that shimming requires the acquisition of low resolution GRE images, it involves RF pulses that excite the magnetization and move it away from its equilibrium. By omitting a temporal break between shim procedure and image acquisition, sequences based on a transient states, like the IR-bSSFP, follow a modified magnetization evolution. The incompletely recovered magnetization affects the transient state similarly

to a decreased inversion efficiency. The prior shimming influences tissues with longer relaxation times more strongly because their magnetization requires more time to relax back to its equilibrium.

5.5. Influences of Gradient Delays

After discussing additional physical effects on the level of individual voxels like ΔB_0 or skipped relaxation breaks between acquisition and shimming, this section has a focus on inaccuracies in the sampling trajectory. The most prominent error source here are gradient delays, which result from eddy currents. They change the sampling trajectory and break the data consistency in the optimization. In this section, the influence of such delays on the parameters that were reconstructed from in vivo single-shot IR-bSSFP data is investigated.

Theoretical Background of Gradient Delays Sampling trajectories are defined by local changes of the magnetic field due to spatial gradients and RF pulses, which are introduced in Section 2.1.7. In practice, these gradients need to be ramped up and down within a few hundred microseconds, which leads to currents of multiple hundred amperes in the corresponding coils. The resulting rapid change in current creates temporary varying magnetic fields and can induce eddy currents in surrounding electronic hardware parts [126, 127]. If this affects the gradient system itself, the waveform of their response is changed and deviations from the actual sampling trajectory occur [128]. This effect varies for different sampling schemes. Cartesian imaging is characterized by the same gradient waveform that is used for every readout. Therefore, gradient delays affect every readout in the same way, thus creating a constant phase offset in the reconstructed images. Spiral imaging has single trajectories that span the whole k-space. Here, gradient delays have a different effect on each sampling point, which makes corrections challenging [34]. The focus of this work is on radial imaging. Gradient delays affect each sampling point along a spoke similarly. This can be described as a superposition of a parallel and orthogonal shift with respect to the readout direction. The shifts can be measured during each acquisition with dedicated hardware to correct for these deviations [129, 130]. Another generic correction estimates the gradient system impulse response function (GIRF) of the scanner system in prior calibration scans and corrects each gradient waveform with it [131, 132]. Both methods might be superior for correcting complex spiral trajectories, but they can be challenging to implement and require expensive hardware. Radial trajectories can be corrected more easily, even on the acquired dataset itself without additional hardware

or calibration scans. One technique has been developed by Block and Uecker in 2011 [133]. It derives the parallel shift component based on sampled spokes from opposite angles. A method developed by Rosenzweig in 2018 [134], called radial spoke intersections for gradient delay estimation (RING), determines both the parallel and orthogonal component of the gradient delay effect. It takes multiple spokes and fits an ellipse to intersecting readout samples. Afterwards, the shifting operators that transform the ellipse back to a unit circle are calculated. They uniquely define a correction of the gradient delay effects from only a few spokes. This technique can also be applied to other sampling trajectories with radial behavior for low frequencies, like for rosette patterns [135].

Experimental Setup In this analysis, an in vivo brain from a healthy volunteer is measured with a single-shot IR-bSSFP sequence. The sequence parameters are TR/TE=4.5/2.25 ms, 1000 acquired spokes, 7th tiny golden angle, 45° nominal flip angle, T_{RF}=1 ms and BWTP=4. For the correction of the nominal flip angle, an external B_1 map is acquired with a preconditioned RF pulse sequence. The reconstructions are performed with the Bloch model-based technique, which includes a slice profile simulation that is based on the known slice-selection gradient strength. The nominal flip angle is corrected pixel-wisely with the acquired B_1 map. Two reconstructions are performed with and without RING-corrected sampling trajectories. The relative gradient delay difference between both experiments is one sample in parallel and orthogonal direction.

Results & Discussion The results of the reconstructed T_1 and T_2 parameter maps are presented on the left of in Figure 5.8. On the right, the differences between the individual maps are shown. The reconstruction without correction of gradient delay effects shows many checkerboard artifacts, especially in and close to regions associated with flow. That indicates that the data consistency is violated because the sampled positions in the forward model do not match the measured frequencies. If the discrepancy is removed with a RING-based correction, fewer regions with checkerboard effects occur in the reconstruction. The strongest influences of gradient delay effects is observed in the T_1 map. The delays introduce errors especially in the outer parts of the brain with complex geometries and potential flow effects.

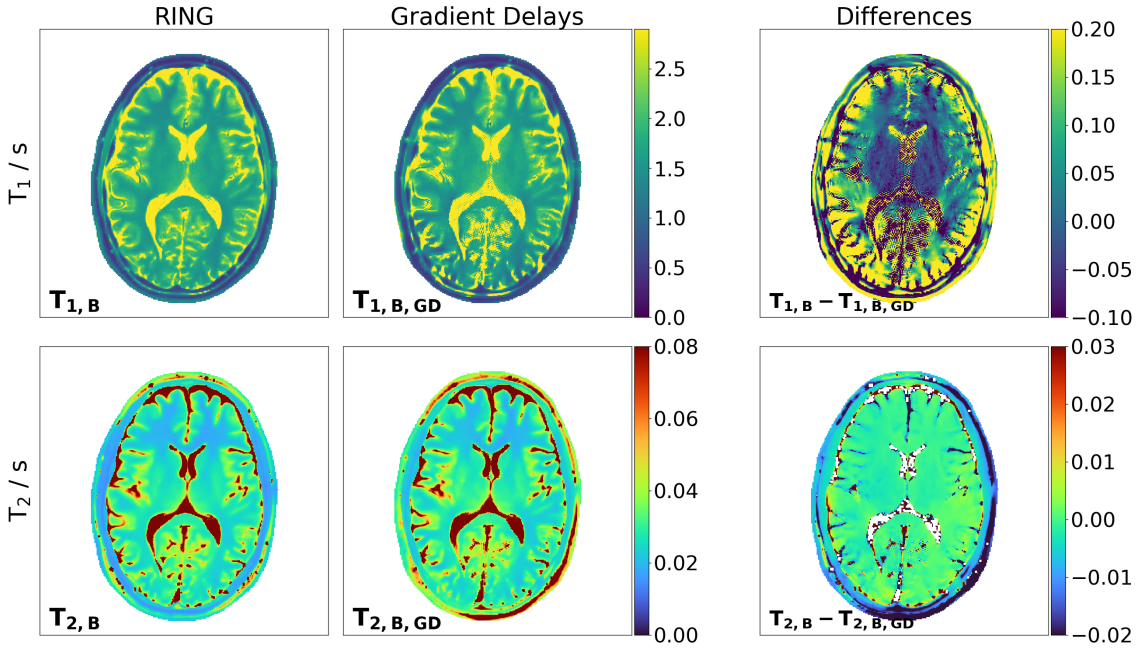

Figure 5.8: Influence of gradient delays on a Bloch model-based reconstruction of single-shot IR-bSSFP data. Two reconstructions of T_1 and T_2 maps from datasets with and without gradient delay correction based on RING are presented on the left. On the right, the difference maps are presented.

5.6. Pixel-Wise Perspective on the In Vivo IR-bSSFP Offset

Up to now, various influences on the accuracy of the parameter quantification are discussed. None leads to large enough differences that can explain the observed offset in the in vivo IR-bSSFP analysis shown in Figure 4.6. In this section, an additional validation step is performed that compares the Bloch model-based reconstruction to a pixel-wise fitting technique based on real-time regularized nonlinear inverse reconstruction (RT-NLINV) [14]. This analysis aims to provide additional understanding about the accuracy of the optimization.

Theoretical Background of RT-NLINV The basis for RT-NLINV [14] is regularized nonlinear inverse reconstruction (NLINV), which is introduced in Section 2.1.9. RT-NLINV provides additional causal temporal regularization terms,

$$(\hat{\boldsymbol{\rho}}_t, \hat{\boldsymbol{c}}_t) = \underset{(\boldsymbol{\rho}_t, \boldsymbol{c}_t)}{\operatorname{argmin}} \|\mathcal{P}\mathcal{F}\mathcal{C}(\boldsymbol{c}_t, \boldsymbol{\rho}_t) - \boldsymbol{y}\|_2^2 + \alpha \left[\|\boldsymbol{\rho}_t - \tau \boldsymbol{\rho}_{t-1}\|_2^2 + \|\boldsymbol{W}(\boldsymbol{c}_t - \tau \boldsymbol{c}_{t-1})\|_2^2 \right] , \quad (5.11)$$

and the weighting

$$\boldsymbol{W} = \begin{pmatrix} \left(1 + s\|\boldsymbol{k}\|^2\right)^{l/2} \mathcal{F} & & \\ & \ddots & \\ & & \left(1 + s\|\boldsymbol{k}\|^2\right)^{l/2} \mathcal{F} \end{pmatrix}, \tag{5.12}$$

the scaling s=220 and l=32 as well as a temporal damping factor of τ=0.9. The difference between the current solution $(\boldsymbol{\rho}_t, \boldsymbol{c}_t)$ and its predecessor $(\boldsymbol{\rho}_{t-1}, \boldsymbol{c}_{t-1})$ is penalized with a l_2 norm. This enforces similarity between consecutive frames in time and adds prior knowledge to the reconstruction of $(\boldsymbol{\rho}_t, \boldsymbol{c}_t)$, which allows for a further reduction of the required data.

Methods For this analysis, an in vivo brain from a healthy volunteer is measured with a single-shot IR-bSSFP sequence. The sequence parameters are TR/TE=4.5/2.25 ms, 1000 acquired spokes, 7th tiny golden angle, 45° nominal flip angle, T_{RF}=1 ms and BWTP=4. To correct the nominal flip angle, an external B_1 map is acquired with a preconditioned RF pulse sequence from the same slice. The reconstructions with RT-NLINV are performed on datasets on which five temporal consecutive spokes have been joined to one frame. The optimization is performed frame-by-frame starting from the last acquired frame. This exploits the smooth transitions of the contrast close to the steady-state of the bSSFP acquisition. The order reversed in time ensures that more accurate prior knowledge is added to the reconstruction close the inversion pulse. It is crucial for an accurate fitting of the signal because these steps encode the most T_1 information. After frame-wise reconstruction, two ROIs are defined and their signals with their standard deviations are extracted. Both are fitted with the analytical signal model for an IR-bSSFP sequence, as presented in Equation (4.32). The relaxation parameters are calculated following Equation (5.4) together with their errors defined by the Equations (5.5), (5.6) and (5.7). Afterwards, two Bloch model-based reconstructions of the same data are performed. One incorporates a complex signal model with slice profile and hyperbolic secant (HS1) inversion pulse and the other assumes hard pulses to approximate the analytical fitting process performed on the RT-NLINV reconstructions. The relaxation values of both ROIs are extracted from the Bloch model-based reconstructions. The temporal evolution of the magnetization of the ROI's relaxation values is simulated and compared to the analytical fits.

Results The results are shown in Figure 5.9. On the left, the T_1 parameter map that has been reconstructed with the complex signal model is presented with the marked analyzed ROIs. In the left center of Figure 5.9, the T_1 map is shown that is reconstructed

with the simple signal model to include the same assumptions as for analytical model of an IR-bSSFP. The mean relaxation values for T_1 and T_2 are extracted from the marked ROIs and are added to Table 5.2 with standard deviations. On the right side of Figure 5.9, the mean signal of the two ROIs extracted from the RT-NLINV reconstructions with standard deviations is presented.

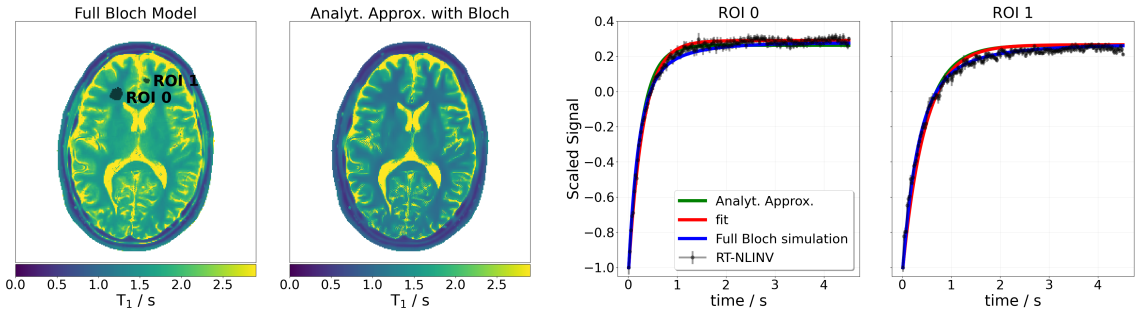

Figure 5.9: T_1 and T_2 maps reconstructed with the Bloch model-based technique under the assumption of a complex Bloch model (left) and its approximation of the analytical IR-bSSFP model (center left). ROIs mark the locations in which the T_1 and T_2 values are extracted from both maps. On the right, the simulated signals based on the extracted relaxation values are presented (blue, green). The temporal evolution of the marked ROIs during the individual frames of an RT-NLINV reconstruction of the data is added in black. Their errors represent the standard deviations in the ROIs in each frame. The red lines represent the synthetic signals from the analytical fit to the RT-NLINV reconstructions. The corresponding fitting results are listed in Table 5.2.

The RT-NLINV ROI selected signal is fitted with the analytical signal model of Equation (4.32). Both are plotted with the simulated signals that are based on the T_1 and T_2 relaxation values, which are extracted from both Bloch model-based reconstructions.

All simulated signal evolutions overlap with the extracted signal from the RT-NLINV reconstruction. The relaxation parameters reconstructed with the simple forward model are similar to the pixel-wise fits on the RT-NLINV signal.

Discussion Both reconstructed T_1 parameters are higher and both T_2 values are lower than the white matter reference values [102]. Following the analysis in Section S5, the difference can partially be explained by MT effects. The strongly overlapping signals indicate that the Bloch model-based reconstruction is able to find solutions that accurately fulfill the data consistency. This is the case for both the complex and the simple forward model. Including a realistic signal model with slice profile simulation and finite RF pulses leads to an increase in the T_1 values and to a decrease in the T_2 parameters. Both are in the

Table 5.2: T_1 and T_2 values calculated from the ROIs in Figure 5.9 for both reconstructions with complex Bloch model and its approximation of the analytical IR-bSSFP signal. Additionally, the results of the analytical model fitted to the RT-NLINV reconstructions are added. The error of the Bloch reconstructions follows the standard deviation in the ROIs. The error of the fitting follows from the fitting covariance and propagates according to Equations (5.5), (5.6) and (5.7).

		T_1 [s]	T_2 [s]
ROI 0	Full Model (Bloch)	1.45±0.025	0.019±0.001
	Analy. Approx. (Bloch)	1.047±0.019	0.037±0.002
	Analytical Fit	1.034±0.017	0.045±0.001
ROI 1	Full Model (Bloch)	2.063±0.076	0.028±0.001
	Analy. Approx. (Bloch)	1.687±0.054	0.058±0.007
	Analytical Fit	1.699±0.028	0.062±0.001

range of the in vivo IR-bSSFP offset. Nevertheless, incorporating these additional physical effects should not move the solution further away from the physical references. This holds especially as the phantom studies (Figure 4.5) with an IR-bSSFP sequence indicated better accuracies for more realistically simulated models.
Overall, this analysis suggests that the optimization works well for various signal model assumptions. It indicates that the offset is related to the actual physical model used in the Bloch model-based reconstruction rather than the optimization settings.

5.7. Influence of Spoke Binning

In the RT-NLINV analysis, five consecutive spokes are binned to a single frame to be reconstructed together. This averages their individual contrast and their encoded physical effects. Choosing a too large number of binned spokes reduces the temporal resolution and can lead to undesired averaging of fast physical behavior. Spoke binning is used in the Bloch model-based reconstruction to reduce the computational complexity of solving the linearized problem in each Gauss-Newton step, as described in Equation (4.20). Because (4.20) is solved with fast iterative shrinkage/thresholding algorithm (FISTA), the normal operator

$$\mathcal{N}(\boldsymbol{x}_n) = D\mathcal{A}^H(\boldsymbol{x}_n) D\mathcal{A}(\boldsymbol{x}_n)\,, \tag{5.13}$$

with

$$D\mathcal{A}(\boldsymbol{x}_n) : \mathbb{C}^{B\times B\times P} \mapsto \mathbb{C}^{N\times S\times C\times T} \tag{5.14}$$

is required in each iteration. Here, $(\cdot)^H$ is the adjoint, B the base resolution, P the parameters, N the number of samples in k-space, S the number of radial spokes, C the coil sensitivities and T the time steps.
While $\mathcal{N}$ can be pre-computed, it requires storing a large matrix and does not allow for exploiting a fast (discrete) Fourier transform (FFT). To reduce the computational costs, $\mathcal{N}$ is designed as an operator and can therefore incorporate an FFT, but needs to be applied in every FISTA iteration. The current implementation of the non-uniform fast Fourier transform (nuFFT) exploits a Toeplitz trick for efficient computation of $\mathcal{F}^H\mathcal{P}^H\mathcal{P}\mathcal{F}$, but the numbers of applied FFT operations is still proportional to T. By joining consecutive spokes, T is decreased and the computational demands for calculating $\mathcal{N}$ are reduced. This binning of spokes requires the balancing of the number of joined data with the time scale on which the modelled physical effects appear. Otherwise, undesired averaging introduces a physical bias. A detailed analysis of this phenomenon for reconstructions of IR-FLASH sequences has been performed by Roeloffs in 2016 [43]. In this study, the influence of spoke binning on the Bloch model-based reconstruction of single-shot in vivo IR-bSSFP data is investigated.

Methods An in vivo brain from a healthy volunteer is measured with a single-shot IR-bSSFP sequence. The sequence parameters are TR/TE=4.5/2.25 ms, 1000 acquired spokes, 7th tiny golden angle, 45° nominal flip angle, T_{RF} is 1 ms and BWTP is 4. To correct the nominal flip angle, an external B_1 map is acquired with a preconditioned RF pulse. Two reconstructions are performed with the Bloch model-based technique including a temporal binning of 15 spokes and no binning at all. The binning is implemented in the Bloch simulation as averaging over multiple simulated echoes. The nominal flip angle in both reconstructions is corrected pixel-wisely with the additional B_1 map.

Results The results are shown in Figure 5.10. On the left, the individual parameter maps for T_1 and T_2 are presented, while the difference maps are presented on the right.

Discussion For the Bloch model-based reconstruction, the speedup through spoke binning only affects the solving of the linearized problem. Other model-based techniques that are based on analytical functions [9, 10] can also benefit from the reduced computational efforts during execution of the forward operator. The relaxation parameter maps

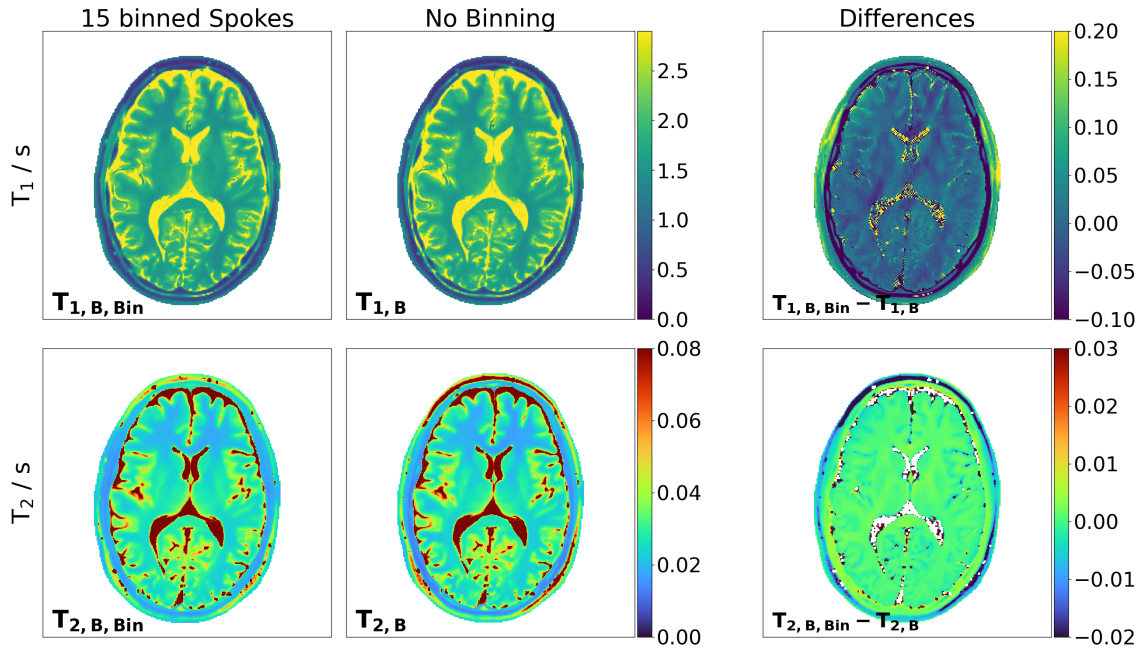

Figure 5.10: Influence of spoke binning on the Bloch model-based reconstruction of single-shot IR-bSSFP data. Two reconstructions of T_1 and T_2 maps from datasets with and without 15 binned spokes are presented on the left. On the right, the difference maps are shown.

reconstructed with both settings are similar. The T_1 map shows errors up to 50 ms, which might arise from a different regularization. This can result from a different initial scaling of the dataset, similar to the analysis in Section 5.2. Because the IR-bSSFP sequence is more sensitive for changes in T_1 than in T_2, the effect is stronger in T_1. Nevertheless, a relative error comparison as well as an additional physical and numerical phantom study would be interesting.

5.8. Flip Angle Effects

The quantitative mapping accuracy with IR-bSSFP sequences is sensitive to flip angle variations. For low angles (>30°) the transverse component of the magnetization vanishes. This reduces the sensitivity of the sequence with respect to T_2 and the effective relaxation rate R_1^* becomes close to R_1. Higher flip angles (>90°) increase R_1^*, which reduces the time until the steady-state is reached and constraints the reconstruction to a high temporal resolution. This forced previous work [3] to use flip angles between 30° and 90° in order to determine accurate quantitative maps. Model-based reconstructions provide a high temporal resolution with each single repetition modelled individually, which can resolve

fast physical dynamics. Nevertheless, large flip angles result in a high specific absorption rate (SAR) and the application of spoke binning is also more limited. Therefore, flip angles of 45° are exploited in previous sections. To validate the assumption, it is investigated in this analysis which influence varying flip angles of IR-bSSFP acquisitions have on the reconstructed parameter maps.

Methods All datasets of this analysis are acquired on a brain of a healthy volunteer. A single-shot IR-bSSFP sequence is used with the parameters TR/TE = 4.5/2.25 ms, 1000 acquired spokes, 13th tiny golden angle, T_{RF}=1 ms and BWTP=4. The nominal flip angles are set to 20, 40, 45, 50, 60, 70, 77°. To correct the nominal flip angle in IR-bSSFP, an external B_1 map is acquired with a preconditioned RF pulse sequence. A reference single-shot IR-FLASH sequence is measured on the same slice with the settings TR/TE=3.8/2.26 ms, 1000 acquired spokes, 13th tiny golden angle, 8° flip angle, T_{RF}=1 ms and BWTP=4. All reconstructions are performed with the Bloch model-based reconstruction including a slice profile simulation that is based on the known slice-selection gradient strength. The nominal flip angle is corrected pixel-wisely with the B_1 map additionally acquired for the IR-bSSFP datasets. The T_1 and T_2 values of representative ROIs for white matter and gray matter are extracted from each IR-bSSFP reconstruction and plotted against the nominal flip angle. Their correlation is linearly fitted with

$$T_1(\text{flip angle}) = m \cdot \text{flip angle} + b \ . \tag{5.15}$$

The results with their corresponding errors are listed in Table 5.3.

Table 5.3: Fitting results of the variable flip angle IR-bSSFP analysis for two different ROIs. The data corresponds to the fits that are visualized in Figure 5.11.

	#ROI	m [s/deg]	b [s]
T_1	1	0.01±0.001	0.984±0.016
	2	0.008±0.001	1.794±0.013
T_2	1	0.0003±2e-05	0.011±0.001
	2	0.00026±4e-05	0.023±0.003

Results The results for the variable flip angle analysis are visualized in Figure 5.11. The relaxation values for T_1 and T_2, which are extracted from the ROIs, increase linearly with the flip angle. Lower flip angles lead to T_1 values closer to and T_2 values further away from the reference.

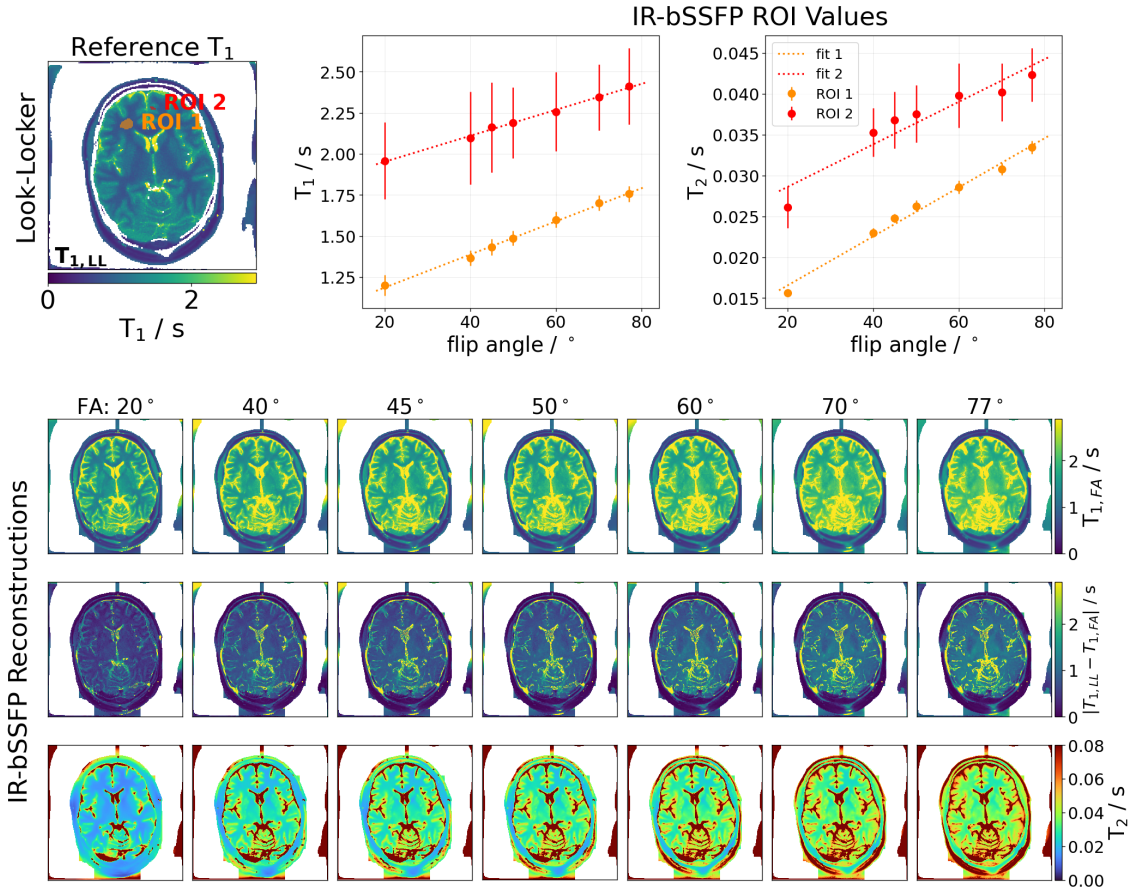

Figure 5.11: On the top left, a reference T_1 map determined from an IR-FLASH acquisition is presented. The two ROIs that are used for extracting T_1 and T_2 values are marked in the frames on the bottom. On the bottom, multiple T_1 (bottom top), T_2 (bottom bottom) and difference maps (bottom center) are presented that were reconstructed with the Bloch model-based technique from IR-bSSFP data for varying nominal flip angles (increasing column-wise to the right). The difference maps refer to the reference Look-Locker T_1 map. On the top right of the figure, the results for the mean T_1 and T_2 values are shown that are extracted from the IR-bSSFP reconstructions. These ROI analysis results are fitted linearly with Equation (5.15). The determined parameters are listed in Table 5.3.

Discussion With a higher flip angle, the MT influence on the parameter maps increases. This can lead to higher T_1 values and reduced T_2. Because the latter actually increases, the differences through varying flip angles can not be explained by MT. The decreasing T_1 and T_2 for lower flip angles ($< 30°$) are expected. They result from the IR-bSSFP sequence's ability to become only sensitive to T_1 in this flip angle range. One potential influence of the increasing relaxation values can lay in the regularization differences. Different flip

angles change the transient magnetization contributing to the measured signal, but also leading to different steady-states. This effect, combined with the initial data scaling for improved robustness, can change the regularization of the individual parameter maps and can influence the convergence and the potential solution. Nevertheless, the similar effect in Section 5.2 does not indicate that the effect is expected to be strong. In future studies, this analysis should be repeated numerically and on a physical phantom to reduce the amount of potential dependencies on the acquisition.

6. Summary and Outlook

In this thesis, a generic tool for quantitative multi-parameter mapping has been developed. It combines a new efficient Bloch simulation based on state-transition matrices (STM), a numerically stable sensitivity analysis of the Bloch equations (SAB) for generic and accurate calculation of the partial derivatives of the signal, and a nonlinear model-based reconstruction framework.

In the first step, the individual parts of the Bloch model-based reconstruction technique were validated. Starting from the work of the previous proof-of-principle study [13], an in-depth analysis of the SAB has been performed. One key step was the comparison of partial derivatives with respect to T_1, T_2 and B_1 calculated with an analytical model, a difference quotient (DQ) and the SAB. The SAB showed no amplification of numerical noise and did not require manual tuning of perturbation limits in contrast to DQ. It outperformed DQ in precision and accuracy for all calculated derivatives.

The second validation addressed the computational costs of SAB in a Bloch model-based reconstruction. Especially when based on the Runge-Kutta (RK) 54 ordinary differential equation (ODE) solver, the estimation of the temporal evolution of the derivatives is accurate but rather slow. This becomes challenging for complex dynamics such as the modelling of strong off-resonances, which requires small step sizes to ensure high accuracy.

In this work, the speedup of the simulation and SAB was achieved by developing a new STM-based method. It was verified with slice profile simulations and its accuracy and computational speed were compared to a RK54 simulation and an asymmetric operator splitting (ASY) based rotation matrix (ROT) simulation. The STM reproduced the results of the RK54 as expected because both techniques exploit the same ODE solver. The ROT simulation showed a higher point-wise error compared to the STM in all experiments. The reason is the first order nature of the ASY ROT simulation with its accuracy increasing linearly with the number of steps until numerical noise dominates. In comparison to the ASY ROT, the underlying ODE solver for RK54 and STM is a fourth order technique, which provides higher accuracy for the same decrease in step size.
After comparing the accuracy of the simulation techniques, their computational cost was

investigated. The STM showed substantial efficiency gains for sequences with repeating patterns which occur in many typical magnetic resonance imaging (MRI) sequences such as inversion-recovery fast low angle shot (IR-FLASH) and inversion-recovery balanced steady-state free precession (IR-bSSFP). The crossover point where the computation of the state-transition matrices including the SAB has less computational costs compared to full simulations with a RK54 is expected to be at 13 repeating patterns. The limit drops to four when only the Bloch equations are solved and no SAB is included. In comparison to these theoretical expectations, the current analysis shows the crossover point to be at about 60, which indicates that the implementation of the STM can still be improved.

By combining the simulation of the Bloch equations and the SAB in the STM, the computational efficiency increased sufficiently to make an integration into a nonlinear model-based reconstruction framework feasible. The Bloch model-based tool was validated in a numerical and physical phantom as well as in an in vivo study. First, the technique was compared to a specialized reconstruction based on the analytical Look-Locker model for IR-FLASH sequences [9]. To ensure a comparable regularization of the determined physical quantities, the Look-Locker model was reparameterized. The Bloch model-based technique reproduced the results of its analytical special case in all studies. For this on-resonant simulations, the reconstruction speeds for both models were similar.

With the IR-FLASH sequence used for reproducing the special case of a Look-Locker model-based reconstruction, T_1 and a relative flip angle can be determined. The aim of this work was to realize a simultaneous mapping of multiple relaxation parameters. Therefore, a study with an IR-bSSFP sequence was performed. It provided the same sensitivities as an IR-FLASH but adds sensitivity to T_2. While T_1 and T_2 are coupled, prior knowledge about the effective flip angle was used to decouple both. Thus, both relaxation parameters can be determined simultaneously. In a first step, a numerical and physical phantom study was performed. The flexibility of the Bloch model-based method was demonstrated using different reconstructions with varying complexity of the signal model. The most complex model included a hyperbolic secant (HS1) inversion pulse with non-analytical magnetization evolution and a slice profile. The simultaneously mapped T_1 and T_2 values determined with the most complex model were accurate compared to a gold-standard references. They became less accurate the further the model moved away from the realistic physical model. Especially, the missing slice profile simulation decreased the T_2 accuracy substantially. This is expected because the slice profile significantly affects the effective flip angle, which needs to be known to decouple T_1 and T_2.

After validating the simultaneous T_1 and T_2 mapping with the Bloch model-based reconstruction in phantoms, another IR-bSSFP study was performed using in vivo data.

The most complex and realistic signal model was chosen as the default reconstruction because of its high accuracy in the phantom studies. Nevertheless, it could not accurately reproduce the expected T_1 values from a Look-Locker reference scan. The differences showed up as positive offsets in the T_1 and negative offsets in the T_2 values when being compared to the literature values. The offset could be reduced by using prolonged radio frequency (RF) pulses and a prolonged repetition time (TR), which hints at magnetization transfer (MT) as one potential source of the discrepancies. Following this idea, the error may result from a physical bias because the Bloch equations only model a single substance. As a result, the influence from macromolecules that interact with the measured free water was not modelled and this changed the reconstructed parameters. An additional study in Section S5 estimated the size of this effect with multiple IR-bSSFP measurements. It suggested that MT can explain about half of the observed offset in T_1. Consequently, the extension of the Bloch model to a two pool Bloch-McConnell model should be investigated in the future.

Further investigations concentrated on potential other sources of the still unexplained portion of the offset. First, changes in the optimization algorithm were tested. Here, the Bloch model-based reconstruction of in vivo IR-bSSFP data has been found to be robust for a wide range of initialization values. Tests with different parameter distributions indicated that the internal scaling that is based on the l_2 norm of the data makes the reconstruction sensitive to changes in the overall signal amplitude. This causes different effective regularization strengths that influence the accuracy of the calculated parameter maps.

In a second step, other effects that could lead to a physical bias were investigated. The main focus was on B_0 inhomogeneities. The influence of differences in B_0 was measured, simulated and analyzed. B_0 affected the estimated T_1 and T_2 values of white matter tissue. This can be taken into account by integration of a prior ΔB_0 reference map into the Bloch model-based reconstruction. A study on in vivo IR-bSSFP data showed slightly increased offsets, which is evidence that B_0 is not the source of the offset.

Following the idea that B_0 influences the reconstruction results, the effects from shimming of the B_0 field were investigated. This showed that the parameter maps are influenced when there is not enough time between the automatic shimming procedure and the start of the IR-bSSFP sequence. An additional break can be inserted between shimming and acquisition to avoid any influence on the IR-bSSFP acquisition, but it does not remove the remaining offset in the in vivo IR-bSSFP reconstructions.

The next investigated physical effects were gradient delays. They affected the parameter maps in outer regions of the brain more than in inner regions and increased checkerboard

artifacts in regions associated with flow. These delays could also not explain the constant offset for the used sampling patterns.
An additional analysis investigated a flip angle dependency of the offset. A linear behavior was found, but no flip angle combination could provide relaxation values close to the expected reference.
Overall, multiple physical effects were found to influence the accuracy of the reconstructed parameter maps, but none of them provided a complete explanation for the observed offset in the in vivo IR-bSSFP reconstructions.

Additional tests focused on the optimization procedure and related potential error sources. Tests with different amounts of averaged spokes could also not provide a sufficiently strong influence on the relaxation values to explain the offset.
The validity of the data consistency was also confirmed with a pixel-wise fit on real-time regularized nonlinear inverse reconstruction (RT-NLINV) results. Furthermore, the more realistic physical model can estimate the relaxation parameters accurately, as it was demonstrated in phantom studies. These findings rule out that a numerical issue during the optimization is the source of the error and indicate that the cause is of physical nature.

The reconstruction time of the Bloch model-based reconstruction is still long for complex signal dynamics despite the use of adaptive step-size controlled a ODE solver and STM simulations. A speedup can be achieved with an optimized implementation that adds GPU support. Additionally, the STM concept can be generalized. At the moment the state-transition matrixs (STMs) have to be calculated for many spins along a slice profile. Future studies should investigate if the STM can be computed more efficiently for multiple related spins by exploiting their relationship.

Moreover, the Bloch model-based reconstruction is sensitive to a large variety of different scaling factors. The internal scaling of the data influences the overall regularization strength for different parameter maps. Additionally, the preconditioning of the parameter maps affects the relative convergence. Currently, both require manual tuning and future work should investigate automatic preconditioning techniques based on simulations [109], eigenvalues [110], or Cramer-Rao bounds.

Besides these conceptional improvements, the major unsolved challenge of this work is the offset in the in vivo IR-bSSFP reconstructions. The MT effect can be modelled with an extension to the Bloch-McConnell equations. While this work could exclude various potential error sources, the variable flip angle analysis opens up interesting questions that require future investigation.

In general, the Bloch model-based reconstruction is a first step into the direction of a closer integration of reconstruction and acquisition. A future extension of this project could be the unification of the software that runs on the scanner and the one that defines the physical model in the quantitative reconstruction. This would ensure that the scanner and the simulation process the sequence in the same way. The integration of more complex signal models could then increase the number of estimated parameters. This requires special sequences that can be obtained by automatically optimizing their sensitivity to physical parameters, which would connect this framework with the field of sequence design.

Taken together, this work developed a generic calibration-less model-based reconstruction framework for multi-parameter quantitative mapping. With its flexibility to work with arbitrary sequences, this framework emerges as a versatile tool for the simultaneous measurement of various important physical quantities. It is my hope that this contribution will help to improve diagnostics, understanding, and reproducibility of quantitative magnetic resonance imaging (QMRI) results.

A. Appendix

A1. Windowed Sinc Integral

In this section the integral of a windowed sinc function,

$$B_1(t) = A\left[(1-\alpha) + \alpha\cos\left(\frac{\pi t}{N t_0}\right)\right]\operatorname{sinc}\left(\frac{\pi t}{t_0}\right), \tag{A.1}$$

is derived with its scaling A, the windowing parameter α (0 for no, 0.5 for Hanning- and 0.46 for Hamming-windowed sinc pulse), the maximum of left n_l and right n_r sidelobes $N = \max(n_l,n_r)$, the length of the main lobe $t_0 = \frac{T_{\mathrm{RF}}}{n_l+n_r}$, the pulse duration T_{RF} and the time t.

For simplification of the notation in the following steps $a = A(1-\alpha)$, $b = A\alpha$, $c = \frac{\pi}{N t_0}$ and $d = \frac{\pi}{t_0}$ are substituted in Equation A.1 that leads to

$$B_1(t) = a\operatorname{sinc}(dt) + \frac{b}{dt}\cos(ct)\sin(dt)\,. \tag{A.2}$$

With $\sin(x)\cos(y) = \frac{1}{2}(\sin(x-y)+\sin(x+y))$ Equation (A.2) can be reformulated to

$$\begin{aligned}
B_1(t) &= a\operatorname{sinc}(dt) + \frac{b}{2dt}(\sin(dt-ct)+\sin(dt+ct)), && \text{(A.3)}\\
&= a\operatorname{sinc}(dt) + \frac{b}{2dt}\sin([d-c]t) + \frac{b}{2dt}\sin([d+c]t), && \text{(A.4)}\\
&= a\operatorname{sinc}(dt) + \frac{b(d-c)}{2dt(d-c)}\sin([d-c]t) + \frac{b(d+c)}{2dt(d+c)}\sin([d+c]t), && \text{(A.5)}\\
&= a\operatorname{sinc}(dt) + \frac{b(d-c)}{2d}\operatorname{sinc}([d-c]t) + \frac{b(d+c)}{2d}\operatorname{sinc}([d+c]t)\,. && \text{(A.6)}
\end{aligned}$$

The derivation of the integral of $B_1(t)$ requires the definition of the sine integral

$$\mathrm{Si}(x) = \int_0^x \frac{\sin(t)}{t}\mathrm{d}t\,. \tag{A.7}$$

If combined with the substitution $t' = t + \frac{T_{\mathrm{RF}}}{2}$ and the chain rule, the integral can be

determined

$$I_{B_1} = \int_0^{T_{\mathrm{RF}}} a\,\mathrm{sinc}(dt')\mathrm{d}t' + \int_0^{T_{\mathrm{RF}}} \frac{b(d-c)}{2d}\,\mathrm{sinc}([d-c]t')\mathrm{d}t' \tag{A.8}$$

$$+ \int_0^{T_{\mathrm{RF}}} \frac{b(d+c)}{2d}\,\mathrm{sinc}([d+c]t')\mathrm{d}t' \tag{A.9}$$

$$= \frac{a}{d}\,\mathrm{Si}(dt')\Big|_0^{T_{\mathrm{RF}}} + \frac{b}{2d}\,\mathrm{Si}([d-c]t')\Big|_0^{T_{\mathrm{RF}}} + \frac{b}{2d}\,\mathrm{Si}([d+c]t')\Big|_0^{T_{\mathrm{RF}}} \tag{A.10}$$

$$= \frac{a}{d}\,\mathrm{Si}(d\cdot T_{\mathrm{RF}}) + \frac{b}{2d}\,\mathrm{Si}([d-c]T_{\mathrm{RF}}) + \frac{b}{2d}\,\mathrm{Si}([d+c]T_{\mathrm{RF}})\ . \tag{A.11}$$

By resubstitution of a, b, c and d Equation (A.11) becomes

$$I_{B_1} = \frac{A(1-\alpha)t_0}{\pi}\,\mathrm{Si}\left(\frac{\pi\ T_{\mathrm{RF}}}{t_0}\right) \tag{A.12}$$

$$+ \frac{A\alpha t_0}{2\pi}\left[\mathrm{Si}\left(-\frac{\pi\ T_{\mathrm{RF}}}{t_0}\left(\frac{1}{N}-1\right)\right) + \mathrm{Si}\left(\frac{\pi\ T_{\mathrm{RF}}}{t_0}\left(\frac{1}{N}+1\right)\right)\right]\ , \tag{A.13}$$

which can be reformulated to be

$$I_{B_1} = \frac{2A(1-\alpha)t_0\ \mathrm{Si}\left(\frac{\pi\ T_{\mathrm{RF}}}{t_0}\right) + A\alpha t_0\left[\mathrm{Si}\left(\frac{\pi\ T_{\mathrm{RF}}}{t_0}\left(1-\frac{1}{N}\right)\right) + \mathrm{Si}\left(\frac{\pi\ T_{\mathrm{RF}}}{t_0}\left(1+\frac{1}{N}\right)\right)\right]}{2\pi} \tag{A.14}$$

$$= \frac{At_0}{2\pi}\left[\alpha\left[\mathrm{Si}\left(\frac{\pi\ T_{\mathrm{RF}}(N-1)}{Nt_0}\right) + \mathrm{Si}\left(\frac{\pi\ T_{\mathrm{RF}}(N+1)}{Nt_0}\right)\right] - \left(2(\alpha-1)\ \mathrm{Si}\left(\frac{\pi\ T_{\mathrm{RF}}}{t_0}\right)\right)\right]\ . \tag{A.15}$$

Bibliography

[1] V. Gulani and N. Seiberlich. "Quantitative MRI: Rationale and Challenges". *Quantitative Magnetic Resonance Imaging*. Ed. by N. Seiberlich, V. Gulani, F. Calamante, A. Campbell-Washburn, M. Doneva, H. H. Hu, and S. Sourbron. Vol. 1. Advances in Magnetic Resonance Technology and Applications. Academic Press, 2020, pp. xxxvii–li (cit. on p. 1).

[2] A. P. Crawley and R. M. Henkelman. "A comparison of one-shot and recovery methods in T1 imaging". *Magn. Reson. Med.* 7 (1988), pp. 23–34 (cit. on p. 1).

[3] P. Schmitt, M. A. Griswold, P. M. Jakob, M. Kotas, V. Gulani, M. Flentje, and A. Haase. "Inversion recovery TrueFISP: quantification of T1, T2, and spin density". *Magn. Reson. Med.* 51 (2004), pp. 661–667 (cit. on pp. 1, 79, 92, 131).

[4] S. C. L. Deoni, T. M. Peters, and B. K. Rutt. "High-resolution T1 and T2 mapping of the brain in a clinically acceptable time with DESPOT1 and DESPOT2". *Magnetic Resonance in Medicine* 53 (2005), pp. 237–241 (cit. on p. 1).

[5] C. Graff, Z. Li, A. Bilgin, M. I. Altbach, A. F. Gmitro, and E. W. Clarkson. "Iterative T2 estimation from highly undersampled radial fast spin-echo data". *Proc. Int. Soc. Mag. Reson. Med.* 14 (2006), p. 925 (cit. on pp. 2, 45, 47, 73).

[6] V. T. Olafsson, D. C. Noll, and J. A. Fessler. "Fast Joint Reconstruction of Dynamic R_2^* and Field Maps in Functional MRI". *IEEE Trans. Med. Imag.* 27 (2008), pp. 1177–1188 (cit. on pp. 2, 45, 47, 73).

[7] K. T. Block, M. Uecker, and J. Frahm. "Model-Based Iterative Reconstruction for Radial Fast Spin-Echo MRI". *IEEE Trans. Med. Imaging* 28 (2009), pp. 1759–1769 (cit. on pp. 2, 45, 47, 73).

[8] X. Wang, Z. Tan, N. Scholand, V. Roeloffs, and M. Uecker. "Physics-based Reconstruction Methods for Magnetic Resonance Imaging". *Philos. Trans. R. Soc. A.* 379 (2021-05) (cit. on pp. 2, 45, 47, 73).

[9] X. Wang, V. Roeloffs, J. Klosowski, Z. Tan, D. Voit, M. Uecker, and J. Frahm. "Model-based T1 mapping with sparsity constraints using single-shot inversion-recovery radial FLASH". *Magn. Reson. Med.* 79 (2018), pp. 730–740 (cit. on pp. 2, 30, 47, 48, 64, 73, 79, 81, 89, 110, 130, 136).

[10] Z. Tan, D. Voit, J. M. Kollmeier, M. Uecker, and J. Frahm. "Dynamic water/fat separation and inhomogeneity mapping adjoint estimation using undersampled triple-echo multi-spoke radial FLASH". *Magn. Reson. Med.* 82 (2019), pp. 1000–1011 (cit. on pp. 2, 47, 48, 73, 130).

[11] D. Ma, V. Gulani, N. Seiberlich, K. Liu, J. L. Sunshine, J. L. Duerk, and M. A. Griswold. "Magnetic resonance fingerprinting". *Nature* 495 (2013), pp. 187–192 (cit. on pp. 2, 48, 73).

[12] J. Assländer, D. S. Novikov, R. Lattanzi, D. K. Sodickson, and M. A. Cloos. "Hybrid-state free precession in nuclear magnetic resonance". *Communications Physics* 2 (2019-06), p. 73 (cit. on pp. 2, 53, 77, 88, 120).

[13] N. Scholand. "Model-Based Reconstruction for Quantitative MRI using the Bloch Equations". Master's Thesis. Georg-August-Universität Göttingen, 2019 (cit. on pp. 2, 6, 8, 10, 12, 13, 18, 22, 23, 25–27, 34, 41, 42, 62, 117, 135).

[14] M. Uecker, S. Zhang, D. Voit, A. Karaus, K.-D. Merboldt, and J. Frahm. "Real-time MRI at a resolution of 20 ms". *NMR Biomed.* 23 (2010), pp. 986–994 (cit. on pp. 3, 30, 126).

[15] Z. P. Liang and P. C. Lauterbur. *Principles of Magnetic Resonance Imaging: A Signal Processing Perspective*. IEEE Press Series on Biomedical Engineering. Wiley, 1999 (cit. on pp. 5–7, 12, 16, 21–25, 33–35).

[16] M. A. Bernstein, K. F. King, and X. J. Zhou. *Handbook of MRI Pulse Sequences*. Elsevier Science, 2004 (cit. on pp. 8–12, 15, 21).

[17] C. P. Slichter. *Principles of Magnetic Resonance*. Springer-Verlag Berlin Heidelberg, 1990 (cit. on p. 9).

[18] F. Bloch. "Nuclear Induction". *Phys. Rev.* 70 (1946), pp. 460–474 (cit. on pp. 9, 17–19).

[19] M. Silver, R. Joseph, and D. Hoult. "Highly selective pi2 and pi pulse generation". *J. Magn. Reson.* 59 (1984), pp. 347–351 (cit. on p. 13).

[20] M. Garwood and L. DelaBarre. “The Return of the Frequency Sweep: Designing Adiabatic Pulses for Contemporary NMR”. *J. Magn. Reson.* 153 (2001), pp. 155–177 (cit. on pp. 14, 15).

[21] N. Bloembergen, E. M. Purcell, and R. V. Pound. “Nuclear magnetic relaxation”. *Nature* 160 (1947), pp. 475–476 (cit. on p. 17).

[22] N. Bloembergen, E. M. Purcell, and R. V. Pound. “Relaxation Effects in Nuclear Magnetic Resonance Absorption”. *Phys Rev* 73 (7 1948-04), pp. 679–712 (cit. on pp. 17, 18).

[23] J. Assländer, C. Gultekin, S. Flassbeck, S. J. Glaser, and D. K. Sodickson. “Generalized Bloch model: A theory for pulsed magnetization transfer”. *Magn. Reson. Med.* 87 (2022), pp. 2003–2017 (cit. on p. 17).

[24] H. C. Torrey. “Bloch Equations with Diffusion Terms”. *Phys. Rev.* 104 (3 1956), pp. 563–565 (cit. on p. 19).

[25] E. O. Stejskal. “Use of Spin Echoes in a Pulsed Magnetic-Field Gradient to Study Anisotropic, Restricted Diffusion and Flow”. *J. Chem. Phys.* 43 (1965), pp. 3597–3603 (cit. on p. 20).

[26] H. M. McConnell. “Reaction Rates by Nuclear Magnetic Resonance”. *J Chem Phys* 28 (1958), p. 430 (cit. on p. 20).

[27] J. Zhou, D. A. Wilson, P. Z. Sun, J. A. Klaus, and P. C. van Zijl. “Quantitative description of proton exchange processes between water and endogenous and exogenous agents for WEX, CEST, and APT experiments”. *Magn Reson Med* 51 (2004), pp. 945–952 (cit. on p. 20).

[28] R. Pohmann, E. Rommel, and M. von Kienlin. “Beyond k-Space: Spectral Localization Using Higher Order Gradients”. *J Magn Reson* 141 (1999), pp. 197–206 (cit. on p. 21).

[29] J. Hennig, A. M. Welz, G. Schultz, J. Korvink, Z. Liu, O. Speck, and M. Zaitsev. “Parallel imaging in non-bijective, curvilinear magnetic field gradients: a concept study”. *Magn Reson Mater Phys , Biol Med* 21 (2008), pp. 5–14 (cit. on p. 21).

[30] A. A. Maudsley. “Multiple-line-scanning spin density imaging”. *J. Magn. Reson.* 41 (1980), pp. 112–126 (cit. on p. 21).

[31] S. Müller. “Multifrequency selective rf pulses for multislice MR imaging”. *Magn. Reson. Med.* 6 (1988), pp. 364–371 (cit. on p. 21).

[32] D. J. Larkman, J. V. Hajnal, A. H. Herlihy, G. A. Coutts, I. R. Young, and G. Ehnholm. "Use of multicoil arrays for separation of signal from multiple slices simultaneously excited". *J. Magn. Reson. Imaging* 13 (2001), pp. 313–317 (cit. on p. 21).

[33] K. T. Block. "Advanced methods for radial data sampling in magnetic resonance imaging". PhD thesis. Georg August Universität Göttingen, 2008 (cit. on p. 27).

[34] K. T. Block and J. Frahm. "Spiral imaging: a critical appraisal". *J. Magn. Reson. Imaging* 21 (2005), pp. 657–668 (cit. on pp. 27, 124).

[35] M. Blaimer, F. Breuer, M. Mueller, R. M. Heidemann, M. A. Griswold, and P. M. Jakob. "SMASH, SENSE, PILS, GRAPPA: How to Choose the Optimal Method". *Top. Magn. Reson. Imaging* 15 (2004), pp. 223–236 (cit. on pp. 28, 40).

[36] M. Uecker, T. Hohage, K. T. Block, and J. Frahm. "Image reconstruction by regularized nonlinear inversion-joint estimation of coil sensitivities and image content". *Magn. Reson. Med.* 60 (2008), pp. 674–682 (cit. on pp. 28, 37, 65, 77, 89).

[37] E. L. Hahn. "Spin Echoes". *Phys. Rev.* 80 (4 1950), pp. 580–594 (cit. on p. 29).

[38] A. Haase. "Snapshot flash mri. applications to t1, t2, and chemical-shift imaging". *Magn. Reson. Med.* 13 (1990), pp. 77–89 (cit. on p. 30).

[39] A. P. Crawley, M. L. Wood, and R. M. Henkelman. "Elimination of transverse coherences in FLASH MRI". *Magn. Reson. Med.* 8 (1988), pp. 248–260 (cit. on p. 30).

[40] Y. Zur, M. L. Wood, and L. J. Neuringer. "Spoiling of transverse magnetization in steady-state sequences". *Magn. Reson. Med.* 21 (1991), pp. 251–263 (cit. on p. 30).

[41] V. Roeloffs, D. Voit, and J. Frahm. "Spoiling without additional gradients: Radial FLASH MRI with randomized radiofrequency phases". *Magn. Reson. Med.* 75 (2016), pp. 2094–2099 (cit. on p. 30).

[42] D. C. Look and D. R. Locker. "Time saving in measurement of NMR and EPR relaxation times". *Rev. Sci. Instrum.* 41 (1970), pp. 250–251 (cit. on pp. 30, 90).

[43] V. Roeloffs, X. Wang, T. J. Sumpf, M. Untenberger, D. Voit, and J. Frahm. "Model-based reconstruction for T1 mapping using single-shot inversion-recovery radial FLASH". *Int. J. Imag. Syst. Tech.* 26 (2016), pp. 254–263 (cit. on pp. 30, 91, 130).

[44] H. Y. Carr. "Steady-State Free Precession in Nuclear Magnetic Resonance". *Phys. Rev.* 112 (5 1958), pp. 1693–1701 (cit. on p. 31).

[45] O. Bieri and K. Scheffler. "On the origin of apparent low tissue signals in balanced SSFP". *Magn. Reson. Med.* 56 (2006), pp. 1067–1074 (cit. on pp. 31, 87).

[46] O. Bieri and K. Scheffler. “Optimized balanced steady-state free precession magnetization transfer imaging”. *Magn. Reson. Med.* 58 (2007), pp. 511–518 (cit. on p. 31).

[47] M. Gloor, K. Scheffler, and O. Bieri. “Quantitative magnetization transfer imaging using balanced SSFP”. *Magn. Reson. Med.* 60 (2008), pp. 691–700 (cit. on p. 31).

[48] O. Bieri and K. Scheffler. “SSFP signal with finite RF pulses”. *Magn. Reson. Med.* 62 (2009), pp. 1232–1241 (cit. on p. 31).

[49] K. Scheffler and S. Lehnhardt. “Principles and applications of balanced SSFP techniques”. *Eur. Radiol.* 13 (2003), pp. 2409–2418 (cit. on pp. 31, 91).

[50] R. Freeman and H. D. W. Hill. “Phase and intensity anomalies in Fourier transform NMR”. *J. Magn. Reson.* 4 (1971), pp. 366–383 (cit. on p. 31).

[51] K. Scheffler and J. Hennig. “Is TrueFISP a gradient-echo or a spin-echo sequence?” *Magn. Reson. Med.* 49 (2003), pp. 395–397 (cit. on p. 31).

[52] D. G. Nishimura and S. S. Vasanawala. “Analysis and Reduction of the Transient Response in SSFP Imaging”. *Proc. 8th Annual Meeting ISMRM*. Denver. 2000 (cit. on p. 31).

[53] B. A. Hargreaves, S. S. Vasanawala, J. M. Pauly, and D. G. Nishimura. “Characterization and reduction of the transient response in steady-state MR imaging”. *Magn. Reson. Med.* 46 (2001), pp. 149–158 (cit. on p. 31).

[54] D. Hoult and P. C. Lauterbur. “The sensitivity of the zeugmatographic experiment involving human samples”. *J. Magn. Reson.* 34 (1979), pp. 425–433 (cit. on p. 36).

[55] M. Uecker, P. Lai, M. J. Murphy, P. Virtue, M. Elad, J. M. Pauly, S. S. Vasanawala, and M. Lustig. “ESPIRiT—an eigenvalue approach to autocalibrating parallel MRI: where SENSE meets GRAPPA”. *Magn. Reson. Med.* 71 (2014), pp. 990–1001 (cit. on pp. 37, 47, 85).

[56] L. Ying and J. Sheng. “Joint image reconstruction and sensitivity estimation in SENSE (JSENSE)”. *Magn. Reson. Med.* 57 (2007), pp. 1196–1202 (cit. on pp. 37, 65).

[57] A. B. Bakushinsky and M. Y. Kokurin. *Iterative Methods for Approximate Solution of Inverse Problems*. Mathematics and Its Applications. Springer Science & Business Media, 2005 (cit. on p. 38).

[58] M. Uecker. “Nonlinear Reconstruction Methods for Parallel Magnetic Resonance Imaging”. PhD thesis. Georg-August-Universität Göttingen, 2009 (cit. on p. 38).

[59] D. J. Park. “B1 Mapping for Magnetic Resonance Imaging”. PhD thesis. Brigham Young University - Provo, 2014 (cit. on p. 43).

[60] E. Insko and L. Bolinger. “Mapping of the Radiofrequency Field”. *J. Magn. Reson.* 103 (1993). Series A, pp. 82–85 (cit. on p. 43).

[61] R. Stollberger and P. Wach. “Imaging of the active B1 field in vivo”. *Magn. Reson. Med.* 35 (1996), pp. 246–251 (cit. on p. 43).

[62] S. Chung, D. Kim, E. Breton, and L. Axel. “Rapid B1+ mapping using a preconditioning RF pulse with TurboFLASH readout”. *Magn. Reson. Med.* 64 (2010), pp. 439–446 (cit. on pp. 43, 44, 80).

[63] R. R. Ernst, G. Bodenhausen, and A. Wokaun. *Principles of nuclear magnetic resonance in one and two dimensions*. Oxford University Press, 1997 (cit. on p. 44).

[64] K. S. Nayak and D. G. Nishimura. “Automatic field map generation and off-resonance correction for projection reconstruction imaging”. *Magn. Reson. Med.* 43 (2000), pp. 151–154 (cit. on p. 45).

[65] F. H. Petzschner, I. P. Ponce, M. Blaimer, P. M. Jakob, and F. A. Breuer. “Fast MR parameter mapping using k-t principal component analysis”. *Magn. Reson. Med.* 66 (2011), pp. 706–716 (cit. on pp. 45, 73).

[66] C. Huang, C. G. Graff, E. W. Clarkson, A. Bilgin, and M. I. Altbach. “T2 mapping from highly undersampled data by reconstruction of principal component coefficient maps using compressed sensing”. *Magn. Reson. Med.* 67 (2012), pp. 1355–1366 (cit. on pp. 45, 73).

[67] B. Zhao, W. Lu, T. K. Hitchens, F. Lam, C. Ho, and Z.-P. Liang. “Accelerated MR parameter mapping with low-rank and sparsity constraints”. *Magn. Reson. Med.* 74 (2015), pp. 489–498 (cit. on pp. 45, 73).

[68] J. I. Tamir, M. Uecker, W. Chen, P. Lai, M. T. Alley, S. S. Vasanawala, and M. Lustig. “T2 shuffling: Sharp, multicontrast, volumetric fast spin-echo imaging”. *Magn. Reson. Med.* 77 (2017), pp. 180–195 (cit. on pp. 45, 73).

[69] J. Assländer, M. A. Cloos, F. Knoll, D. K. Sodickson, J. Hennig, and R. Lattanzi. “Low rank alternating direction method of multipliers reconstruction for MR fingerprinting”. *Magn. Reson. Med.* 79 (2018), pp. 83–96 (cit. on pp. 45, 73).

[70] T. J. Sumpf, M. Uecker, S. Boretius, and J. Frahm. “Model-based nonlinear inverse reconstruction for T2-mapping using highly undersampled spin-echo MRI”. *J. Magn. Reson. Imaging* 34 (2011), pp. 420–428 (cit. on pp. 45, 47, 73).

[71] J. I. Tamir, V. Taviani, S. Vasanawala, and M. Lustig. "T1-T2 Shuffling: Multi-Contrast 3D Fast Spin-Echo with T1 and T2 Sensitivity". *Proc. Intl. Soc. Mag. Reson. Med.* Vol. 25. Honolulu, 2017, p. 451 (cit. on p. 46).

[72] T. Hilbert, T. J. Sumpf, E. Weiland, J. Frahm, J.-P. Thiran, R. Meuli, T. Kober, and G. Krueger. "Accelerated T2 mapping combining parallel MRI and model-based reconstruction: GRAPPATINI". *J. Magn. Reson. Imaging* 48 (2018), pp. 359–368 (cit. on pp. 47, 73).

[73] N. Ben-Eliezer, D. K. Sodickson, T. Shepherd, G. C. Wiggins, and K. T. Block. "Accelerated and motion-robust in vivo T2 mapping from radially undersampled data using bloch-simulation-based iterative reconstruction". eng. *Magn. Reson. Med.* 75 (2016-03), pp. 1346–1354 (cit. on pp. 47, 48, 74).

[74] A. Sbrizzi, O. van der Heide, M. Cloos, A. van der Toorn, H. Hoogduin, P. R. Luijten, and C. A. van den Berg. "Fast quantitative MRI as a nonlinear tomography problem". *Magn Reson Imaging* 46 (2018), pp. 56–63 (cit. on pp. 47, 48, 74).

[75] M. Weigel. "Extended phase graphs: Dephasing, RF pulses, and echoes-pure and simple". *J. Magn. Reson. Imaging* 41 (2015), pp. 266–295 (cit. on p. 49).

[76] C. Guenthner, T. Amthor, M. Doneva, and S. Kozerke. "A unifying view on extended phase graphs and Bloch simulations for quantitative MRI". *Sci. Rep.* 11 (2021-10), pp. 2045–2322 (cit. on p. 49).

[77] J. Bittoun, J. Taquin, and M. Sauzade. "A computer algorithm for the simulation of any Nuclear Magnetic Resonance (NMR) imaging method". *Magn. Reson. Imaging* 2 (1984), pp. 113–120 (cit. on pp. 49, 52).

[78] G. Strang. "On the Construction and Comparison of Difference Schemes". *SIAM J. Numer. Anal.* 5 (1968), pp. 506–517 (cit. on p. 52).

[79] A. Hazra. "Numerical Simulation of Bloch Equations for Dynamic Magnetic Resonance Imaging". PhD thesis. Georg-August University School of Science, 2016 (cit. on p. 52).

[80] S. J. Malik, R. P. A. G. Teixeira, D. J. West, T. C. Wood, and J. V. Hajnal. "Steady-state imaging with inhomogeneous magnetization transfer contrast using multiband radiofrequency pulses". *Magn. Reson. Med.* 83 (2020), pp. 935–949 (cit. on pp. 53, 77, 88).

[81] C. Moler and C. van Loan. "Nineteen Dubious Ways to Compute the Exponential of a Matrix". *SIAM Rev.* 20 (1978) (cit. on pp. 53, 77).

[82] C. Moler and C. V. Loan. "Nineteen Dubious Ways to Compute the Exponential of a Matrix, Twenty-Five Years Later*". *SIAM Rev.* 45 (2003), p. 3 (cit. on pp. 53, 77).

[83] W. H. Press, S. A. Teukolsky, W. T. Vetterling, and B. P. Flannery. *Numerical Recipes in C (2Nd Ed.): The Art of Scientific Computing*. New York, NY, USA: Cambridge University Press, 1992 (cit. on pp. 54, 55).

[84] J. Dormand and P. Prince. "A family of embedded Runge-Kutta formulae". *J. Comput. Appl. Math.* 6 (1980), pp. 19–26 (cit. on pp. 55, 79, 83).

[85] R. P. Dickinson and R. J. Gelinas. "Sensitivity analysis of ordinary differential equation systems-A direct method". *J. Comput. Phys.* 21 (1976), pp. 123–143 (cit. on pp. 59, 74, 75).

[86] A. Chulliat, S. Macmillan, P. Alken, C. D. Beggan, M. C. Nair, B. Hamilton, A. Woods, V. Ridley, S. Maus, and A. W. P. Thomson. "The US/UK World Magnetic Model for 2015-2020". Retrieved 21 February 2016. National Geophysical Data Center. 2015 (cit. on p. 61).

[87] K. F. Stupic et al. "A standard system phantom for magnetic resonance imaging". *Magn. Reson. Med.* 86 (2021), pp. 1194–1211 (cit. on pp. 63, 81, 86, 88).

[88] T. J. Sumpf, A. Petrovic, M. Uecker, F. Knoll, and J. Frahm. "Fast T2 Mapping With Improved Accuracy Using Undersampled Spin-Echo MRI and Model-Based Reconstructions With a Generating Function". *IEEE Trans. Med. Imaging* 33 (2014), pp. 2213–2222 (cit. on pp. 64, 81).

[89] K. P. Pruessmann, M. Weiger, M. B. Scheidegger, and P. Boesiger. "SENSE: sensitivity encoding for fast MRI". *Magn. Reson. Med.* 42 (1999), pp. 952–962 (cit. on p. 65).

[90] M. Guerquin-Kern, L. Lejeune, K. P. Pruessmann, and M. Unser. "Realistic Analytical Phantoms for Parallel Magnetic Resonance Imaging". *IEEE Trans. Med. Imaging* 31 (2012), pp. 626–636 (cit. on pp. 65, 66).

[91] R. Van De Walle, H. Barrett, K. Myers, M. Aitbach, B. Desplanques, A. Gmitro, J. Cornelis, and I. Lemahieu. "Reconstruction of MR images from data acquired on a general nonregular grid by pseudoinverse calculation". *IEEE Trans. Med. Imaging* 19 (2000), pp. 1160–1167 (cit. on p. 66).

[92] M. Blumenthal, G. Luo, M. Schilling, H. C. M. Holme, and M. Uecker. "Deep, deep learning with BART". *Magn. Reson. Med.* 89 (2023), pp. 678–693 (cit. on pp. 69, 79).

[93] P. K. Lee, L. E. Watkins, T. I. Anderson, G. Buonincontri, and B. A. Hargreaves. "Flexible and efficient optimization of quantitative sequences using automatic differentiation of Bloch simulations". *Magn. Reson. Med.* 82 (2019), pp. 1438–1451 (cit. on p. 73).

[94] G. Dong, M. Hintermüller, and K. Papafitsoros. "Quantitative Magnetic Resonance Imaging: From Fingerprinting to Integrated Physics-Based Models". *SIAM J. Imag. Sci.* 12 (2019), pp. 927–971 (cit. on p. 73).

[95] N. Scholand, X. Wang, S. Rosenzweig, and M. Uecker. "Generalized model-based reconstruction for quantitative MRI using the Bloch-Equations". *Magn. Reson. Mater. Phy.* 36 (2019), 32(Suppl 1) (cit. on p. 74).

[96] N. Scholand, X. Wang, S. Rosenzweig, H. C. M. Holme, and M. Uecker. "Generic Quantitative MRI using Model-Based Reconstruction with the Bloch Equations". *Proc. Intl. Soc. Mag. Reson. Med.* 28 (2020) (cit. on p. 74).

[97] N. Scholand, C. Graf, and M. Uecker. "Efficient Bloch Simulation Based on Pre-computed State-Transition Matrices". *Proc. Intl. Soc. Mag. Reson. Med.* 30 (2022) (cit. on p. 74).

[98] N. Scholand and M. Uecker. "Sensitivity Analysis of the Bloch Equations". *Proc. Intl. Soc. Mag. Reson. Med.* 30 (2022) (cit. on p. 74).

[99] S. Vasanawala, M. Murphy, M. Alley, P. Lai, K. Keutzer, J. Pauly, and M. Lustig. "Practical parallel imaging compressed sensing MRI: Summary of two years of experience in accelerating body MRI of pediatric patients". *Proc. IEEE Int. Symp. Biomed. Imaging* 2011 (2011), pp. 1039–1043 (cit. on p. 77).

[100] A. Beck and M. Teboulle. "A Fast Iterative Shrinkage-Thresholding Algorithm for Linear Inverse Problems". *SIAM J. Img. Sci.* 2 (2009), pp. 183–202 (cit. on p. 77).

[101] M. Uecker, P. Virtue, F. Ong, M. J. Murphy, M. T. Alley, S. S. Vasanawala, and M. Lustig. "Software toolbox and programming library for compressed sensing and parallel imaging". *ISMRM Workshop on Data Sampling and Image Reconstruction.* Sedona, 2013 (cit. on p. 79).

[102] J. P. Wansapura, S. K. Holland, R. S. Dunn, and W. S. Ball Jr. "NMR relaxation times in the human brain at 3.0 tesla". *J. Magn. Reson. Imaging* 9 (1999), pp. 531–538 (cit. on pp. 80, 113, 115, 118, 128).

[103] M. Deimling and O. Heid. "Magnetization prepared trueFISP imaging". *Proceedings of the 2nd Annual Meeting of ISMRM, San Francisco* (1994), p. 495 (cit. on p. 80).

[104] V. S. Deshpande, Y.-C. Chung, Q. Zhang, S. M. Shea, and D. Li. "Reduction of transient signal oscillations in true-FISP using a linear flip angle series magnetization preparation". *Magn. Reson. Med.* 49 (2003), pp. 151–157 (cit. on p. 80).

[105] X. Wang, S. Rosenzweig, N. Scholand, H. C. M. Holme, and M. Uecker. "Model-based Reconstruction for Simultaneous Multi-slice T1 Mapping using Single-shot Inversion-recovery Radial FLASH". *Magn. Reson. Med.* 85 (2021), pp. 1258–1271 (cit. on p. 80).

[106] X. Wang, S. Rosenzweig, N. Scholand, H. C. M. Holme, and M. Uecker. *Data for: Model-Based Reconstruction for Simultaneous Multi-Slice T1 Mapping using Single-Shot Inversion-Recovery Radial FLASH [Data set].* Zenodo. 2020 (cit. on p. 80).

[107] R. Deichmann. "Fast high-resolution T1 mapping of the human brain". *Magn. Reson. Med.* 54 (2005), pp. 20–27 (cit. on pp. 81, 90, 91).

[108] S. J. Graham and R. M. Henkelman. "Understanding pulsed magnetization transfer". *J. Magn. Reson. Imaging* 7 (1997), pp. 903–912 (cit. on p. 88).

[109] O. Maier, J. Schoormans, M. Schloegl, G. J. Strijkers, A. Lesch, T. Benkert, T. Block, B. F. Coolen, K. Bredies, and R. Stollberger. "Rapid T1 quantification from high resolution 3D data with model-based reconstruction". *Magn. Reson. Med.* 81 (2019), pp. 2072–2089 (cit. on pp. 88, 138).

[110] Z. Tan, T. Hohage, O. Kalentev, A. A. Joseph, X. Wang, D. Voit, K.-D. Merboldt, and J. Frahm. "An eigenvalue approach for the automatic scaling of unknowns in model-based reconstructions: Applications to real-time phase-contrast flow MRI". *NMR Biomed.* 30 (2017), e3835 (cit. on pp. 88, 138).

[111] J. Assländer, R. Lattanzi, D. K. Sodickson, and M. A. Cloos. "Optimized quantification of spin relaxation times in the hybrid state". *Magn. Reson. Med.* 82 (2019), pp. 1385–1397 (cit. on p. 88).

[112] L. Feng, F. Liu, G. Soultanidis, C. Liu, T. Benkert, K. T. Block, Z. A. Fayad, and Y. Yang. "Magnetization-prepared GRASP MRI for rapid 3D T1 mapping and fat/water-separated T1 mapping". *Magn. Reson. Med.* 86 (2021), pp. 97–114 (cit. on p. 88).

[113] R. Deichmann and A. Haase. "Quantification of T1 values by SNAPSHOT-FLASH NMR imaging". *J. Magn. Reson.* 96 (1992). Journal of Magnetic Resonance (1969), pp. 608–612 (cit. on p. 90).

[114] S. Clare and P. Jezzard. “Rapid T1 mapping using multislice echo planar imaging”. *Magn. Reson. Med.* 45 (2001), pp. 630–634 (cit. on p. 91).

[115] P. Ehses, N. Seiberlich, D. Ma, F. A. Breuer, P. M. Jakob, M. A. Griswold, and V. Gulani. “IR TrueFISP with a golden-ratio-based radial readout: Fast quantification of T1, T2, and proton density”. *Magn. Reson. Med.* 69 (2013), pp. 71–81 (cit. on pp. 92, 105).

[116] J. Pfister, M. Blaimer, W. H. Kullmann, A. J. Bartsch, P. M. Jakob, and F. A. Breuer. “Simultaneous T1 and T2 measurements using inversion recovery TrueFISP with principle component-based reconstruction, off-resonance correction, and multi-component analysis”. *Magn. Reson. Med.* 81 (2019), pp. 3488–3502 (cit. on pp. 92, 120).

[117] O. Bieri and K. Scheffler. “Fundamentals of balanced steady state free precession MRI”. *J. Magn. Reson. Imaging* 38 (2013), pp. 2–11 (cit. on p. 117).

[118] C. Ganter. “Off-resonance effects in the transient response of SSFP sequences”. *Magn. Reson. Med.* 52 (2004), pp. 368–375 (cit. on p. 120).

[119] J. L. Wilson, M. Jenkinson, and P. Jezzard. “Optimization of static field homogeneity in human brain using diamagnetic passive shims”. *Magn. Reson. Med.* 48 (2002), pp. 906–914 (cit. on p. 121).

[120] A. J. Lesch. “Application of Variational Methods for Field Mapping in Magnetic Resonance Imaging”. PhD thesis. Graz University of Technology, 2020 (cit. on p. 122).

[121] F. Roméo and D. I. Hoult. “Magnet field profiling: Analysis and correcting coil design”. *Magn. Reson. Med.* 1 (1984), pp. 44–65 (cit. on p. 122).

[122] R. Gruetter and C. Boesch. “Fast, noniterative shimming of spatially localized signals. In vivo analysis of the magnetic field along axes”. *J. Magn. Reson.* 96 (1992). Journal of Magnetic Resonance (1969), pp. 323–334 (cit. on p. 122).

[123] R. Gruetter. “Automatic, localized in Vivo adjustment of all first-and second-order shim coils”. *Magn. Reson. Med.* 29 (1993), pp. 804–811 (cit. on p. 122).

[124] S. Kanayamay, S. Kuhara, and K. Satoh. “In vivo rapid magnetic field measurement and shimming using single scan differential phase mapping”. *Magn. Reson. Med.* 36 (1996), pp. 637–642 (cit. on p. 122).

[125] L. M. Klassen and R. S. Menon. “Robust automated shimming technique using arbitrary mapping acquisition parameters (RASTAMAP)”. *Magn. Reson. Med.* 51 (2004), pp. 881–887 (cit. on p. 122).

[126] C. B. Ahn and Z. H. Cho. “Analysis of eddy currents in nuclear magnetic resonance imaging”. *Magn. Reson. Med.* 17 (1991), pp. 149–163 (cit. on p. 124).

[127] C. Boesch, R. Gruetter, and E. Martin. “Temporal and spatial analysis of fields generated by eddy currents in superconducting magnets: Optimization of corrections and quantitative characterization of magnet/gradient systems”. *Magn. Reson. Med.* 20 (1991), pp. 268–284 (cit. on p. 124).

[128] M. T. Alley, G. H. Glover, and N. J. Pelc. “Gradient characterization using a Fourier-transform technique”. *Magn. Reson. Med.* 39 (1998), pp. 581–587 (cit. on p. 124).

[129] C. Barmet, N. D. Zanche, and K. P. Pruessmann. “Spatiotemporal magnetic field monitoring for MR”. *Magn. Reson. Med.* 60 (2008), pp. 187–197 (cit. on p. 124).

[130] B. E. Dietrich, D. O. Brunner, B. J. Wilm, C. Barmet, S. Gross, L. Kasper, M. Haeberlin, T. Schmid, S. J. Vannesjo, and K. P. Pruessmann. “A field camera for MR sequence monitoring and system analysis”. *Magn. Reson. Med.* 75 (2016), pp. 1831–1840 (cit. on p. 124).

[131] S. J. Vannesjo, M. Haeberlin, L. Kasper, M. Pavan, B. J. Wilm, C. Barmet, and K. P. Pruessmann. “Gradient system characterization by impulse response measurements with a dynamic field camera”. *Magn. Reson. Med.* 69 (2013), pp. 583–593 (cit. on p. 124).

[132] M. Stich, T. Wech, A. Slawig, R. Ringler, A. Dewdney, A. Greiser, G. Ruyters, T. A. Bley, and H. Köstler. “Gradient waveform pre-emphasis based on the gradient system transfer function”. *Magn. Reson. Med.* 80 (2018), pp. 1521–1532 (cit. on p. 124).

[133] K. T. Block and M. Uecker. “Simple Method for Adaptive Gradient-Delay Compensation in Radial MRI”. *Proc. Intl. Soc. Mag. Reson. Med.* Vol. 19. Montreal, 2011, p. 2816 (cit. on p. 125).

[134] S. Rosenzweig, H. C. M. Holme, and M. Uecker. “Simple auto-calibrated gradient delay estimation from few spokes using Radial Intersections (RING)”. *Magn. Reson. Med.* 81 (2019), pp. 1898–1906 (cit. on p. 125).

[135] V. Roeloffs, M. Bush, S. Anand, and M. Lustig. “Measuring and Correcting Gradient Delays in Multi-Echo Rosette Trajectories with RING”. *Proc. Intl. Soc. Mag. Reson. Med.* Vol. 28. Sidney, 2020 (cit. on p. 125).

Acknowledgments

Zuallererst möchte ich meinem Betreuer Prof. Martin Uecker danken. Seine Freude und Begeisterung an der MRT, seine Leidenschaft für freie Software und reproduzierbare Forschung sowie seine Hilfsbereitschaft und Offenheit in leichten und schwierigen Momenten, haben mich immer wieder motiviert, mir neue Perspektiven eröffnet und diese Promotion erst ermöglicht. Ich bin ihm sehr dankbar für die zahlreiche Unterstützung beim Verfassen von Dokumenten, für die Freiheiten und das Vertrauen, das er mir entgegen gebracht hat, die Möglichkeit ihn an die Technische Universität Graz zu begleiten sowie die vielen Chancen Kollaborationspartner, internationale Konferenzen und Workshops zu besuchen.

Ein weiterer Dank gehört Prof. Hans-Christian Hofsäss, Prof. Susann Boretius und Prof. Stefan Luther für die Diskussionen, die Ratschläge und all die weitere Unterstützung im Betreuungsausschuss dieser Dissertation.

Ausserdem möchte ich Prof. Andreas Tilgner und Prof. Russell Luke für ihre Unterstützung im Rahmen meines Prüfungskommittees danken.

Besonders möchte ich mich bei allen aktuellen und ehemaligen Kollegen am Standort der Universitätsmedizin in Göttingen und am Institut für Biomedizinische Bildgebung in Graz bedanken. Ich habe die Zeit mit euch allen sehr genossen! Ich bin euch dankbar für die tolle Atmosphäre und die viele fachliche und freundschaftliche Unterstützung, die ich von euch erhalten durfte. Ich verstehe es als grosses Privileg, dass ich so viel Zeit mit euch auch ausserhalb der Arbeit in Kneipen, im Kino, beim Grillen, auf Reiterhöfen oder beim Zubereiten und Verkosten von Dumblings verbringen durfte. Vielen Dank euch allen!

Ausserdem möchte ich mich ganz herzlich bei der Max-Planck Gesellschaft und meiner Graduiertenschule dem IMPRS-PBCS sowie ihren fantastischen Koordinatoren Frauke Bergmann und Antje Erdmann bedanken. Es hat mir immer viel Freude bereitet in einem so diversen, weltoffenen und Promovierenden-nahen Promotionsprogramm zu sein! Die

Retreats, Workshops und Konferenzen habe ich sehr genossen und sie haben mich stets motiviert über den Tellerand meiner eigenen Forschung hinauszuschauen und viele nette Menschen kennenzulernen.

Ich möchte mich zusätzlich bei allen bedanken, die mir geholfen haben Rechtschreibfehler und unpassende Formulierungen aufzuspüren und ihnen vorzubeugen. Vielen Dank an Pauline, Basti, Moritz, Christian, Philip und Xiaoqing für eure ganze Zeit und Spontanität.

Natürlich gehört grosser Dank meiner Freundin Pauline und unserem Hund Tréju, die mich durch die Aufs und Abs dieser Dissertation begleitet haben und mich immer mit Rat und Tat unterstützten. Ich bin so froh, dass es euch gibt!

Schlussendlich bin ich meinen Eltern, meinem Bruder und meiner ganzen tollen Familie sehr dankbar. Auch wenn wir mittlerweile über einige Orte verstreut wohnen, habt ihr mir immer viel Kraft geschenkt und ich konnte mich jederzeit auf euch verlassen. Vielen vielen Dank dafür!

Nick Scholand, M.Sc. B.Sc.

Education

since 2019 **PhD Candidate**

International Max Planck Research School - Physics of Biological and Complex Systems

Göttingen Graduate Center for Neurosciences, Biophysics, and Molecular Biosciences

Group:	Computational MRI Research Group of Prof. Dr. Uecker
since 2021:	Institute of Biomedical Imaging Graz University of Technology
2019 - 2021:	Department of Diagnostic and Interventional Radiology University Medical Center Göttingen
PhD Track:	Physics of Biological and Complex Systems

2019 Finished Master of Physics - University of Göttingen

Institute:	University Medical Center Göttingen
Department:	Cardiovascular MRI Research Group of Prof. Dr. Uecker in the Institute for Diagnostic and Interventional Radiology
Topic:	Model-Based Reconstruction for Quantitative MRI using the Bloch Equations

2016 Erasmus Exchange Semester - University of Amsterdam

2015 - 2019 **Master of Science in Physics** - University of Göttingen

Track:	Biophysics and Complex Systems

2015 Finished Bachelor of Physics - University of Göttingen

Institute:	Max-Planck-Institute for Dynamic and Self-Organization, Göttingen
Department:	Fluid Physics, Pattern Formation and Biocomplexity
Topic:	Stochastic Description of Myosin(II)-, Coronin- and Aip1-Null Mutants of Dictyostelium Discoideum

2012 - 2015 **Bachelor of Science in Physics** - University of Göttingen

2012 University Entrance Qualification

Publications

Journal

1. **Nick Scholand**, Xiaoqing Wang, Volkert Roeloffs, Sebastian Rosenzweig, Martin Uecker. *Quantitative Magnetic Resonance Imaging by Nonlinear Inversion of the Bloch Equations.* Magn. Reson. Med.:1-19 (2023) doi: 10.1002/mrm.29664

2. Xiaoqing Wang, Sebastian Rosenzweig, Volkert Roeloffs, Moritz Blumenthal, **Nick Scholand**, Zhengguo Tan, H. Christian M. Holme, Martin Uecker. *Free-Breathing Myocardial T1 Mapping using Inversion-Recovery Radial FLASH and Motion-Resolved Model-Based Reconstruction.* Magn. Reson. Med. 89:1368-1384 (2023)

3. Zhengguo Tan, Christina Unterberg-Buchwald, Moritz Blumenthal, **Nick Scholand**, Philip Schaten, Christian Holme, Xiaoqing Wang, Dirk Raddatz, Martin Uecker. *Free-Breathing Water, Fat, R2* and B0 Field Mapping of the Liver Using Multi-Echo Radial FLASH and Regularized Model-based Reconstruction (MERLOT).* IEEE Trans. Med. Imag. (2022), doi: 10.1109/TMI.2022.3228075

4. Xiaoqing Wang, Zhengguo Tan, **Nick Scholand**, Volkert Roeloffs, Martin Uecker. *Physics-based Reconstruction Methods for Magnetic Resonance Imaging.* Philosophical Transactions of the Royal Society A. 379:20200196 (2021)

5. Xiaoqing Wang, Sebastian Rosenzweig, **Nick Scholand**, H.Christian M.Holme, Martin Uecker. Model-based Reconstruction for *Simultaneous Multi-slice T1 Mapping using Single-shot Inversion-recovery Radial FLASH.* Magn. Reson. Med. 85:1258-1271 (2021)

6. Sebastian Rosenzweig, **Nick Scholand**, H. Christian M. Holme, Martin Uecker. *Cardiac and Respiratory Self-Gating in Radial MRI using an Adapted Singular Spectrum Analysis (SSA-FARI)*, IEEE Trans. Med. Imag. 39:3029-3041 (2020)

Conferences

1. **Nick Scholand**, Martin Schilling, Martin Heide, Martin Uecker. *Digital Reference Objects with BART.* ISMRM 2023. In Proc. Intl. Soc. Mag. Reson. Med. 31; 3118 (2023)

2. **Nick Scholand**, Christina Graf, Martin Uecker. *Efficient Bloch Simulation Based on Precomputed State-Transition Matrices.* ISMRM 2022. In Proc. Intl. Soc. Mag. Reson. Med. 30; 0748 (2022)

3. Xiaoqing Wang, Moritz Blumenthal, **Nick Scholand**, Martin Uecker. *Model-Based Reconstruction with Automatic Differentiation for Single-Shot Myocardial T1 Mapping using Radial MOLLI with FLASH Readout.* ISMRM 2022. In Proc. Intl. Soc. Mag. Reson. Med. 30; 1111 (2022)

4. **Nick Scholand**, Martin Uecker. *Sensivitiy Analysis of the Bloch Equations.* ISMRM 2022. In Proc. Intl. Soc. Mag. Reson. Med. 30; 1700 (2022)

5. Zhengguo Tan, Sebastian Rosenzweig, Xiaoqing Wang, **Nick Scholand**, H. Christian M. Holme, Moritz Blumenthal, Martin Uecker. *Free-Breathing Liver Fat and R2* Mapping: Multi-Echo Radial FLASH and Model-based Reconstruction (MERLOT).* ISMRM 2021. In Proc. Intl. Soc. Mag. Reson. Med. 29; 0753 (2021)

6. Volkert Roeloffs, **Nick Scholand**, Martin Uecker. *Fast-Sweep Frequency-Modulated SSFP: Boosting Sensitivity for 3D Joint T1/T2 Mapping.* ISMRM 2021. In Proc. Intl. Soc. Mag. Reson. Med. 29; 3052 (2021)

7. Xiaoqing Wang, Sebastian Rosenzweig, Moritz Blumenthal, Zhengguo Tan, **Nick Scholand**, Martin Uecker. Free-breathing, motion-resolved myocardial T1 mapping using inversion-recovery radial FLASH and model-based reconstruction. ISMRM 2021. In Proc. Intl. Soc. Mag. Reson. Med. 29; 3598 (2021)

8. Ansgar Adler, Jost M. Kollmeier, **Nick Scholand**, Sebastian Rosenzweig, Yong Wang, Martin Uecker. *Simulation of Flowing Spins in MRI using the Lattice Boltzmann Method.* ISMRM 2021. Proc. Intl. Soc. Mag. Reson. Med. 29; 2100 (2021)

9. **Nick Scholand**, Xiaoqing Wang, Sebastian Rosenzweig, H. Christian M. Holme, Martin Uecker. *Generic Quantitative MRI using Model-Based Reconstruction with the Bloch Equations.* ISMRM Virtual Conference & Exhibition 2020, In Proc. Intl. Soc. Mag. Reson. Med. 28; 0885 (2020)

10. Zhengguo Tan, Peter Dechent, Xiaoqing Wang, **Nick Scholand**, Dirk Voit, Jens Frahm, Martin Uecker. *Dynamic Water, Fat, R2* and B0 Field Inhomogeneity Quantification Using Multi-Echo Multi-Spoke Radial FLASH*. ISMRM Virtual Conference & Exhibition 2020, In Proc. Intl. Soc. Mag. Reson. Med. 28; 1019 (2020)

11. **Nick Scholand**, Xiaoqing Wang, Sebastian Rosenzweig, Martin Uecker. *Generalized model-based reconstruction for quantitative MRI using the Bloch-Equations*. ESMRMB 2019 Congress, Rotterdam 2019, In: Magn Reson Mater Phy (2019) 32(Suppl 1): 235

12. Xiaoqing Wang, Sebastian Rosenzweig, **Nick Scholand**, H. Christian M. Holme, and Martin Uecker. *Model-based reconstruction for simultaneous multi-slice T1 mapping using single-shot inversion-recovery radial FLASH*. In Proc. Intl. Soc. Mag. Reson. Med. 27; 313 (2019)

13. **Nick Scholand**, Sebastian Rosenzweig, Felix Ertingshausen, and Martin Uecker. *Plastic Bricks in MRI: An Efficient Way to Build Static and Dynamic Phantoms*. In Proc. Intl. Soc. Mag. Reson. Med. 27; 1593 (2019)

14. Sebastian Rosenzweig, **Nick Scholand**, H. Christian M. Holme, and Martin Uecker. *Robust Cardiac and Respiratory Self-Gating Using an Adapted Singular Spectrum Analysis (SSA-FARI): Application to Simultaneous-Multi-Slice Imaging*. In Proc. Intl. Soc. Mag. Reson. Med. 27; 2444 (2019)

15. Sebastian Rosenzweig, H. Christian M. Holme, **Nick Scholand**, Robin N. Wilke, and Martin Uecker. *Self-Gated and Real-time Simultaneous Multi-Slice Cardiac MRI from the Same Acquisition*. In Proc. Intl. Soc. Mag. Reson. Med. 26; 209 (2018)

16. H. Christian M. Holme, **Nick Scholand**, Sebastian Rosenzweig, Robin N. Wilke, and Martin Uecker. *Banding-Free Reconstruction in Frequency-Modulated bSSFP using Virtual Coils with Regularized Non-Linear Inversion*. In Proc. Intl. Soc. Mag. Reson. Med. 26; 2870 (2018)

17. Volkert Roeloffs, Jost M. Kollmeier, **Nick Scholand**, Dirk Voit, Sebastian Rosenzweig, H. Christian M. Holme, Martin Uecker, and Jens Frahm. *Joint T1/T2 mapping with frequency- modulated SSFP, radial sampling, and subspace reconstruction*. In Proc. Intl. Soc. Mag. Reson. Med. 26; 2767 (2018)

Thesis

1. **Nick Scholand**, *Model-Based Reconstruction for Quantitative MRI using the Bloch Equations*, Master Thesis, arXiv:1905.03188 (2019)